U.PORTO

DOUTORAMENTO EM CIÊNCIAS FARMACÊUTICAS
ESPECIALIZAÇÃO EM QUÍMICA ANALÍTICA

Environmental contamination by the broad-spectrum herbicide glyphosate: development of simple and low-cost analytical procedures for its quantification and remediation technologies

Luis Angel Zambrano Intriago

D

2023

Luis Angel Zambrano Intriago

Environmental contamination by the broad-spectrum herbicide glyphosate: development of simple and low-cost analytical procedures for its quantification and remediation technologies

Tese do 3º Ciclo de Estudos Conducente ao Grau de Doutor em Ciências Farmacêuticas na Especialidade de Química Analítica

Trabalho realizado sob a orientação da Professora Doutora Maria da Conceição Branco da Silva e coorientação da Professora Doutora Célia Gomes Amorim e do Professor Doutor Joan Manuel Rodríguez Díaz

.

Abril 2023

De acordo com a legislação em vigor, não é permitida a reprodução de qualquer parte desta tese.

A linha da vida alinha-se com o trabalho árduo

This Thesis was also supported by the LAQV/REQUIMTE unit, which is financed by Portuguese national funds (FCT/MCTES) through the project UIDB/50006/2020.



The experimental work presented in this Doctoral Thesis was performed in the Laboratory of Applied Chemistry, Department of Chemical Sciences of the Faculty of Pharmacy, University of Porto, Portugal, and at the Chemical and Biotechnological Analysis Laboratory of the Research Institute of the Universidad Técnica de Manabí.





Acknowledgements

I would like to express my greatest gratitude to my Supervisor, Professor Maria Conceição Branco Silva (Ph.D.), for all the transmission of knowledge and scientific guidance, consideration, availability, tolerance, and friendship. In addition, your willingness to provide me with all the conditions for the development of this thesis.

I also express all my gratitude to my Co-Supervisor, Professor Célia Gomes Amorim (Ph.D.), for her complete availability, scientific guidance, transmission of knowledge, and friendship.

Special thanks to Professor Alberto Araújo (Ph.D.), for his accompaniment and scientific advice for the development of experiments and publications.

A special thanks to Professor Joan Manuel Rodríguez Díaz (Ph.D.), for his scientific guidance, consideration, and friendship. Since 2016 when I started working with him on my graduation thesis, he has always been a mentor to me in my professional growth.

To Andrea Paula Amaral Gouveia, for all the accompaniment, advice, and understanding of her for being an international student.

To all the members of the Sensors and Biosensors Group, for the good work environment, for the support and help in the experiments. A special thanks to Renato Gil, Álvaro Torrinha, Michaela Kohlová, Jaime Cevallos, Andrea Mantovani, and Simone Stefani.

To the Faculty of Pharmacy of the University of Porto and LAQV/REQUIMTE for providing me with the necessary conditions for my work.

A special thanks to my parents, Angelo and Beatriz, for all their unconditional support and belief in me throughout my academic training. To my brothers, Felipe (our angel), Patricia and Diana. To my nephews, Camila, Thomás, Zahir and José for being the joy of the home.

Finally, I want to express my greatest gratitude to my future wife, Mayra Gorozabel, for all her support, understanding, and encouragement to not give up on this dream. Thanks for all your love.

Abstract

This thesis presents the development of an enzyme-type amperometric biosensor for the detection of the broad spectrum herbicide glyphosate. The presence of enzymes on the electrodes makes possible the interaction with specific substrates and inhibitors for indirect detection. The correct immobilization of the enzymes can make detection with high sensitivity and selectivity possible, being able to compete directly in terms of performance against non-enzymatic electrodes, and conventional instrumental chemistry equipment, such as UV-VIS spectrophotometry, liquid and gas chromatography, mass spectrometry, ELISA immunoassays, etc. However, the process of enzyme immobilization is a complex process, as oriented immobilization, direct binding for direct electron transfer, or the requirement of diffusional mediators to ensure electronic binding to the electrode must be obtained. In addition, unsuitable conditions in the measurement medium, such as inappropriate pH, low ionic strength, and inappropriate electrolyte loading can cause problems of stability, sensitivity, and reduce the operating time of the biosensors.

In this work, a low-cost enzymatic biosensor was developed, using easily accessible materials, whose construction was simple and fast. For this purpose, pencil graphite electrodes (PGE) were used as support for the enzymatic recognition membrane. This type of support is considered a viable alternative due to its low cost, commercial availability, and good electrochemical performance. For membrane modification, the horseradish peroxidase (HRP) enzyme was immobilized on a polymeric matrix composed of polysulfone (PSF) and multi-walled carbon nanotubes through a phase inversion process (HRP/PSF/MWCNT/PGE). This approach was fully characterized by cyclic voltammetry (CV) and impedance spectroscopy (EIS). Several analytical conditions were validated, such as concentration of membrane constituints , PGE mine type, buffer concentration and pH, ionic strength, and electrochemical mediator concentration. The proposed biosensor showed high sensitivity for the detection of hydrogen peroxide substrate, demonstrating the effectiveness of the immobilization and measurement conditions. Finally, the biosensor was applied for the determination of glyphosate herbicide through the enzymatic inhibition mechanism. Under optimal experimental conditions, the biosensor showed a linear response in the concentration range of 0.1 to 10 mg L^{-1}. The limits of detection and quantification were 0.025±0.002 and 0.084±0.007 mg L^{-1}, respectively. The proposed biosensor demonstrated high reproducibility, excellent analytical performance, repeatability, and accuracy. The sensor proved to be selective against other pesticides, organic acids, and inorganic salts. Application on real samples showed recovery rates ranging between 98.18±0.11% and 97.32±0.23%.

The second part of the research proposes the development of a treatment technology for the remediation of aqueous matrices with the presence of highly toxic contaminants such as glyphosate. For this purpose, an adsorption system was implemented using as adsorbent a new hybrid material composed of the metal-organic framework MIL-53(Al) and rice husk (MIL-53(Al)@RH) synthesized by microwave assistance. All treatment monitoring was followed through electrochemical measurements employing a glassy carbon (GCE) based sensor modified with a CuOx@mC composite derived from the MOF HKUST-1. MIL-53(Al)@RH exhibited favorable adsorbent characteristics, such as a high adsorption capacity of 296.95 mg g^{-1} using a ratio of 0.04g MIL-53(Al)@RH/50 mL of solution. Kinetic, equilibrium and temperature tests were carried out with the respective mathematical modelling. Likewise, tests of the material in a fixed bed were performed to demonstrate its functionality in batch and dynamic systems. It was determined that the type of adsorption that governed the system was of the chemical type, whose mechanism involved several types of bonds, namely hydrogen bonds, π*-π interactions, and complexes between the metallic center of MIL-53(Al) and the anionic groups of glyphosate. In this way, the importance of developing new materials for the detection and effective treatment of highly toxic contaminants, such as glyphosate, with repercussions on biodiversity and human health that this can cause is demonstrated.

Keywords: Glyphosate, electrochemical biosensor, pollution control, adsorption, hybrid adsorbents, water remediation control.

Resumo

Esta tese apresenta o desenvolvimento de um biosensor enzimático para a detecção amperométrica de glifosato, um herbicida de amplo espectro usado como agrotóxico. A presença de enzimas nos eléctrodos torna possível a interacção com substratos e inibidores específicos para a sua deteção indireta. A adequada imobilização das enzimas torna possível a obtenção de unidades sensoras cujas características de sensibilidade e seletividade competem favoravelmente com as obtidas por eléctrodos não enzimáticos. Além disso, a utilização de biossensores electroquímicos é vantajosa relativamente às técnicas convencionais como por exemplo a espectrofotometria de UV-VIS, a cromatografia líquida e gasosa, a espectrometria de massa, os imunoensaios realizados pela técnica de ELISA, etc. Contudo, o processo de imobilização enzimática é um processo complexo, pois deve ser obtida uma imobilização da enzima de forma orientada, ligação directa para transferência de electrões directa, ou a necesidade de mediadores químicos para garantir a ligação electrónica ao eléctrodo. Além disso, condições do meio de análise menos adequadas, tais como pH das soluções, baixa força iónica e carga electrolítica inadequada podem causar problemas de estabilidade, sensibilidade, e reduzir o tempo de funcionamento dos biossensores.

Neste trabalho foi desenvolvido de um biosensor enzimático, de baixo custo, utilizando materiais comuns facilmente acessíveis, cuja construção era simples e rápida. Para este fim, foram utilizados como suporte para a membrana de reconhecimento enzimático, eléctrodos de minas de grafite (PGE). Este tipo de eléctrodo é considerado uma alternativa viável devido ao seu baixo custo, disponibilidade comercial, e bom desempenho electroquímico. Para modificação da membrana, a enzima peroxidase de rábano (HRP) foi imobilizada numa matrix polimérica composta de polisulfona (PSF) e nanotubos de carbono de paredes múltiplas, através de um processo de inversão de fase (HRP/PSF/MWCNT/PGE). Esta abordagem foi totalmente caracterizada por voltametria cíclica (CV) e espectroscopia de impedância (EIS). Foram validadas várias condições analíticas, tais como a concentração dos constituintes da membrana, o tipo de mina PGE, a concentração de tampão e pH, a força iónica, e a concentração de mediador electroquímico . O biosensor proposto mostrou alta sensibilidade para a detecção de substrato de peróxido de hidrogénio, demonstrando a eficácia das condições de imobilização e medição. Finalmente, o biosensor foi aplicado na determinação do herbicida glifosato, através do mecanismo de inibição enzimática do peróxido de hidrogénio. Em condições experimentais ideais, o biosensor mostrou uma resposta linear no intervalo de concentração de 0,1 a 10 mg L^{-1}. Os limites de detecção e quantificação foram de

0,025±0,002 e 0,084±0,007 mg L^{-1}, respectivamente. O biosensor proposto demonstrou alta reprodutibilidade, excelente desempenho analítico, repetibilidade, e exactidão. O sensor provou ser selectivo em relação a outros pesticidas, ácidos orgânicos, e sais inorgânicos. A aplicação em amostras reais mostrou taxas de recuperação que variavam entre 98,18±0,11% e 97,32±0,23%.

Na segunda fase da investigação desenvolveu-se uma tecnologia de tratamento, para a remediação de matrizes aquosas, com a presença de contaminantes altamente tóxicos, tais como o glifosato. Para este fim, foi implementado um sistema de adsorção utilizando como adsorvente um novo material híbrido composto pela estrutura metal-orgânica MIL-53(Al) e casca de arroz (MIL-53(Al)@RH), sintetizado por assistência de microondas. Toda a monitorização do tratamento foi realizada recorrendo a medições electroquímicas empregando um sensor de carbono vítreo (GCE), modificado com um composto CuOx@mC, derivado da MOF HKUST-1. MIL-53(Al)@RH no sistema implementado apresentou características adsorventes favoráveis, tais como uma alta capacidade de adsorção de 296,95 mg g^{-1} quando era usado uma proporção de 0,04g MIL-53(Al)@RH/50 mL de solução. Foram efectuados testes cinéticos, de equilíbrio e de temperatura com a respetiva modelação matemática. Do mesmo modo, foram realizados testes do material num leito fixo para demonstrar a sua funcionalidade em sistemas dinâmicos e descontínuos. Determinou-se que o tipo de adsorção que governava o sistema era do tipo químico, cujo mecanismo envolvia diversos tipos de ligações, nomeadamente ligações de hidrogénio, interações π*-π, e complexos entre o centro metálico do MIL-53(Al) e os grupos aniónicos de glifosato.

Desta forma, é demonstrada a importância do desenvolvimento de novos materiais para a detecção e tratamento eficaz de contaminantes altamente tóxicos, como o glifosato, com repercussões na biodiversidade e na saúde humana que este pode causar.

Palavras-chave: Glifosato, biosensor electroquímico, controlo da poluição, adsorção, adsorventes híbridos, controlo da remediação da água.

Organization of the Thesis

This Doctoral Thesis in Pharmaceutical Sciences – a specialization branch of Analytical Chemistry, entitled “Environmental contamination by the broad-spectrum herbicide glyphosate: development of simple and low-cost analytical procedures for its quantification and remediation technologies”, is divided into six main chapters, each one containing the following information:

- **Chapter 1** - This section provides the general objective and specific objectives of this Thesis.
- **Chapter 2** - The state-of-the-art, which contains literature on the evolution of electrochemical sensors for the detection of glyphosate.
- **Chapter 3** - Adsorption principles, which contains literature on adsorption, adsorbent materials, kinetic and equilibrium models describing adsorption mechanisms.
- **Chapter 4** – This section provides an overview of the analytical techniques, methods, instrumentation and equipment used throughout the research work. **Chapter 5** - Development of an enzymatic biosensor for amperometric detection of glyphosate. The whole process of validation of analysis and performance of the biosensor is presented, as well as its application in river and drinking water samples.
- **Chapter 6** - Application of a hybrid material composed of Mil-53(Al) metal organic framework with rice husk (RH) (Mil-53(Al)@RH) for the assembly of a glyphosate adsorption system. In this chapter, experiments on adsorbent dosage, pH effect, kinetics, equilibrium, temperature effect, and column system are shown. In addition, an analysis of the adsorption mechanisms involved in the process is proposed.
- **Chapter 7** - Conclusions, which integrates the results obtained from the development of detection and remediation technologies. Prospects concerning modified materials applicable to sensors and remediators.

Table of Contents

Acknowledgements xi

Abstract xiii

Resumo xv

Organization of the Thesis xvii

Table of Contents xviii

List of Figures xxii

List of Tables xxv

Abbreviations xxvi

Chapter 1 1

Objectives 1

Chapter 2 3

State-of-the-art. Electrochemical sensors for glyphosate sensing. 3

2.1. Introduction 4

2.2. Most common analytical methods for GLY determination 5

2.3. Determination methods based on classical electrodes 12

2.4. Analytical methods based on modified electrodes 16

2.4.1. Electrodes structured with nanomaterials 16

2.4.2. Electrodes structured with organometallic compounds 18

2.4.3. Electrodes structured with conductive polymers 20

2.5. Biosensors 24

2.6. Electronic tongues 36

2.7. Conclusions and prospects 37

2.8. References 38

Chapter 3 53

Adsorption principles 53

3.1. Adsorption 54

3.2. Types of adsorption. 55
3.3. Adsorption mechanism. 56
3.4. Sorption equilibrium. 56
3.5. Adsorption equilibrium models....58
3.5.1. Langmuir Isotherm 58
3.5.2. Freundlich Isotherm....59
3.5.3. Toth Isotherm 60
3.5.4. Sips Isotherm....60
3.5.5. Khan isotherm 60
3.6. Kinetics of the sorption process....61
3.6.1. Pseudo-First Order Kinetic Equation 61
3.6.2. Pseudo-Second Order Kinetic Equation 62
3.6.3. Bangham Kinetic Model 62
3.6.4. Avrami Kinetic Model....63
3.6.5. Weber-Morris Kinetic Model....63
3.7. Study of the sorption process under dynamic conditions....63
3.8. Adsorbents. 65
3.8.1. Agroindustrial wastes 65
3.8.2. Rice husk as adsorbent material....66
3.8.3. Metal-organic frameworks as adsorbent material 66
3.8.4. MOF@biomass hybrids as adsorbent material 68
3.9. References....68
Chapter 4 75
Experimental section 75
4.1. Overview of Electrochemical Technology 76
4.1.1. Cyclic voltammetry 76
4.1.2. Amperometry....78
4.1.3. Differential Pulse Voltammetry (DPV)....79

4.1.4. Electrochemical impedance spectroscopy....80
4.2. Instrumentation....81
4.2.1. Apparatus for electrochemical determinations....81
4.2.2. Electrodes....82
4.3. Other equipment....83
4.3.1. UV-VIS spectrophotometer....83
4.3.2. Microwave system for synthesis....84
4.3.3. Equipment employed in adsorption studies....84
4.4. References....85
Chapter 5....87
Development of an inexpensive and rapidly preparable enzymatic pencil graphite biosensor for monitoring of glyphosate in waters....87
5.1. Introduction....88
5.2. Materials and methods....89
5.2.1. Materials and reagents....89
5.2.2. Instrumentation....90
5.2.3. Working electrode development....90
5.2.4. Electroanalytical measurements....91
5.3. Results and discussion....92
5.3.1. Electrochemical characterization of the biosensor....92
5.3.2. Morphological characterization of the glyphosate biosensor....95
5.3.3. Characterization of the electrochemical GLY biosensor....97
5.3.4. GLY determination....101
5.3.5. Selectivity, stability, and reproducibility....103
5.3.6. GLY in real samples....105
5.4. Conclusions....105
5.5. References....106
5.6. Supplementary Data....113
Chapter 6....121

Application of a novel hybrid MIL-53(Al)@rice husk for the adsorption of glyphosate in water: Characteristics and mechanism of the process. 121

6.1. Introduction 122

6.2. Experimental section 123

6.2.1. Materials 123

6.2.2. Measurements of GLY 123

6.2.3. Synthesis of MIL-53(Al)@RH 124

6.2.4. Adsorption tests 125

6.2.5. Adsorption kinetics and isotherms 125

6.2.6. Estimation of adsorption thermodynamics 125

6.2.7. Fixed-bed adsorption experiments 126

6.3. Results and discussion 126

6.3.1. Mil-53(Al)@RH properties 126

6.3.2. Batch adsorption 128

6.3.3. Fixed-bed treatment 137

6.3.4. Adsorption mechanism 138

6.4. Conclusion 140

6.5. References 140

6.6. Supplementary Data 146

Chapter 7 152

General Conclusions 152

Appendix 154

List of Figures

Figure 2.1. a) Chemical structure of GLY, and b) AMPA 4

Figure 2.2. Chromatograms of a) amitrole, GLY, and AMPA obtained by Sánchez-Bayo et al. (55); b) standard mixture of glufosinate, bialaphos, and glyphosate detected by Sato et al. (56); and c) spiked apple juice with glyphosate at the 6.8 mg L^{-1} level according to Coutinho et al. (58) without derivatization of the sample. 12

Figure 2.3. a) Schematic illustration of a metal-organic framework assembled from organic linkers and metal nodes; b) Sensor based on the hierarchically porous Cu-BTC MOF material (100); c) formation of CuOx@mC composite and electrochemical analytical principle (101) 19

Figure 2.4. a) Schematic representation of the main steps regarding the production of MIP (122); b) Preparation of CS molecularly imprinted film (MIPs/Au) and its recognition for GLY (114); and c) double-template imprinted polymer-modified GNPs-PGE fabrication along with a suggested binding mechanism for the simultaneous analysis of NGLY and GLU (121).23

Figure 2.5. a) CV illustration of HRP inhibition effect for H_2O_2 reduction with progressive GLY concentration (154); b) Immuno-magnetic assay of GLY sensing (159); and c) (A)ElectrochemSENSE sensor strip (B) Solid-Liquid interface depicting contact angle made by synthetic buffer PBS on sensor substrate (C) Diagrammatic representation of electrochemical sensor immunoassay stack (D) FTIR Spectrum of DSP (Pink) and DSP-AB (Blue) to validate immunoassay chemistry (162). 27

Figure 2.6. a) Electronic tongues of Martínez Gil et al. (165); b) System designed of Laguarda-Miro et al. (166) 37

Figure 3.1. Schematic representation of the adsorption, absorption and ion exchange processes (6). 54

Figure 3.2. Classification of isotherms according to IUPAC (9).....56

Figure 3.3. Breakthrough curve (34).....64

Figure 3.4. Schematic illustration of a metal-organic framework assembled from organic linkers and metal clusters (58).....67

Figure 4.1. Cyclic voltammogram of a electron oxidation-reduction.....77

Figure 4.2. The current-time profile associated with a potential step redox process (6)....79

Figure 4.3. Examples of Nyquist plots and equivalent circuit models (10) 81

Figure 4.4. Electrochemical workstation composed by the potentiostat Autolab PGSTAT10, computer and electrochemical cell. 81

Figure 4.5. Impedance workstation composed by potentiostat with impedance module (Autolab FRA32M), computer and electrochemical cell. 82

Figure 4.6. a) Ag/AgCl reference electrode, and b) platinum counter electrode 82

Figure 4.7. PGE working electrode used in the development of the biosensor. Inside: 25 cent coin as size reference 83

Figure 4.8. UV-VIS Spectrophotometer, Thermo Scientific, Evolution 60-S. 83

Figure 4.9. Microwave system of the CEM brand, model Mars 6. 84

Figure 4.10. Shaker system Eppendorf New Brunswick Excella E24/E24R 84

Figure 4.11. a) Packed column of Mil-53(Al)@RH, b) Column adsorption system, including peristaltic pump, packed column, and fraction collector. 85

Figure 5.1. Schematic representation of the different construction phases of the HRP/PSF/MWCNT/PGE biosensor. 91

Figure 5.2. a) Cyclic voltammetry results for the effect of HRP/PSF/MWCNT/PGE scan rate in an equimolar 5 mmol L^{-1} solution of $Fe(CN)_6^{3-/4-}$ with 0. 1 mol L^{-1} KCl (3 to 140 mV s^{-1}), b) I_{pa} and I_{pc} versus square root of the scan rate, c) Electrochemical impedance spectroscopic measurements of PGE (▲), PSF/MWCNT/PGE (●), and HRP/PSF/MWCNT/PGE (■), and d) circuit model for evaluation of the parameters. 94

Figure 5.3. FTIR-ATR of the membrane with the immobilized enzyme. The main features of the PSF polymer are indicated in blue color. 95

Figure 5.4. SEM micrographs of the HRP/PSF/MWCNT membrane (a); EDS spectrum for Z1 (b), Z2 (c), Z3 (d) 97

Figure 5.5. a) Cyclic voltammetry for HRP/PSF/MWCNT/PGE biosensor under different H_2O_2 concentrations, and b) Linear representation of the CV test for catalytic reduction. Conditions: 1.8 mmol L^{-1} of HQ; 0.1 mol L^{-1} PBS (pH 6); scan rate 10 mV s^{-1} (vs Ag/AgCl). 98

Figure 5.6. The catalytic cycle representation of the proposed sensing mechanism between HRP with H_2O_2 and HQ (compounds I and II denote enzyme intermediates in the reaction) 99

Figure 5.7. a) Amperometric measurements of H_2O_2 with HRP/PSF/MWCNT/PGE; b) Calibration curve plot of the HRP/PSF/MWCNT/PGE. Conditions: 0.01 mol L^{-1} PBS buffer (pH 6); 0.5 mM of HQ; applied potential -0.05 V (vs Ag/AgCl). 100

Figure 5.8. Lineweaver-Burk plot for the biosensor response to H_2O_2 in the absence and presence of GLY. 102

Figure 5.9. a) Amperometric responses for HRP/PSF/MWCNT/PGE in the presence of 0.075 mmol L^{-1} H_2O_2 after interaction with solutions of 0.1, 0.5, 1, 3, 5, 7, and 10 mg L^{-1} of GLY (Conditions: 0.01 mol L^{-1} PBS (pH 6), 0.1 mol L^{-1} KCl, and 0.5 mmol L^{-1} HQ), b) Calibration curve for GLY. 103

Figure 5.10. The sensitivity (μA μM^{-1}) of three-parallel HRP/PSF/MWCNT/PGE towards H_2O_2 (biosensor calibration process), and the stability within 15 days. 104

Figure 6.1. Characterization of MIL-53(Al)@RH layered hybrid a) Nitrogen adsorption and desorption isotherm, b) thermal stability (TGA-DTG) of the hybrid and its parent independent materials (RH and MIL-53), c) scanning electron microscope (SEM), d) XRD patterns , e) FTIR spectra, and f) pHpzc graphical method 127

Figure 6.2. a) Adsorbent dose effect on GLY removal using MIL-53(Al)@RH; b) pH_0 effect on GLY removal using MIL-53(Al)@RH. (C_o = 100 mg L^{-1}, t = 180 min, T = 298.15 K)...129

Figure 6.3. Contact time effect on the adsorption of GLY employing MIL-53(Al)@RH, and PFO, PSO, Bangham, and Avrami kinetic models with non-linear adjustment. 132

Figure 6.4. Equilibrium isotherms to adsorb GLY using MIL-53(Al)@RH 135

Figure *6.*5. a) Scheme of the fixed-bed column adsorption system; b) Breakthrough curves of GLY adsorption by MIL-53(Al)@RH packed column 137

Figure 6.6. a) FTIR spectra of MIL-53(Al)@RH before and after contact with GLY solutions at 60, 140, and 300 mg L^{-1}, and b) Schematic illustration of the possible mechanism of GLY adsorption on MIL-53(Al)@RH. 139

List of Tables

Table 2.1. Conventional methods quantification of glyphosate in waters and other matrices 6

Table 2.2. General and modified electrodes for glyphosate sensing 29

Table 6.1. Kinetic parameters for the adsorption of GLY with MIL-53(Al)@RH.....130

Table 6.2. Adsorption isotherm parameters and R^2, HYBRID, and MPSD values for the Langmuir, Freundlich, Sips, Toth, and Khan isotherms at 288.15, 298.15, 313.15, and 328.15 K.....134

Table 6.3. Thermodynamic parameters for GLY adsorption onto MIL-53(Al)@RH 136

Table 6.4. q_t, q_u, and MTZ of the GLY adsorption column at various concentrations calculated from the breakthrough curves. 137

Abbreviations

AMP	Amperometry
AMPA	Aminomethyl)phosphonic acid
AuNPs	Gold nanoparticles
BET	Brunauer-Emmett-Teller model
BQ	p-benzoquinone
Ce	Concentration in the equilibrium
CE or Ce	Counter electrode
CEL	Capillary electrophoresis
Co	Initial concentration
CP	Carbon paste
CPE	Carbon paste electrodes
CPol	Conductive polymers
CRAMP	Chronoamperometry
CuO	Copper oxide nanoparticles
CuNPs	Copper nanoparticles
CV	Cyclic voltammetry
DME	Dropping mercury as the working electrode
DMF	Formic acid dimethylamide
DPP	Differential pulse polarography
DPV	Differential pulse voltammetry
DSP	Dithiobis(succinimidyl propionate
EDS	Energy-dispersive X-ray spectroscopy
EIS	Electrochemical Impedance Spectroscopy
ELISA	Enzyme-linked immunosorbent assay
FTIR	Fourier-transform infrared spectroscopy
GC	Gas chromatography
GC-MS	Gas chromatography with mass spectrometry
GCE	Glassy carbon electrode
GLU	Gluphosinate
GLY	Glyphosate
H_2O_2	Hydrogen peroxide
HMDE	Hanging mercury drop electrode
HPLC	High-performance liquid chromatography
HRP	Horseradish peroxidase
IC-MS	Ion chromatography with mass spectrometry
IUPAC	International Union of Pure and Applied Chemistry
LC-MS	Liquid chromatography with mass spectrometry
HQ	Hydroquinone
HRP	Horseradish peroxidase
HYBRID	Hybrid fractional error function
IL	Ionic liquid
ITO	Indium tin oxide
LOD	Limit of detection
LOQ	Limit of quantification
LSV	Linear sweep voltammetry

MIPs	Molecularly imprinted polymers
MIL-53(Al)@RH	Hybrid material
MOF	Metal-organic frameworks
MPSD	Marquardt's percent standard deviation
MTZ	Mass transfer zone
MWCNTs	Multi-Walled Carbon Nanotube
NHE	Normal hydrogen electrode
NMP	1-methyl-2-pyrrolidone
OMT	Omethoate
PAni	Polyaniline film
PATP	p-Aminothiophenol
PBS	Phosphate buffer solution
PFO	Pseudo-first order
PGE	Pencil graphite electrode
pHpzc	Point of zero charge
PSF	Polysulfone
PSO	Pseudo-second order
Pt	Platinum
PVP	Polyvinylpyrrolidone
Py	Pyrrol
Q	Adsorption capacity
Qe	Adsorption capacity in the equilibrium
Qt	Adsorption capacity in the time
qt	Total adsorption capacity in dynamic systems
qu	Useful adsorption capacity in dynamic systems
RE	Reference electrode
rGO	Reduced graphene oxide
RH	Rice Husk
SCE	Saturated calomel electrode
SEM	Scanned electron microscope
SPE	Screen-printed electrode
SWV	Square Wave Voltammetry
TGA	Thermogravimetric analysis
UV-Vis	Ultraviolet-visible
WE	Working electrode
XRD	X-ray powder diffraction

Chapter 1

Objectives

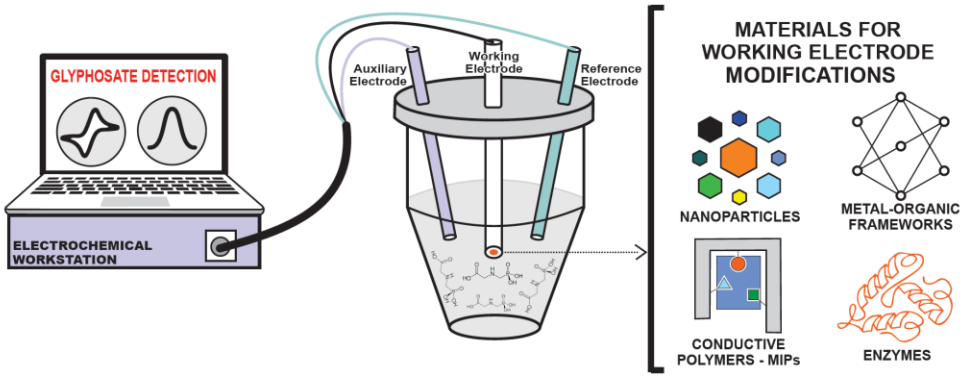
The main objective of this thesis was the development of simple and low-cost analytical procedures for the detection and remediation of the broad-spectrum herbicide glyphosate in water, as alternatives to conventional methods of monitoring and treatment of contaminated water.

In the first research phase, the objective was to develop a low-cost enzymatic biosensor for the amperometric detection of glyphosate in water. For this purpose, the design and construction of the biosensor were proposed based on a pencil graphite electrode (PGE) and its subsequent modification of the surface with polymer and carbon-based materials. Immobilization strategies of the oxidoreductase enzyme horseradish peroxidase were then applied. The immobilization process was based on adsorption and entrapment procedures. The immobilization efficiency and characterization of the biosensor were evaluated by microscopic, spectrometric, voltammetric and amperometric techniques. The analytical validation of the biosensor for glyphosate detection was developed, considering the criteria of linear range, LOD, LOQ, sensitivity, selectivity, stability, reproducibility and application with real samples.

In the second research phase, the objective was to use as remediation technology a hybrid material based on Metal-Organic Framework (MOF; Mil-53(Al)) and biomass as support (rice husk, RH), called Mil-53(Al)@RH, in a treatment system based on the unitary operation of adsorption in batch and column configurations. A glassy carbon electrochemical sensor based on copper oxides was used for monitoring the treatment platform. To determine the performance of the hybrid material in the batch adsorption system, adsorbent amount , effect of solution pH, the effect of contact time, concentration and temperature were tested, as well as mathematical modelling for the interpretation of the mechanisms governing the adsorption system. On the other hand, the study in a column was developed to determine the performances of breakthrough and saturation point times, breakthrough and total adsorption capacity, and the mass transfer zone (MTZ).

Chapter 2

State-of-the-art. Electrochemical sensors for glyphosate sensing.



Chapter 2 contains literature on the evolution of electrochemical sensors for the detection of glyphosate[1]

[1] This is a partial translation of the article *Zambrano-Intriago LA, Amorim CG, Rodríguez-Díaz JM, Araújo AN, Montenegro MCBSM. Challenges in the design of electrochemical sensor for glyphosate-based on new materials and biological recognition. Science of The Total Environment. 2021;793:148496. doi: Https://doi.org/10.1016/j.scitotenv.2021.148496.* Copyright 2021, with permission from Elsevier

2.1. Introduction

Nowadays, the most popular herbicide in fighting a broadleaf weed and wild grass species is perhaps glyphosate (GLY) due to its high efficacy and broad spectrum of applicability. The compound is the N-(phosphonomethyl) glycine (Figure 2.1 a), which along with other substituted glycines forms a subset of the organophosphorus pesticides (1, 2). GLY inhibits the 5-enolpyruvyl shikimate 3-phosphate synthase, a pivotal enzyme of the shikimic acid pathway by which essential aromatic amino acids such as phenylalanine, tyrosine, and tryptophan, are synthesized (3, 4). The enzyme is absent in mammals and insects, despite being expressed in some bacteria, fungi, and algae. Therefore, only a selective effect is expected when leaves of wild plant varieties are sprayed with GLY (5). Besides phosphonate, the molecule bears amine and carboxylate functional groups with the ability to coordinate different transition metals, namely Fe(III) or Al(III), and be that way retained in different environment compartments for a long time (6, 7). Some species of microbiota inhabiting soils are then capable to metabolize GLY to (aminomethyl)phosphonic acid (AMPA) (Figure 2.1 b) and ultimately to carbon dioxide and inorganic phosphate (8).

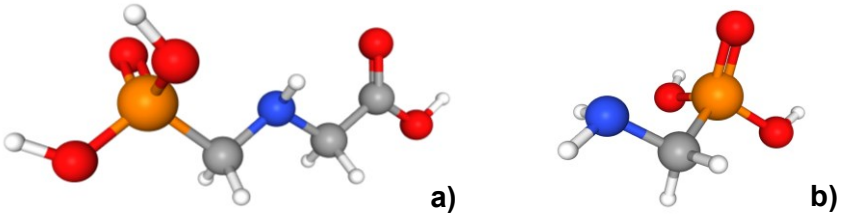


Figure 2.1. a) Chemical structure of GLY, and b) AMPA

GLY has been intensively used since its introduction in the commercial market in 1974 as ammonium, isopropylamine, or sodium salt (9). In the last decade, more than 750 different trademarks sold about 6.1 billion kilograms of GLY for agricultural, urban, and domestic use (10, 11). The main reasons for such success were the emergence of genetically modified crops resistant to the herbicidal action in agricultural practices, and the minimal oral acute toxicity meanwhile reported (10, 12). During the introduction of glyphosate in the market, the World Health Organization (WHO) considered the herbicide harmless to people (13). However, suspicions about GLY assimilation by non-target living organisms, including humans, were nevertheless issued and it was only evidenced after the analytic inspection of blood and urine samples of individuals that routinely handling it (10, 14, 15).

Chronic exposure to glyphosate is however noxious and commonly associated with a plethora of human pathologies including epithelial (16, 17), neural (18–20), cardiocirculatory and muscular disorders (20–22), neoplasia, and teratogenic effects (23–27). According to

some studies (26–28), GLY concentrations one hundred times lower than those used in agricultural practices can interact with estrogenic and androgenic receptors on the surface of cells (29–31) and behave as a competitive aromatase inhibitor (25–27). The inhibitory effect as referred to for aromatase extends to other cytochrome P450 isozymes constituting the Phase I detoxification pathway in mammals. As a consequence, there is an increment in foodborne chemical residues and other xenobiotics (16). On the other hand, it has been observed that GLY-DNA interaction results in the oxidation of pyrimidines that can induce teratogenic and carcinogenic effects (22–25). Even so, few authors claim that GLY and its AMPA metabolite inhibit the proliferation of cancer cells and promote their apoptosis, namely on prostate cancer cells (30), without affecting normal cells (31). However, IARC (32) has eventually recognized GLY as purporting carcinogen risk to humans. Given the described effects the United States and the European Community described 700 μg L^{-1} and 0.1 μg L^{-1}, as a tolerable GLY levels in drinking water, respectively (33, 34)

Because of the hazardous effects on human health and the environment, it is important to develop advanced, selective, and sensitive analytical methods that produce reliable results for monitoring GLY in multi-component matrices, such as water, soil, food, grain, beverage, agricultural products, etc. Although different analytical methods for the determination of GLY were described, at the time of writing the article (Appendix B1) there was no review article that aimed at the use of electrochemical sensors for its determination. Thus, it will be discussed the different strategies for GLY determination by using metal and modified electrodes, biosensors, or electronic tongues.

2.2. Most common analytical methods for GLY determination

Different analytical methods have been proposed for GLY in biological fluids, soil, agri-food products, and beverages analysis (Table 2.1). Most of them also detect its metabolite AMPA and use sensitive detection techniques but are associated with separation techniques as is the case of high-performance liquid chromatography (HPLC) (35–37), liquid chromatography with mass spectrometry (LC-MS) (38–41), gas chromatography (GC) (42–44), gas chromatography with mass spectrometry (GC-MS) (45, 46), ion chromatography with mass spectrometry (IC-MS) (47), capillary electrophoresis (CEL) (48–51), and enzyme-linked immunosorbent assay (ELISA) (52–54).

Table 2.1. Conventional methods quantification of glyphosate in waters and other matrices

Method	Analyte	Sample	Sample preparation description	L.R. ($\mu g\ L^{-1}$); ($\mu g\ Kg^{-1}$)*	D.L ($\mu g\ L^{-1}$); ($\mu g\ Kg^{-1}$)*	Ref
CEL; contactless conductivity detection	GLY AMPA	Water	Microextraction method based on cone-shaped membrane termed dynamic supported liquid membrane tip extraction (SLMTE)	0.01 - 200 0.1 - 400	0.005 0.06	(48)
CEL; electrochemiluminesce detection	GLY AMPA	Water; Soybean	GLY-spiked sample followed by water extraction and deproteinization.	170 - 17000 5550 - 111000	60 4040	(49)
CEL; fluorescence detection	GLY GLU AMPA	Commercial herbicides (Ninninchun - 41% GLY; Basida - 13.5% GLUF)	Direct injection of diluted sample with running buffer (fluorescein)	2200 - 270000 1200 - 390000 4200 - 210000	203 119 1888	(50)
GC; flame photometric detection	GLY AMPA	River water; Yellow-brown soil	Solid-phase extraction (SPE) procedure, derivatized by heptafluorobutyric anhydride and heptafluorobutanol	10 – 1000 10 – 1000	0.10 0.22	(43)

GC; tandem mass spectrometry	GLY AMPA	Water	Samples purified by column chromatography on ion-exchange resins and post-derivatization with TFAA/HFB mixture	0.05 - 5 0.05 - 5	0.025 0.025	(45)
HPLC; tandem mass spectrometry	GLY AMPA	Surface water; groundwater	Samples of water fortified with internal standard.	0.1 - 100 0.1 - 100	0.02 - 0.05 0.02 - 0.05	(38)
LC; fluorescence detection	GLY AMPA	Seawater	Artificial seawater derivatized with FMOC-Cl	2 - 160 160 - 480 480 – 2400 1 - 16 10 - 200	0.60 0.30	(35)
LC/coupled Au electrode with Pulsed Amperometric Detection (PAD)	GLY AMPA	River water	Samples filtered through 0.7µm GF/F glass microfibre spiked with a mixture of GLY, AMPA and amitrole.	1000 - 180000 100 - 50000 50 - 40000	320 50 30	(55)
ELISA; enzyme-linked immunosorbent assay	GLY	Tap water	Sample mix with enzyme conjugate and anti-glyphosate particles	1 - 25	0.6	(52)
CI-ELISA; competitive indirect	GLY	Water	Sample mix with polyclonal antisera, secondary antibody, GARHRP, 2,2'-azinobis(3-	10000 - 1000000	7600	(53)

enzyme-linked immunosorbent assay			ethylbenzothiazoline-6-sulfonic acid, and urea hydrogen peroxide.			
Other matrices						
CEL; UV/VIS detection	GLY AMPA PARQ	Abuse drug: marijuana	A powdered sample mixed with glutamic acid working solution and hydrochloric acid.	10000 -1000000* 10000 -1000000* 5000 - 1000000*	8 000* 8 000* 800*	(51)
GC; pulsed flame photometric detector	GLY GLU AMPA MPPA	Rice; soybean	Recovery and purification in a spiked sample with post derivatization and cleanup process with florisil cartridge	100 - 50000 25 - 25000 100 – 50000 100 - 25000	20 20 30 10	(42)
GC; nitrogen-phosphorus detector	GLY	Soil	Extracted sample derivatized by trifluoroacetic anhydride and trifluoroethanol	100 – 20000	10*	(44)
GC; mass spectrometry	GLY GLU AMPA	Human serum	Purified spiked sample with SPE process and reconstituted with MTBSTFA with 1% TBDMCS and acetonitrile	3000 - 100000 3000 - 100000 3000 - 100000	250 50 250	(46)
HPLC; UV detection	GLY AMPA	Orange, grapefruit, apple and	Spiked sample extracted for post-derivatization with p-toluenesulphonyl chloride	25 – 10000 25 – 10000	10 10	(36)

		blackcurrant juices				
IC; Inductively coupled plasma	GLY AMPA PO_4^{3-}	Drinking water, reservoir water and Newater	Chlorine free spiked sample through sodium thiosulfate	1-1000 1-1000 1-1000	1.5 1 1	(47)
LC; fluorescence detection	GLY	Soil/sludge from China	Extracted and purified sample for derivatized by FMOC-Cl	5 - 500	10*	(37)
UPLC; tandem mass spectrometry	GLY GLU BIA AMPA MPPA	Blood samples from real forensic cases	Extraction by Quick Polar Pesticides Extraction (QuPPe) method, and cleanup with the PRiME HLB sorbents	50 - 5000 50 – 5000 30 – 5000 50 – 5000 30 - 5000	20 20 10 20 10	(39)
LC; tandem mass spectrometry	GLY AMPA	Celery cabbage, cucumber, kidney beans, potato, and orange.	Supernatant from direct centrifugation of the sample with water.	0.5 - 500 5 – 1000	1.2* 15*	(40)
LC; tandem fluorescence - mass spectrometry	GLY AMPA	Powdered maize shoot	Supernatant from direct centrifugation of sample with water following derivatization (FMOC-Cl)	130 – 1000000* 40 - 1000000* 240 – 1000000* 60 - 1000000*	40* (FLD) 10* (ESI-MS) 70* (FLD)	(41)

					20* (ESI-MS)	
LC/coupled Au electrode with Pulsed Amperometric Detection (PAD)	GLY GLU BAP	Human serum. Human urine. Mouse urine.	Spiked Serum (separated from blood by centrifugation) and urine diluted (1:100 HS, 1:1000 urine) and filtered. Mouse urine was obtained after oral administration with subsequent preparation equal to human urine.	100 - 50700 100 - 45300 300 - 32300	51 18 65	(56)
LC/coupled Cu microelectrode with coulometric detection	GLY	Apple juice. Grape juice. Tomato juice.	Spiked samples centrifuged and filtered before injection	100 - 34000	100	(57, 58)
CI-ELISA; competitive indirect enzyme-linked immunosorbent assay	GLY	Turmeric, chili, tea, coriander, coffee, rice, and ginger	Sample mix with an Anti-glyphosate antibody obtained from poultry egg yolk immunized with glyphosate protein (gly-BSA).	2 – 1000	2	(54)

LR (Linear Range); DL (Detection Limit); GLY (Glyphosate); AMPA (Aminomethylphosphonic Acid); GLU (Glufosinate); BIA (Bialaphos); MPPA (3-(methylphosphinico)propionic acid); PARQ (Paraquat)

Chromatographic methods are the most commonly used for the quantitative determination of GLY but require laborious sample pre-treatment procedures that are time-consuming and above all environmentally unfriendly (37, 59). Furthermore, these methods do not give real-time results and are confined to the laboratory bench. Since most of the time an optical detection process is used, a derivatization step is required for assessing appropriate retention in the chromatographic columns and low detection limits. This increases the time of analysis, the costs and also generates hazardous waste (35, 37, 41–46).

CE is another alternative method frequently used for GLY and AMPA monitoring. However, it has some limitations arising from migration mobility and hence the separation of the compounds is greatly affected by the experimental conditions such as the pH of the sample (48, 51). ELISA has also been used avoiding of the derivatization processes and complex sample pre-treatments (52–54). However, is a labour-intensive assay with numerous tedious wash steps, suffers from short signal stability, is an absorbance-based readout that has a narrow analytical range window and due to the numerous wash steps, weak antibody-analyte interactions may not be detected and high detection limits are obtained (60).

As an alternative to the separative and immunoassay methods employed in the determination of GLY, electrochemical detection has emerged. The use of sensors with electrochemical techniques (potentiometry, voltammetry and amperometric) has raised interest in the detection of organic compounds such as pesticides. Electrochemical detection has demonstrated applicability in different areas, such as environment, health and food. Compared to conventional methods it has favourable characteristics such as speed of analysis, low cost, low detection limits and the ability to modify the sensors as required, making them highly sensitive and selective (5). Another characteristic of electrochemical systems is that they can operate as detectors in static methods or coupled to separative techniques such as chromatographic techniques (61). The recognized advantages of this configuration are their simplicity, and less prone to interferences. When chromatographic methods are used, the separation of other herbicides that interfere with the determination of GLY in aqueous matrices can be guaranteed (Figure 2.2). Furthermore, one of the merits of chromatography coupled with electrochemical detection is the possibility of direct determination and quantification of GLY and the other analytes without any derivatization procedures (55–58). In addition, the determination is faster, suggesting that this detection technique may be applicable in the determination of this compound with advantages over traditionally used optical methods.

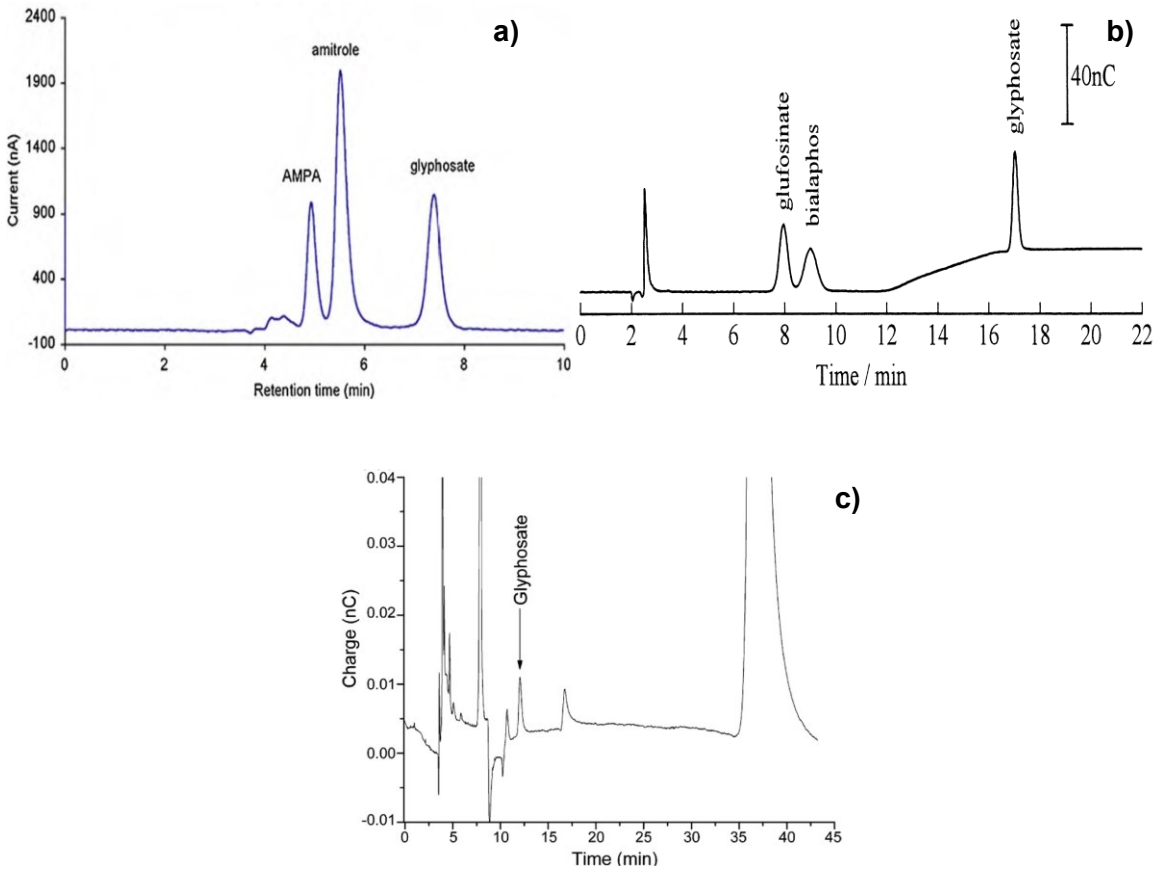


Figure 2.2. Chromatograms of a) amitrole, GLY, and AMPA obtained by Sánchez-Bayo et al. (55); b) standard mixture of glufosinate, bialaphos, and glyphosate detected by Sato et al. (56); and c) spiked apple juice with glyphosate at the 6.8 mg L^{-1} level according to Coutinho et al. (58) without derivatization of the sample.

2.3. Determination methods based on classical electrodes

The first reported method for the electrochemical determination of GLY was authored by Brønstad and Friestad (62) using differential pulse polarography (DPP). The method accomplished determinations of the N-Nitrous derivative resulting from the reaction between GLY and potassium bromide. The polarogram, i.e. electron current intensity versus applied potential recording, showed a wave with a defined peak at -0.78 V. At optimal conditions, peak height was proportional to GLY concentration in the range of 35 to 210 µg L^{-1}, but the sensitivity of measurements was affected by fluctuations in sample pH, dissolved oxygen, and nitrite content. The electrochemical cell consisted of dropping mercury as the working electrode (DME), in addition to platinum and saturated calomel (SCE) as counter and reference electrodes, respectively. Theretofore, mercury (Hg) was the most widely used electrodic material. Its liquid nature facilitated successive clean contaminated surfaces at each determination before dripping off from the capillary. As inert material, it also withstands a large window of useful potentials, -2.5 V to +0.4 V relative to a normal hydrogen electrode

(NHE) (63–65). Several adaptations of the Brønstad and Friestad (62) method were deployed with other transduction modes. Daňhel et al. (65) used a hanging mercury drop electrode (HMDE) and differential pulse voltammetry (DPV) to detect and quantify the N-nitrosoglyphosate derivative in concentrations above 2 mg L^{-1} in samples of soil with a significant content of organic matter. The determination was also optimized with a factorial design, by Teófilo (66) who additionally used square wave voltammetry (SWV) to minimize noise, *i.e.* contribution of the non-faradaic component to the analytical signal. The described linear range was wide (50 µg L^{-1} to 100 mg L^{-1}), the limit of detection was good (LOD 25 µg L^{-1}), and only limited by the incomplete reaction of GLY in the sample.

In the form of zwitterion, chemical groups in GLY molecules are not able to undergo reduction or oxidation at low potentials. However, it is capable of coordinating metal ions in specific oxidation states generated at amenable potentials by heterogeneous electron charge transfer at the electrode surface (67–70). For instance, in an alkaline medium, GLY behaves as a tridentate ligand towards Cu^{2+}, with amine nitrogen, carboxylic, and phosphonate oxygens forming two chelate rings (6). Based on this property, dos Santos et al. (71) used an HMDE working electrode and SWV for the detection of Cu(II)-GLY complex in solution. Signal response to different potential scanning rates indicated a quasi-reversible process controlled by diffusion of the electroactive species at the electrode-solution interface. The method was evaluated using real samples in the presence of interferents (humic acid) with recoveries in the order of 99%. The working range and the limit of detection were of the same order of magnitude as previous approaches, 0.07 to 0.60 mg L^{-1} and 22 µg L^{-1}, respectively.

The risk concerning poisoning and environmental contamination raised by handling and use of mercury eventually turns solid electrodes more attractive. Popular options range from traditional carbon-based electrodes (glassy carbon electrode (GCE), carbon paste (CP), pencil graphite (PGE)) and metals (particularly copper, nickel, gold, and platinum) to more advanced materials such as indium tin oxide (ITO). Cross-contamination avoidance and optimal performance nevertheless require careful cleaning of the electrodic active surface for reuse, often a tedious task. Hence, Aguirre et al. (72) resorted to CGE with the active surface cast with an electrodeposited layer of metallic copper. The electrode was immersed in 10 mM $CuSO_4$, 1 M Na_2SO_4 in 0.1 M H_2SO_4 solution, and a constant potential of -0.6 V vs. Ag/AgCl, KCl (3 M) reference electrode for 100 s, was set after chronoamperometric optimization. In this way, copper nucleation under diffusion-controlled growth started at the electrode surface and a continuous layer of copper agglomerates of about 500 nm thick ultimately was formed. The CV performed in acetate buffer solution at pH 5, was similar to the ones obtained by Coutinho et al. (57, 58, 67) with the copper microelectrode. The

content of GLY in natural waters was determined by DPV in the analytical range of 0.07 - 1.69 mg L^{-1} (LOD of 31 µg L^{-1}) and no interferences from Al^{3+}, Ca^{2+}, Fe^{3+}, and Mg^{2+} were observed. The electrodeposition of the same metal was followed by Regiart et al. (73) to generate a copper microelectrode with a nanoporous active surface. The amount of soluble copper ions that diffuse through the pores and are chelated by GLY at the electrode interface increased proportionally to the herbicide concentration when a positive potential was applied. The sensitivity and limit of detection of the proposed determination procedure were improved regarding the simple copper film described before, though with a lower linear analytical range (Table 2.2).

Besides the copper uses to form detection complexes, electrodes have been developed with nickel, which forms stable octahedral complexes. On the other hand, transition metals such as cadmium, lead, zinc, calcium, cobalt, iron, magnesium, manganese, chromium, and silver have been less studied in terms of complexation with GLY. Despite this, most authors have shown that these metals do not generate significant interferences in the detection of GLY (69, 74). Sierra et al. (75) investigated the ability of GLY to complex Ni^{2+} and Cu^{2+} ions in passivated surfaces of both corresponding metal electrodes. After cathodic activation of the copper surface, the electrode was poised at the positive potential in an alkaline medium to promote oxidation, dissolution, and deposition of a less conductive-passivated CuO layer. The alkaline medium facilitated the dissolution of Ni(II) as hydroxide afterwards oxidated to NiO(OH). Through electrochemical impedance spectroscopy (EIS) authors observed the proportional diameter reduction of semi-circles in Nyquist plots with increasing GLY concentrations (76, 77). The results were less evident regarding GLY-Ni interactions for the passivated nickel electrode which also gave the worst signals. The approach resorted by Khenifi et al. (78) was different and consisted of electrogenerated $Ni_{1-x}Al_x(OH)_2NO_{3x}\cdot nH_2O$ layered double hydroxide (NiAl-LDH) on the surface of a platinum electrode. The increased surface area of the NiAl-LDH 2D structure provided lower impedance to charge transfer due to coexisting Ni^{2+}/Ni^{3+} states, as well as anion exchange behaviour favouring the adsorption of negatively charged herbicides. In the presence of GLY and alkaline medium, the anodic peak in the voltammogram at 0.52 V (vs. SCE) corresponding to the oxidation of Ni^{2+} to Ni^{3+} increased as a result of GLY oxidation by Ni(III) centres in the LDH structure. This electrode showed improved selectivity over GLY, as the slope of the calibration curve obtained for the chemically related GLU herbicide was nearly halved. Its response had linear dependence on GLY concentration between 1.7 - 152 mg L^{-1} and a LOD of about 200 µg L^{-1}, though without performance evaluation using real samples. Recently, a nanocomposite of CuAl-LDH and graphene was used to cast the electroactive surface of GCE (79). The voltammetric signal enabled by the complex Cu(II)-GLY resulted well defined due to the

increase of electrical conductivity and active surface area imparted by graphene. The electrode was applied in the determination of concentrations within 0.5 to 199.5 μg L^{-1} of GLY in waters with recoveries above 97% and the presence of organophosphorus pesticides and inorganic ions.

Homemade carbon paste electrodes (CPE) are easily implemented after blending the mixture of graphite microcrystalline powder with a wax binder and stuck over an electronic conductor offering low-cost alternatives to GCE. They additionally provide ease incorporation of reversible electron shuttle compounds to increase electron transfer rates or improve selectivity (80). Oliveira et al. (81) used this kind of electrode to accomplish indirect determinations of GLY in milk, juices, and agricultural formulations. The determination was based on the electrochemical oxidation at pH 5 of the GLY isopropylammonium counter ion at 0.9 V vs Ag/AgCl, KCl (3 M). This approach enabled the determination of the pesticide in a concentration interval between $4.4x10^{-8}$ - $2.8x10^{-6}$ mol L^{-1}. The interference from metal ions and other common pesticides such as atrazine, linuron, thiamethoxam, trifluralin, or trifloxystrobin was inferior to 2% even when the concentrations of interferent were 2000x higher. In the work of Pintado et al. (82, 83), the CPE electrode also included Cu powder and was applied on the surface of GCE. In addition to GLY-Cu(II), the conditions for the formation and quantification of the AMPA-Cu(II) complex was further addressed. In turn, Wong et al. (84) implemented a CPE incorporating copper(II) hexadecafluoro-29H,31 phthalocyanine complex for the analysis of GLY by SWV in spiked river water samples and orange juice. The additional modification of the electrode with biochar resulted in the improvement of heterogeneous electron transfer, translated by a 100% increase in the obtained analytical signals. An analytical range between 50.72 and 676.28 μg L^{-1} and LOD of 3.38 μg L^{-1} were obtained for f = 15 Hz, ΔE = 5 mV, and amplitude of 100 mV, from -0.4 to 0.4 V vs Ag/AgCl. The modified electrode showed to be selective in the presence of diuron, 2,4-dichlorophenoxyacetic acid, atrazine, urea, and uric acid as interfering compounds. Finally, Mbokana et al. (85) modified a CPE electrode with an organosmectite for direct oxidation of glyphosate (EPa = 1.1 V, IPa = 7.8 μA, for 0.1 mM GLY in PBS 0.1 M, pH 6.8). Among clays, smectites exhibit the highest reactivity and offer simpler modification strategies when functionalization is considered. They can accept large guest compounds in the interlayer space while behaving as cationic exchangers, and have layer edges rich in reactive aluminols and silanols groups that can be easily functionalized. Authors grafted an organophilic silane in the interlayers of acid-treated smectite using ethylene glycol as a solvent to enhance pesticide sequestration. In this way, the analyte, as well as AMPA, were strongly adsorbed at the electrode surface. Calibration curves obtained

by SWV were linear between 10 and 100 µM, with LOD of 165.7 µg L^{-1}. The analysis of soil samples showed an important interference of Cu^{2+} ion, due to the formation of complexes.

Screen-printing technology presents a new opportunity for the application of electrochemical techniques in the analysis of environmental contaminants outside a centralized laboratory. Tracks corresponding working, counter, and pseudo-reference electrodes are printed through a porous master mask over one x half inch ceramic or polymeric substrates that can be mass-produced with constant chemical performance and combining different electrodic materials. They are easily acquired from different sellers. Screen-printed electrodes (SPEs) are thought for single-use and disposable. They can be used in miniaturized procedures where 50 µL of sample plus electrolyte are dropped over the surface of the electrode or by immersing the electrode in a small volume (< 5 mL) cylinder cup. This way, SPEs have been successfully applied for *in situ* analysis of organic compounds, such as herbicides and pesticides (86, 87). Noori et al. (68) proposed the detection of GLY in drinking water with a gold-SPE proceeded at 0.78 V vs. Ag pseudo-electrode by chronoamperometry for 50 s, at pH 8 without support electrolytes in the solution. The metabolite AMPA and the pesticide omethoate (OMT) did not interfere since the corresponding oxidation peaks occurred at low potentials. The performance was sufficient to attend to the US regulations, though not enough to comply with the EU regulatory requirements. A similar design was evaluated by Habekost (88). In this work, gold-SPE provided the detection of GLY and AMPA copper complexes in solution. Before the measurements, SWV was applied to determine the voltage at maximum current. The proposed amperometric procedure enabled to detection of GLY and AMPA above the concentrations of respectively 169.1 µg L^{-1} and 1691 µg L^{-1}.

In this context, it is demonstrated that the application of metallic electrodes is a viable option for the development of GLY sensors. Prevailing the formation of metal complexes for indirect determination, it demonstrated specificity in the presence of GLY. However, this behavior can generate drawbacks in terms of the quality of the electrical signal or electron transfer. This led to the synthesis of other materials such as carbon derivatives, which create mechanically stable supports and increase the sensitivity of detection systems.

2.4. Analytical methods based on modified electrodes

2.4.1. Electrodes structured with nanomaterials

Nanomaterials have a significant impact on electrochemical analyses, due to the high surface-to-volume ratios bringing better-conducting characteristics. As result, an increased mass-transport rate with an improved electron transfer rate at the active surface of the electrodes is translated by higher signal-to-noise ratios (89, 90). In the work of Gholivand

et al. (91) a combination of multi-walled carbon nanotubes (MWCNTs), ionic liquid (IL), and copper oxide nanoparticles (CuO) were applied, to obtain an electrode with mechanical stability, electrical conductivity, greater surface area and the guarantee of the GLY-Cu^{2+} complexation. This combination was used to modify the surface of a hollow fiber (HF)/pencil graphite electrode (PGE). The MWCNT-IL provided analyte adsorption capabilities, which added to the stirring of the electrolyte-sample solution was reflected in the very low limit of detection obtained, LOD 0.22 µg L^{-1}. The procedure showed high selectivity in the presence of metal ions, namely AMPA, bialaphos, chlorpyriphos, cypermethrin, glufosinate, and tridemorph pesticides. The accuracy was further checked by the comparison of results obtained for soil and water samples analysis with those enabled by the standard chromatographic method.

Reduced graphene oxide (rGO) is obtained by the reduction of graphite oxide through a variety of routes, such as chemical, thermal and electrochemical (92). The compound owes its excellent electrochemical proprieties to the high conductance of the sp2 hybridized orbital carbon structure and active defect sites (93). Moreover, it increases the mechanical strength of polymer matrices and its surface can be functionalized through π-π staking (94). However, despite being a widely used material for the development of electrochemical sensors, only one work describes its use in the preparation of sensors for GLY. The sensor developed by Setznagl and Cesarino (95) consisted of an rGO base mixed with copper nanoparticles (CuNPs) deposited on a GCE surface. This mixture aims to obtain a highly conductive surface and ensure the formation of a greater number of complexes with the generated copper (II) ions, due to its high availability in CuNPs. The procedure used DPV transduction and was applied to tap water samples, without any pre-treatment, in the linear range of 16.9 to 186 µg L^{-1} GLY.

In turn, graphite can be oxidised to introduce basal plane defects and bear carboxyl and hydroxyl functionalities, which provides better electrochemical activity as well as adsorptive properties. In this context, Santos et al. (96), treated micrometric-size graphite powder with concentrated sulfuric acid at 70 ºC for 12 hours and afterwards mixed with paraffin wax to form a paste used to fulfil the body of 1 mL syringe as electrode body. The electrode was assayed in the determination of GLY by promoting the irreversible oxidation of its amine group at 1.31 V vs Ag/AgCl in BR buffer, pH 6. The implemented procedure based on SWV was applied to spiked groundwater samples and plant extracts with GLY content in the working range of 3043.26 - 202884 µg L^{-1}. Furthermore, the interference of metallic ions and pesticides such as glufosinate, carbaryl, bentazon, monocrotophos, thiram, carbofuran, AMPA, and sarcosine were evaluated.

Therefore, the transducers modified with nanoparticles, such as carbon-based or metallic ones give improved measuring linear ranges and the detection limits improved due to the special electrical properties and larger surface area of the electroactive nanomaterials. Moreover, the modified electrodes can present more stability, sensitivity, and lower signal error ratio, even in the presence of interferences.

2.4.2. Electrodes structured with organometallic compounds

Metal-organic frameworks (MOFs) are complex structures bringing together inorganic and organic units through strong bonds (reticular synthesis) (Figure 2.3a). Organic units are ditopic or polytopic organic carboxylates (and other similar negatively charged molecules), which produce two or three-dimensional (3D) crystalline structures with porosity covering 50% of the MOF when bound to metal-containing units (97). Due to the structure, porosity, and large surface area, MOFs can be used for purification and separation, gas storage, as well as catalysis and sensing applications (98), such as excellent performance in pesticide detection (99). Cao et al. (100) immobilized porous Cu-BTC MOFs using 0.1% Nafion solution on the surface of an ITO electrode (Figure 2.3b). The synthesized MOFs presented electrochemical responsiveness to Cu^{2+}-GLY complexation. The electrode was applied to determine the presence of the herbicide in soybean samples and the low LOD of $2.4x10^{-5}$ µg L^{-1} achieved was due to the high adsorption capacity on the surface. When tested in the presence of AMPA, metals, acetochlor, carbendazim, thiram, and trichlorfon pesticides, signals were biased less than 5%, thus demonstrating good selectivity. Gu et al. (101) reported a different approach, based on copper oxide@mesoporous carbon (CuOx@mC) immobilized with 0.1% wt Nafion solution onto GCE surface (Figure 2.3c). First, the hydrothermal method was used for HKUST-1 synthesis from $Cu(NO_3)_2$ and benzene-1,3,5-tricarboxylic acid. The MOF was then subjected to a carbonization process at 700 °C to obtain CuOx@mC. This material showed enhanced mass transfer properties, mesoporous structure, and amplified current response due to improved Cu(II)/Cu(I) conversion. Therefore, this configuration was tested for GLY detection in acetate buffer pH 5.5 at 0.3 V vs. Ag/AgCl by DPV, demonstrating the very high linear range, between $1.69x10^{-7}$ and 16907 µg L^{-1} and an excellent LOD of $1.30x10^{-7}$ µg L^{-1}. Besides, determinations were not affected by the presence of interferers such as glucose, ascorbic acid, chlorpyrifos, cypermethrin, metal ions, and inorganic anions.

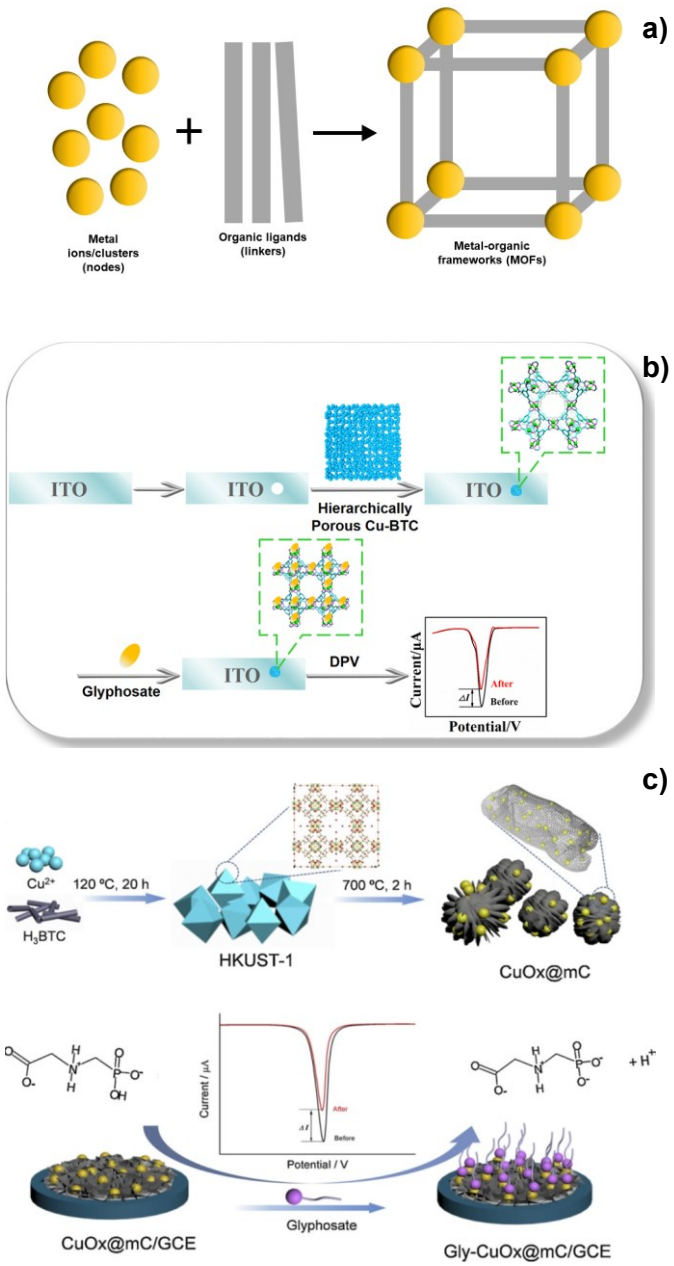


Figure 2.3. a) Schematic illustration of a metal-organic framework assembled from organic linkers and metal nodes; b) Sensor based on the hierarchically porous Cu-BTC MOF material (100); c) formation of CuOx@mC composite and electrochemical analytical principle (101)

In another design, Moraes et al. (102) used copper phthalocyanine (organometallic compound) adsorbed by MWCNTs for the modification of the surface of a GCE (GC/MWCNT/CuPc). The application of this complex is due to its excellent electrocatalytic activity. Furthermore, binding with MWCNTs generates unique properties, such as high specific surface area and strong adsorption capacity, and therefore efficiency for GLY

sensing. In this system, GLY adsorbs to the metal centre of phthalocyanine molecules, guaranteeing the formation of GLY-Cu ion complexes and electrocatalytic activity. Finally, the applied transduction method was DPV, indicating the ability to accomplish the determination of 1 - 50 μg L^{-1} GLY in samples and a LOD of 2.02 μg L^{-1}. In this context, the MOF´s characteristics contribute to the uniqueness of these nanomaterials in the fabrication of electrochemical sensors. Unlike nanoparticles, the structure and position that determines their synthesis, their ultra adsorption capacity, electrical properties, ultra sensitivity and selectivity, and the high availability of metallic materials, guarantee their use for all the chemical species to be analyzed. This condition makes them a promising alternative for monitoring trace levels of organic contaminants.

2.4.3. Electrodes structured with conductive polymers

In search of optimal sensor selectivity and sensitivity, the application of materials such as conductive polymers (CPol), also deemed as “synthetic metals” was exploited. These structures bearing highly conjugated π-bond became attractive as components of electrochemical sensors, due to the good compromise between high electrical conductivity and chemical reversibility. Between them, CPol represents a promising class when envisaging the implementation of modified electrodes with large active surface area, tuned charge transport phenomena, backbone diversity, and the ability for chemical doping (103). For instance, Shrivastava et al. (104) implemented the simultaneous polymerization of pyrrole together with copper electrodeposition on carbon fiber electrodes. The determination relied on the detection of the analyte interaction with copper, while the CPol afforded the within-entrapped metal thus conferring improved physical robustness. The electrode usefulness was assessed by determinations of soil and apple pulp samples performed by DPV within 20 – 12000 μg L^{-1} of GLY in phosphate buffer 0.1 M (pH 7).

On the other hand, polymerization of CPol in the presence of a template molecule confers them a recognizing ability for target compounds (105). Molecularly imprinted polymers (MIPs) have specific printing sites where the molecule of interest fits in shape, size, and functional groups, as shown in Figure 2.4a. This allows MIPs to be highly selective, providing reliability, rapid reaction, efficiency, and easy operation.

Pyrrol (Py) can be easily electropolymerized and therefore is the most commonly described monomer to implement MIPs (106–108). Furthermore, it allows simple functionalization with amino, carboxyl, and phosphonate group recognition sites (109). For instance, Zhang et al. (110) electropolymerized Py on the surface of the gold electrode. For this, the electrode potential was cycled within -1.0 and +1.0 V range at 100 mV s^{-1} scan rate in a solution containing 7.4 mM GLY, 37 mM Py and 0.04 M Britton-Robinson buffer (pH = 5.0). The

afterwards overoxidation of the formed PPy membrane at pH 11 introduced oxygen-containing groups in its backbone which repelled the template GLY while complimentary cavities for the selective recognition process became available. Finally, determinations of GLY in tap water and vegetables were performed by DPV with the MIPPy-modified electrode. The optimized procedure allowed a linear range between 5 - 800 μg L^{-1} and LOD of 0.27 μg L^{-1} GLY. The response to compounds with similar characteristics, such as the AMPA metabolite, and the herbicides chlorpyrifos and aldicarb was also checked. In the paper of Mazouz et al. (12), the electrodeposition of the MIP on a gold electrode by chronoamperometry was alternatively performed. The interaction between GLY and Py was strong as enabled by the determination of two dissociation constants of respectively 0.7±0.3 pM and 1.6±1.4 μM. Then, applying SWV and optimizing the experimental conditions, the GLY detection was performed in distillate water at concentrations as low as 0.1691 ng L^{-1}. Furthermore, the presence of compounds such as gluphosinate ammonium, omethoate, terbuthylazine-2-hydroxy, simetryn, and methidathion did not affect the sensitivity of measurements, even when their concentrations were three times higher. On the other hand, Xu et al. (111) electropolymerized the Py MIP on a Prussian Blue (PB) / Gold Nanoparticles (AuNPs)/ITO modified electrode. In this case, PB worked out as a signal booster. The use of ITO electrodes was justified by their high electrical conductivity and affinity for the deposition of AuNPs and PB. The electrode showed an excellent response in the determination of GLY in corn samples, with a linear concentration range between 400 - 1200 μg L^{-1}, LOD of 92 μg L^{-1}, and recoveries in order of 97.5% to 101%. As an alternative to Py, the preparation of MIPs based on the p-Aminothiophenol (PATP) monomer was described. Its mercapto group brings the ability to establish covalent bonds with metals, thus enabling strong adsorption to the surface of the electrode and stabilizing metallic nanoparticles to avoid spontaneous aggregation (112). Furthermore, the amino group together with the benzene ring provides the recognition sites where the recognition process is accomplished through hydrogen bonds and the π - π stacking interaction. Based on such properties, Do et al. (113) used PATP functionalized with AuNPs, as a monomer in the presence of GLY as a template. The binding of PATP with AuNPs intended the increase of effective binding sites, greater surface area, improved conductivity, stability, and catalytic activity. This so-called MIP-MOF-Au design, was the first, according to this classification, for the detection of GLY. Finally, the evaluation by linear scanning voltammetry (LSV) was verified for its high selectivity and sensitivity, presenting a LOD of 0.8 pg L^{-1}, and the procedure was validated using tap water samples in the presence of AMPA.

Chitosan has a high content of amino and hydroxyl groups in its polysaccharide backbone, which provides flexibility for MIPs preparations. Zouaoui et al. (114) electrodeposited a

GLY-CS suspension on a microarray platform (Figure 2.4b) using CV for 15 scans in the range -1.5 to 0.5 V at the scan rate of 80 mV/s. The array holds four gold microelectrodes, two Ag/AgCl pseudo reference electrodes, and one counter electrode. The template was chemically removed in acid/methanol solution (1:1 v/v). Nyquist plots evidenced that impedance increased proportionally with GLY concentration between $3.1x10^{-4}$ and 50 μg L^{-1}, with a LOD of $1x10^{-6}$ μg L^{-1} and presents high selectivity. No significant response was registered for compounds with similar structures such as GLU, chlorpyrifos, and phosmet. Recently, the same authors described an impedimetric sensor based on a double-layered imprinted electropolymerized polypyrrole doped with cobaltabis (dicarbollide) ions as a solid contact layer between the gold microelectrode surface and the molecularly imprinted chitosan film (CS-MIPs/PPy/Au) (115). The sensor allowed the determination of GLY concentrations between 0.31 pg/mL and 50 ng/mL. The impedance response was assessed by impedance spectroscopy with the fitting model being used for the estimation of the microscopic parameters of the sensors.

N-methacryloyl-L-cysteine, as a product of the reaction between methacryloyl chloride and cysteine, binds metals through sulfhydryl groups and constitutes the monomer of MIP with usefulness in contaminant extraction technologies (eg metals) (116–119), and sensors (120). It was also used as double template MIPs for the simultaneous determination of GLY and GLU (121). The fabrication consisted of an AuNPs nanostructured polymer film on a PGE. Afterwards, the binding of monomers (N-methacryloyl-L-cysteine) through S-Au bonds was promoted (Figure 2.4c). Finally, free radical polymerization proceeded in the presence of the templates, cross-linker, initiator, and MWCNTs, as a prepolymer mixture. The presence of AuNPs and MWCNTs can form nanohybrids and provide superior electron transfer capacity for herbicide oxidation. By using differential pulse anodic stripping voltammetry it was determined a LOD of 0.35 and 0.19 μg L^{-1} for GLY and GLU respectively. Moreover, no interferences were registered.

In this context, it has been demonstrated that conductive polymers with or without polymerization (MIPs) face lower sensitivities due to the lack of conductivity and electrocatalytic activity. Therefore, to increase their electrical conductivity the incorporation of nanoparticles or impregnate them on solid metallic surfaces has been required. The analyzed studies show that nanoparticles accelerate the charge transfer between the electrolyte and the MIP sensor, due to their high specific surface area and excellent conductivity. Furthermore, these combinations efficiently improve the effective adsorption area of the MIPs sensors and lower the detection limits.

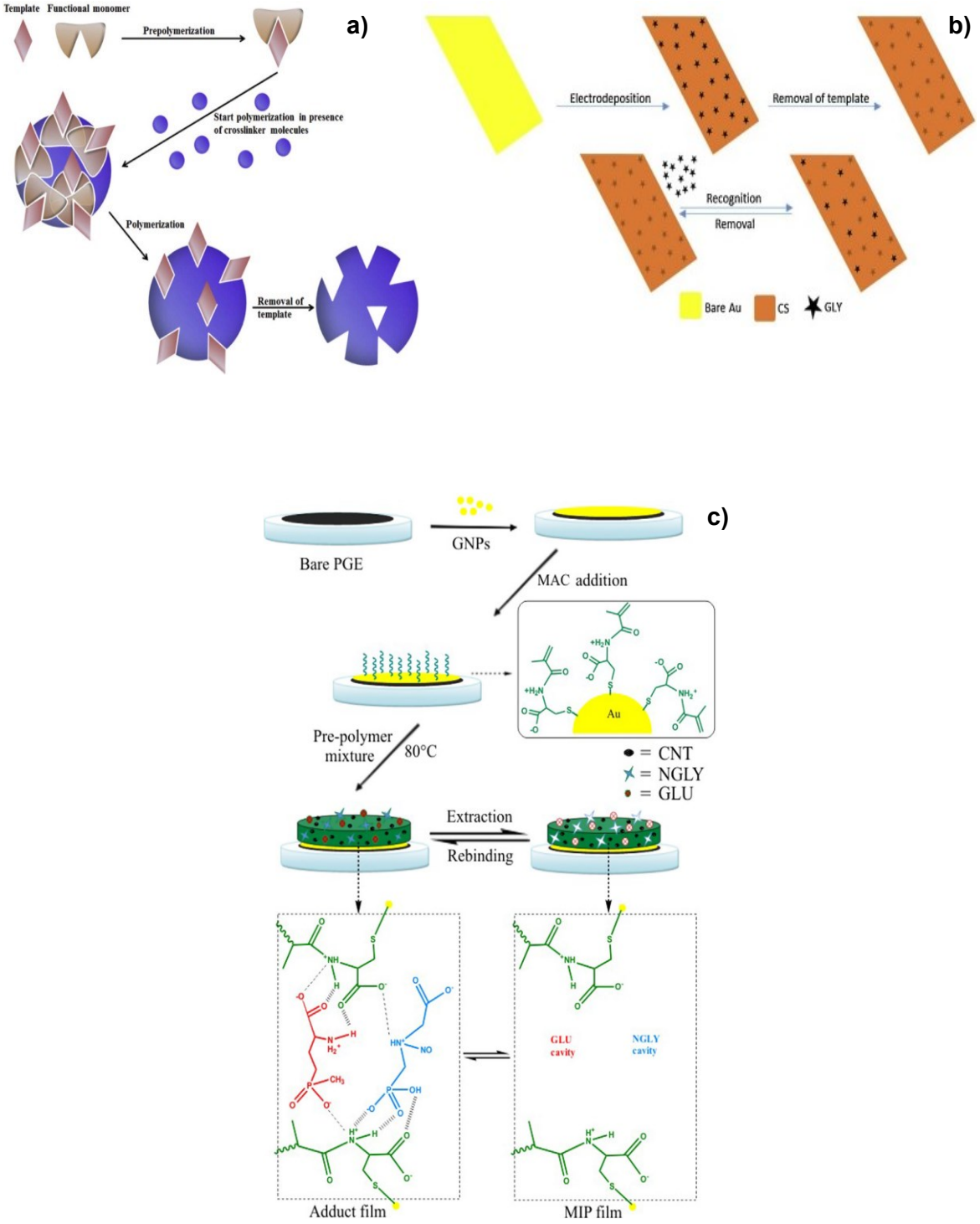


Figure 2.4. a) Schematic representation of the main steps regarding the production of MIP (122); b) Preparation of CS molecularly imprinted film (MIPs/Au) and its recognition for GLY (114); and c) double-template imprinted polymer-modified GNPs-PGE fabrication along with a suggested binding mechanism for the simultaneous analysis of NGLY and GLU (121).

2.5. Biosensors

In the IUPAC classification, biosensors do not appear as an independent group, but are considered a special group of chemical sensors (123). Currently, they have been developed to cope as interdisciplinary technology in diverse activities ranging from food security monitoring (124–127), up to environmental monitoring (128–131). Depending on the nature of the biological recognition element, they can be called organism-based, whole-cell, enzymatic, and antibody biosensors. The last two have been the most widely used because of the combined high selectivity and direct/indirect catalytic properties. Enzyme biosensors can function at moderate potentials to achieve enzyme biocatalysis. However, the general catalytic density can be low due to either molecule's large size and buried catalytic center which turns difficult the electron transfer to the electrode surface. Biosensors translate the analyte recognition through catalytic signals (formation of products in biochemical reaction), catalysis inhibition (an external agent that affects catalytic activity), or immunological reactions (132). The most used strategies for immobilization methods are adsorption, microencapsulation, trapping, covalent bonding, and crosslinking being the key aspect for optimal performance in oriented immobilization (133, 134). On the other hand, in the construction of the receptor element, the conjugation of the biomolecule with nanoparticles such as carbon nanotubes (135–138), conductive polymers (139–142), and metallic nanoparticles (143–145) is presented as a promising platform to improve detection performance (146).

Few enzymes, such as peroxidase, urease, and tyrosine, have been used in the electrochemical detection of GLY. Peroxidases (hydrogen peroxide oxidoreductases) are "heme-containing" glycoproteins that catalyze the oxidation of organic and inorganic compounds with hydrogen peroxide main substrate (147, 148). The oxidizing agent reacts at the catalytic site with the heme iron (III) state of the enzyme to form an intermediate compound that comprises the Fe(IV) oxoferryl center and a porphyrin radical cation (149). This enzyme has been widely studied, for its interesting characteristics such as high activity, fast regeneration, wide pH range, temperature, and covalent bonding with nanoparticles (150, 151). In the reported works GLY and other herbicides are determined as inhibitors of the enzymatic activity of peroxidases. Songa et al. (152–154) immobilized horseradish peroxidase (HRP) enzyme in electrodeposited conductive polymer ink of (poly (2,5-dimethoxyaniline) doped with poly(4-styrenesulfonic acid)), PDMA-PSS, on a gold electrode surface. The performance of the biosensor was evaluated for AMP and GLY or AMPA and GLU in samples of distilled water and corn, respectively. The activity of HRP to reduce H_2O_2 at -0.2 V vs. Ag/AgCl was followed up in phosphate buffer, pH 6.1, by an amperometric measurement made a few minutes after adding the substrate (Figure 2.5a). With the

increase in the concentration of the herbicides, the reducing signal of H_2O_2 diminished. The biosensor was easy to implement, provided an analytical range of 0.25-14.0 µg L^{-1} and a limit of detection of about 1.70 µg L^{-1}.

The determination of GLY at pH 4 was first described by Cahuantzi-Muñoz et al. (155). For this, MWCNTs were immobilized on the surface of the GE electrodes using electrophoretic deposition, for which a stable dispersion of the carbonaceous material in an aqueous solution is required. The HRP immobilization was carried out by immersing the GE/MWCNTs electrode in the enzyme prepared solution, under constant agitation for 18 hours, at 4 ºC. Finally, the resulting GE/MWCNTs-HRP electrode was rinsed with buffer and stored at 4 ºC. At that pH, the GLY molecule bears both positive and negative charges which favour the interaction with the amino acid residues of the biocatalyst. The interaction between the herbicide and the enzyme was assessed by circular dichroism in the UV region, showing the pronounced diminishing effect of the two negative signals at 210, 220 nm associated with the high content of α-helical tertiary structure of HRP. The decrease of H_2O_2 reduction signal at -0.3 V vs. SCE was associated with a blockage of the electroactive sites induced by conformational change during incubation. This biosensor was tested on artificially contaminated extracts of maize kernels exhibiting an excellent linear range between 0.017 and 1860 µg L^{-1}, with a LOD of 0.00022 µg L^{-1}. The inhibition of HRP included in graphite conductive epoxy paste was compared with a carbon-SPE with the bio element chemically immobilized by the biotin-streptavidin complex, by Kergaravat et al. (156) in citrate/phosphate buffer, pH 5. Both sensors were evaluated by SWV, using o-phenylenediamine as a substrate in the presence of H_2O_2. The first electrode was more sensitive regarding the SPE since the linear responses of 0.00016 to 0.5 µg L^{-1} (LOD = $8.5x10^{-5}$ µg L^{-1}) and 0.08 to 11 µg L^{-1} (LOD = 0.045 µg L^{-1}) were respectively obtained.

The biosensor proposed by Roman et al. (157), consisted of HRP immobilized on a polyaniline film (PAni), electrodeposited on the surface of the n-type monocrystalline silicon electrode. PAni can bind to biomolecules and thereby potentiate their biocatalytic properties thus favoring the transfer of electrons between enzyme and substrate. In this case, the detection mechanism consisted of the GLY capacity to inhibit the action of HRP in the oxidation reaction of hydroquinone (HQ) in the presence of H_2O_2, decreasing the signal of electric current, due to the incomplete action of the enzyme. However, the study was only performed at a concentration level of GLY (16.9 µg L^{-1}) to check the biosensor operation, without reporting its linear working range and LOD.

Peroxidases can be obtained from various sources, for this reason, the extraction of atemoya as “atemoya peroxidase” showed that it has high enzymatic activity. This enzyme

was immobilized in a mixture of graphite powder, MWCNTs on nanoclay, and mineral oil and was packed in a plastic syringe to be connected to a copper wire. In this case, the inhibitory effect on the oxidation of hydroquinone in the presence of H_2O_2 was evaluated with SWV. Finally, this design presented stability for eight weeks, with a response range between 100 - 4550 µg L^{-1} and LOD of 30 µg L^{-1}. Besides, its application in real samples was verified, recovering from 94.9 to 108.9% (158).

Bettazzi et al. (159) developed immuno-magnetic assay which consisted of the use of Anti-GLY-IgG modified magnetic particles on a carbon SPE (Figure 2.5b). Chronoamperometry (CRAMP) was applied and the measurement of the oxidation product of the TMB substrate (3,3`,5,5`-tetramethylbenzidine) was carried out in the presence of H_2O_2 by HRP molecules conjugated with GLY as a tracer. This technique was evaluated in a concentration range of 0.03 - 10 µg L^{-1} and LOD of 0.005 µg L^{-1}, applied for analysis in beer samples. Furthermore, it is the only proposal in this category of electrochemical detection immunoassays for GLY.

Other enzymes have also been applied for the development of GLY biosensors. Such is the case of urease, which formed a membrane with AuNPs and trapped in a matrix of guar gum with agarose (160). In this design, the detection system consisted of catalytic inhibition to convert urea to ammonium ions. However, this is the first report on the detection of GLY using potentiometric transduction. The biosensor showed a linear response of 500 - 50000 µg L^{-1} and LOD at 500 µg L^{-1}. It has stability for 180 days and the selectivity was monitored in the presence of other pesticides (dichlorvos, dimethoate, 2–4D, hexaconazole, and paraquat dichloride), which do not show significant changes in urease inhibition.

Sok and Fragoso (161) describe the use of tyrosinase conjugated to carbon nano-onions in a chitosan matrix on a carbon screen-printed electrode. Using AMP, the effect of GLY inhibition on the electrical signal generated by the presence of 3,4-dihydroxy-L-phenylalanine as an enzyme substrate was determined. The presence of carbon nano-onions has a beneficial effect on the sensitivity of the assay. This design was developed for the analysis of GLY in water and rice, achieving a linear quantification range between 2.5 - 1690 µg L^{-1} and a LOD of 1.1 µg L^{-1}. In addition, it has had stability for more than two months, maintaining signal intensities that 90%.

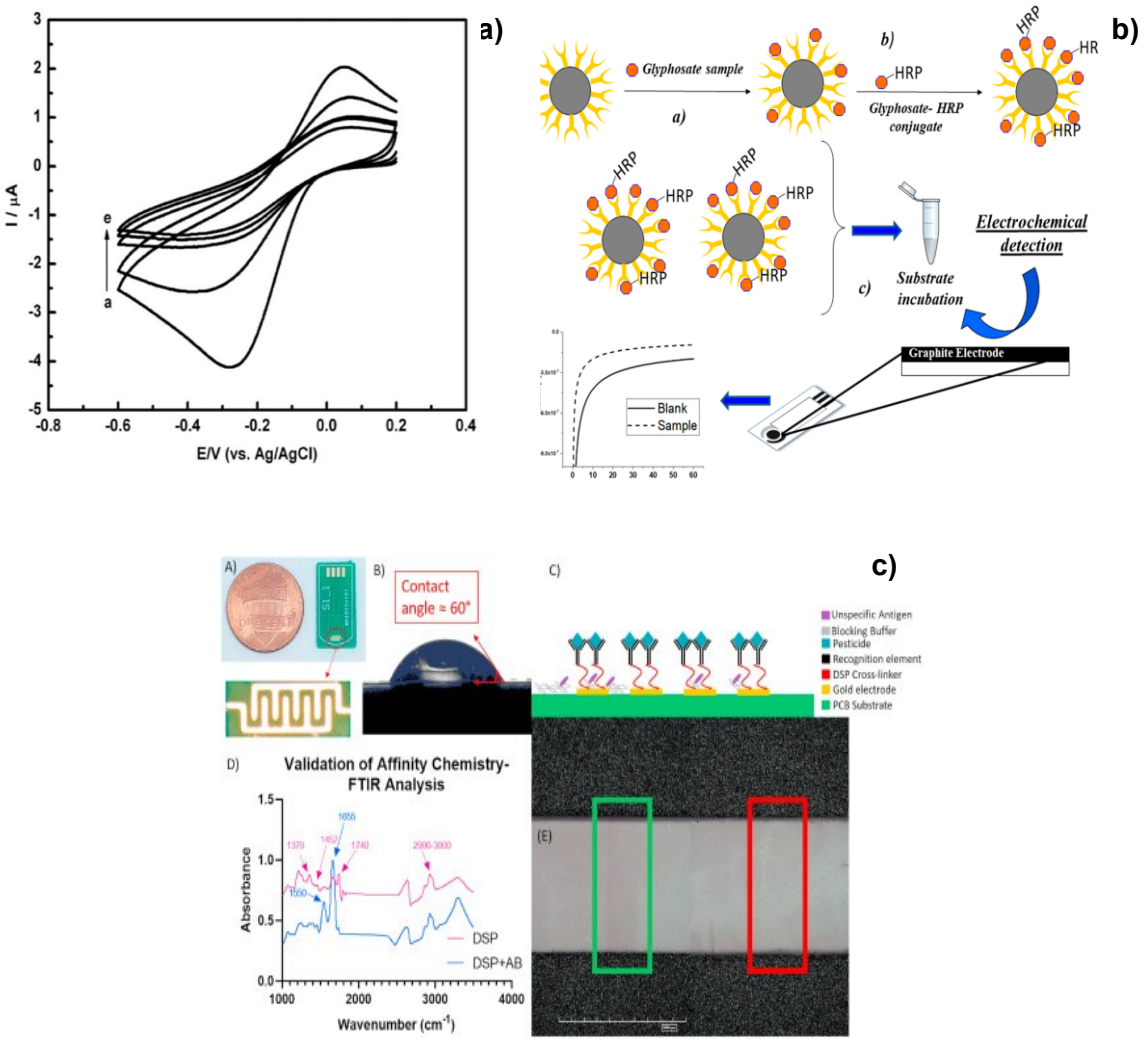


Figure 2.5. a) CV illustration of HRP inhibition effect for H_2O_2 reduction with progressive GLY concentration (154); b) Immuno-magnetic assay of GLY sensing (159); and c) (A)ElectrochemSENSE sensor strip (B) Solid-Liquid interface depicting contact angle made by synthetic buffer PBS on sensor substrate (C) Diagrammatic representation of electrochemical sensor immunoassay stack (D) FTIR Spectrum of DSP (Pink) and DSP-AB (Blue) to validate immunoassay chemistry (162).

On the other hand, Dhamu and Prasad (162) developed a complete portable instrument, designated ElectrochemSENSE, which uses only polyclonal antibodies against GLY, without the need for enzyme interaction. It consisted of a customer reader platform utilizing chronoamperometry as adetection technique and disposable polymer probes with cast interdigitated gold electrodes. The antibodies were fixed on the gold surface using dithiobis(succinimidyl propionate) (DSP) as a cross-linker (Figure 2.5c). The antigen-antibody reaction proceeded for 5 minutes and analyte levels above 10 µg L^{-1} resulted in capacitive current changes when a step voltage of 500 mV was applied for 30 seconds.

Finally, Congur (163) developed, for the first time, an electrochemical biosensor based on passive immobilization of a PGE of double-stranded DNA extracted from fish sperm. The proposal aimed at the monitoring of the genotoxic effect of GLY. It was demonstrated through the decrease in the electrochemical signal of guanine of the DNA, that the herbicides have a marked genotoxic effect. As such, this system corroborated the studies carried out in vitro and in vivo by other authors, though constituting a real alternative for this type of study with other contaminants.

Table 2.2. General and modified electrodes for glyphosate sensing

Sensor configuration	Method	Analyte	Mechanism detection	Sample	Linear range ($\mu g\ L^{-1}$)	LOD ($\mu g\ L^{-1}$)	Ref.
Metal electrodes							
DME	DPP	N-nitrosoglyphosate	N-GLY reduction	Natural water	35 - 210	35	(164)
HDME	DPV	N-nitrosoglyphosate	N-GLY reduction	Soils	500 - 100000 0 - 25000	≤ 2000	(65)
HDME	SWV	N-nitrosoglyphosate	N-GLY reduction	Water	50 - 100000	25	(66)
HMDE	SWV	GLY	GLY-Cu(II) complex	Pure Water. Creek Water.	66.5 – 595.2	22	(71)
Au-SPE	CV SWV AMP	GLY AMPA OMT	GLY-Au complex	Tap water.	338.2 - 50730	338.2	(68)
Au-SPE	AMP	GLY AMPA	GLY-Au complex	Distilled water	-	169.1 1110.4	(88)
Metal deposition-based electrode							

Cu-oxide/hydroxide layers	CV AMP	GLY	GLY-Cu(II) complex	Phosphate Buffer Solution	-	5073	(75)
NiAl-LDH/Pt	AMP	GLY GLU	GLY-Ni(III) complex	Deionized/de carbonated water	1691 - 152190 9908 - 59448	169.1 990.8	(78)
CuAl-LDH/Gr NC	DPV	GLY	GLY-Cu(II) complex	Acetic acid buffer solution	0.5 a 199.5	0.169	(79)
Cu/GC	CV DPV	GLY	GLY-Cu(II) complex	Acetic acid/sodium acetate buffer	67.64 – 1691	31.45	(72)
NPC-modified Cu microelectrode	CV	GLY	GLY-Cu(II) complex	River water	5 - 11	0.676	(73)
Carbon-based electrode							
Graphite powder-Mineral oil/Cu	CV SWV	GLY (monoisopropylamine salt of GLY)	Oxidation of primary amine isoproylammonium cation	Milk Orange juice. Agricultural Formulations.	7.4404 – 473.5	0.3382	(81)

BC-CuHPc/CPE	SWV	GLY	GLY-Cu(II) complex	River water. Orange juice.	50.72 – 676.28	3.38	(84)
CPE/Sg-OS/Eg	SWV	GLY	GLY Oxidation	Soils	1690.7 - 16907	165.7	(85)
GC/rGO-CuNPs	DPV	GLY	GLY-Cu(II) complex	Tap water	16.9 - 186	32	(95)
GrO-PE	SWV	GLY	GLY Oxidation	Groundwater. Soybean. Lettuce extract.	3043.26 - 202884	2.87	(96)
Nanostructured electrodes							
HF-PGE/CuO/MWCNTs-IL	DPV	GLY	GLY-Cu(II) complex	Soil River Water.	0.8455- 186.01	0.22	(91)
Metal-organic frameworks (MOFs)-based electrode							
Cu-BTC/ITO	CV DPV	GLY	GLY-Cu(II) complex	Soybean	0.0001691 - 0.1691 0.1691 - 1691	0.000024	(100)
GC/MWCNT/CuPc	DPV	GLY	GLY-Cu(II) complex	Phosphate buffer solution	140.35- 1674.1	2.02	(102)
CuOx@mC/GCE	DPV	GLY	GLY-Cu(II) complex	Phosphate buffer solution	$1.69x10^{-7}$ - 16907	$1.30x10^{-7}$	(101)

Molecularly imprinted polymer (MIPs)-modified electrodes							
Cu-Ppy/ACF	DPV	GLY	GLY-Cu(II) complex	Phosphate Buffer Solution. Soil. Apple-pulps.	20 - 12000	10	(104)
MIPPy-Au	CV DPV	GLY	Recognition	Cucumber. Tap water.	5 - 800	0.27	(110)
MIPPy-Au	CRAMP SWV	GLY	Recognition	Distilled water	0.0001691 - 0.1691	0.0001691	(12)
AuNPs/PB/GLY-Py-MIP	CV DPV	GLY	Recognition	Spiked samples. Real samples.	400 - 1200	92	(111)
PATP-AuNPs/Au	LSV	GLY	Recognition	Tap water	0.000001 - 1	0.0000008	(113)
CS-MIPs/Au	EIS	GLY	Recognition	River Water	0.00031 - 50	$1x10^{-6}$	(114)
CS-MIPs/PPy/Au	EIS	GLY	Recognition	River water	0.00031 - 50	$1x10^{-6}$	(115)

MIP-modified AuNPS-PGE	DPASV	GLY GLU	Recognition	Water Soil Human serum	3.98 – 176.23 0.54 – 3.96	0.35 0.19	(121)
Biosensing based-electrodes							
HRP/PDMA-PSS/Au	AMP	GLY	Inhibition of the enzymatic activity	Distilled water	0.25 - 14.0	1.70	(154)
HRP/PDMA-PSS/Au	AMP	GLY GLU	Inhibition of the enzymatic activity	Corn	2.0 - 78.0 2.0 - 10.0	0.1 0.1	(152)
HRP/PDMA-PSS/Au	AMP	GLY AMPA	Inhibition of the enzymatic activity	Phosphate buffer solution	- -	0.16 1.0	(153)
GE/MWCNTs-HRP	CV	GLY	Inhibition of the enzymatic activity	Maize Kernels	0.017 - 1860	0.00022	(155)
• C-SPE/biotin-HRP/Streptavidin • GEC-E	SWV	GLY	Inhibition of the enzymatic activity	Groundwater Superficial water	0.08 – 11 0.00016 – 0.5	0.045 8.5×10^{-5}	(156)

n-Si/PAni/HRP	SWV	GLY	Inhibition of the enzymatic activity	Phosphate buffer solution	-	16.9	(157)
Cu/Nanoclay/Graphite powder/MWCNTs/Atemoya Peroxidase	SWV	GLY	Inhibition of the enzymatic activity	Phosphate buffer solution	100 - 4550	30	(158)
SPE/Paramagnetic beads modified with Anti-GLY-IgG / HRP-conjugated glyphosate	CRAMP	GLY	Inhibition of the enzymatic activity	Beer	0.03 - 10	0.005	(159)
Agarose-guar gum-Ureasa-AuNPs	POT	GLY	Inhibition of the enzymatic activity	Tap Water	500 – 50000	500	(160)
SPE/Chi/CNO/TYR	AMP	GLY	Inhibition of the enzymatic activity	Water Rice	2.5 - 1690	1.1	(161)
ElectrochemSENSE	CRAMP	Ag-GLY	Antibody-Antigen binding complex	Run-off/extract solutions obtained from Apples, Strawberries,	10 - 5000	10	(162)

				Bell Peppers and Carrots			
Electronic tongues							
• VET (Ir-Rh-Pt-Au) • VET (Ag-Cu-Co-Ni)	DPV	GLY	Signal pattern	Buffered water	8452.5 - 84525	-	(165)
• Cu • Co	DPV	GLY	Signal pattern	Buffered water	8450 - 845000	-	(166)
• VET (Pt – Co - Cu)	DPV	GLY	Signal pattern	Aqueous environments	16910 - 169100	16910	(167)

2.6. Electronic tongues

Electronic tongues are fast, low-cost and simple tools for liquid analysis, being the response pattern related to one or more constituents by an appropriate chemometric algorithm, commonly multivariate data analysis. They consist of a set of non-selective electrodes made of noble (Au, Pt, Rh, Ir, and Ag) and non-noble (Ni, Co, and Cu) metals encased in a stainless-steel cylinder. These devices are capable of responding with high sensitivity and reproducibility to amines such as GLY if coupling to voltammetric transduction is enabled (168).

In the research of Martínez Gil et al. (165), a working electrode composed of four noble metals (Ir, Rh, Pt, and Au) and a second electrode composed of four non-noble metals (Ag, Cu, Co, and Ni) were used (Figure 2.6a), applying DPV. The objective of this system is to create and validate a mathematical model to quantify GLY, and also, to discriminate the presence of common contaminants in natural water bodies that can be possible interferences, such as humic substances and fertilizers (based on ammonium nitrate). Finally, after building and validating several mathematical models with the software SOLO © (Eigenvector Research Inc.), it was determined that the best one resulted from the combination of rhodium, copper, and cobalt electrodes. On the other hand, Laguarda-Miro et al. (166), used the same electronic tongue as Martínez Gil et al. (165), with the variant of signal testing for each metal with DPV (Figure 2.6b). Finally, they chose copper and cobalt because they are more sensitive. After the optimization, two mathematical methods were evaluated (artificial neural network (ANN) and statistical methods), which were developed for the prediction of GLY in aqueous solutions, with the objective of a projection for its detection in natural water bodies. Bataller et al. (167) also used an electronic tongue composed of three working electrodes (Pt, Co, and Cu) encapsulated in a methacrylate cylinder. The electrical signals were also obtained by DPV. In this case, using partial least square methodologie they developed a model that allowed to determine GLY even in the presence of interferents (humic acid and Ca^{2+}). However, although these studies are presented as reliable methods for predicting GLY in natural water bodies, in the presence of interferents, they are not identified as sensitive since the determined concentrations were very high (8452.5 - 84525 μg L^{-1} (165), 8452.5 - 845250 μg L^{-1} (166) and 16905 - 169050 μg L^{-1} (167).

Although electronic tongues are striking for being a multisensor array, the main drawbacks of this technology are the numerous measurements to obtain a qualitative/quantitative selective standard signal model, discriminating interfering signals. Moreover, one of the main challenges of this technology lies in the substantial scope of miniaturization and integration into optimized systems for commercial applications.

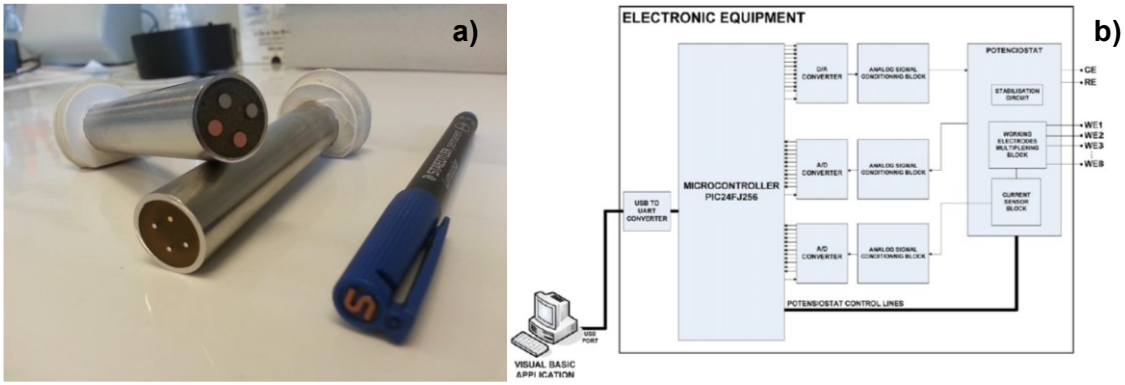


Figure 2.6. a) Electronic tongues of Martínez Gil et al. (165); b) System designed of Laguarda-Miro et al. (166)

2.7. Conclusions and prospects

The harmful properties of GLY to health and the environment have been demonstrated recently, being the appropriate momentum for the development of several mechanisms for its detection. This chapter presents different electrode configurations for the electrochemical detection of GLY. Several parameters involved in electrochemical measurements are briefly explained, such as the electrochemical transduction techniques based on the electrical measurement signals, receptor materials of the developed electrodes, and the behavior of detection mechanisms.

- Electrochemical sensors provide a powerful analytical tool for GLY detection systems. These are particularly attractive because they are small devices with easy portability, high sensitivity, selectivity, and affordable construction investment.
- For better electrocatalytic activity in the detection of GLY, the electrodes have been subjected to chemical and physical modifications. These have been developed extensively by exploring new immobilization designs and surface supports, new receptors or interface materials including materials based on metallic oxides and hydroxides, carbon, nanomaterials, metal-organic frameworks, conductive polymers, molecularly imprinted polymers, and biomaterials as enzymes.
- Nanomaterials play an important role in respecting the biosensors signal transducer. Their physical/chemical characteristics enable a good immobilization of the biological entities and a better interaction of the analyte with the electrode surface. The incorporation of nanoparticles improves the electrode's performances in terms of sensitivity and selectivity. In particular, MOFs and MIPs have been used for GLY determination at trace levels, which has never been reached by optical methods.

- These materials are employed as conventional electrode modifiers such as HDME, glassy carbon, gold, copper, nickel, platinum, carbon paste, graphite, pencil graphite, and indium tin oxide.
- These modified platforms have been applied in different electrochemical techniques, such as voltammetry, amperometry, potentiometry, and impedance, for the detection of GLY with high sensitivity and selectivity, wide dynamic range, and low detection limits.
- The exponential growth of electrochemical sensors development and applications has drawn the attention of many researchers who have demonstrated their flexibility as detectors. This is because different materials with affinity for GLY can be tested, each showing its detection mechanism and performance.

The electrochemical methods proposed for the detection of GLY and their applications are still scarce, although excellent sensitivity and selectivity are demonstrated.

2.8. References

1. Heap I, Duke SO. Overview of glyphosate-resistant weeds worldwide. *Pest Manag Sci* 2018; 74: 1040–1049.
2. Zhu Y, Zhang F, Tong C, et al. Determination of glyphosate by ion chromatography. *J Chromatogr A* 1999; 850: 297–301.
3. Philipp Schledorn MK. Detection of Glyphosate Residues in Animals and Humans. *J Environ Anal Toxicol*; 04. Epub ahead of print 2014. DOI: 10.4172/2161-0525.1000210.
4. Brito IP, Tropaldi L, Carbonari CA, et al. Hormetic effects of glyphosate on plants. *Pest Manag Sci* 2018; 74: 1064–1070.
5. Gauglitz G, Wimmer B, Melzer T, et al. Glyphosate analysis using sensors and electromigration separation techniques as alternatives to gas or liquid chromatography. *Anal Bioanal Chem* 2018; 410: 725–746.
6. Undabeytia T, Morillo E, Maqueda C. FTIR Study of Glyphosate−Copper Complexes. *J Agric Food Chem* 2002; 50: 1918–1921.
7. Morillo E, Undabeytia T, Maqueda C, et al. Glyphosate adsorption on soils of different characteristics.: Influence of copper addition. *Chemosphere* 2000; 40: 103–107.
8. Jacob GS, Garbow JR, Hallas LE, et al. Metabolism of Glyphosate in Pseudomonas sp. Strain LBr. *Appl Environ Microbiol* 1988; 54: 2953–2958.
9. Duke SO, Powles SB. Glyphosate: a once-in-a-century herbicide. *Pest Manag Sci* 2008; 64: 319–325.

10. Guyton KZ, Loomis D, Grosse Y, et al. Carcinogenicity of tetrachlorvinphos, parathion, malathion, diazinon, and glyphosate. *Lancet Oncol* 2015; 16: 490–491.
11. Benbrook CM. Trends in glyphosate herbicide use in the United States and globally. *Environ Sci Eur* 2016; 28: 3.
12. Mazouz Z, Rahali S, Fourati N, et al. Highly selective polypyrrole MIP-based gravimetric and electrochemical sensors for picomolar detection of glyphosate. *Sensors (Switzerland)*; 17. Epub ahead of print 2017. DOI: 10.3390/s17112586.
13. WHO/FAO. *Report of the joint meeting of the FAO Panel of Experts on pesticide residues in food and the environment and the WHO Core Assessment Group on Pesticide Residues (JMPR).* Rome: World Health Organization/Food and Agriculture Organization of the United Nations., http://www.fao.org/ag/agp/agpp/Pesticid/JMPR/DOWNLOAD/2004_rep/report2004jmpr.pdf (September 2004).
14. Connolly A, Basinas I, Jones K, et al. Characterising glyphosate exposures among amenity horticulturists using multiple spot urine samples. *Int J Hyg Environ Health* 2018; 221: 1012–1022.
15. Zouaoui K, Dulaurent S, Gaulier JM, et al. Determination of glyphosate and AMPA in blood and urine from humans: About 13 cases of acute intoxication. *Forensic Sci Int* 2013; 226: e20–e25.
16. Seneff S, Swanson N, Li C. Aluminum and Glyphosate Can Synergistically Induce Pineal Gland Pathology: Connection to Gut Dysbiosis and Neurological Disease. *Agricultural Sciences* 2015; 06: 42–70.
17. Samsel A, Seneff S. Glyphosate's Suppression of Cytochrome P450 Enzymes and Amino Acid Biosynthesis by the Gut Microbiome: Pathways to Modern Diseases. *Entropy* 2013; 15: 1416–1463.
18. Mesnage R, Defarge N, Spiroux de Vendômois J, et al. Potential toxic effects of glyphosate and its commercial formulations below regulatory limits. *Food and Chemical Toxicology* 2015; 84: 133–153.
19. Mesnage R, Phedonos A, Biserni M, et al. Evaluation of estrogen receptor alpha activation by glyphosate-based herbicide constituents. *Food Chem Toxicol* 2017; 108: 30–42.
20. Thongprakaisang S, Thiantanawat A, Rangkadilok N, et al. Glyphosate induces human breast cancer cells growth via estrogen receptors. *Food Chem Toxicol* 2013; 59: 129–136.

21. Sritana N, Suriyo T, Kanitwithayanun J, et al. Glyphosate induces growth of estrogen receptor alpha positive cholangiocarcinoma cells via non-genomic estrogen receptor/ERK1/2 signaling pathway. *Food Chem Toxicol* 2018; 118: 595–607.
22. Manas F, Peralta L, Raviolo J, et al. Genotoxicity of glyphosate assessed by the comet assay and cytogenetic tests. *Environ Toxicol Pharmacol* 2009; 28: 37–41.
23. Kwiatkowska M, Reszka E, Wozniak K, et al. DNA damage and methylation induced by glyphosate in human peripheral blood mononuclear cells (in vitro study). *Food Chem Toxicol* 2017; 105: 93–98.
24. Koller VJ, Fürhacker M, Nersesyan A, et al. Cytotoxic and DNA-damaging properties of glyphosate and Roundup in human-derived buccal epithelial cells. *Arch Toxicol* 2012; 86: 805–813.
25. Wozniak E, Sicinska P, Michalowicz J, et al. The mechanism of DNA damage induced by Roundup 360 PLUS, glyphosate and AMPA in human peripheral blood mononuclear cells - genotoxic risk assessement. *Food Chem Toxicol* 2018; 120: 510–522.
26. Richard S, Moslemi S, Sipahutar H, et al. Differential effects of glyphosate and roundup on human placental cells and aromatase. *Environ Health Perspect* 2005; 113: 716–720.
27. Hokanson R, Fudge R, Chowdhary R, et al. Alteration of estrogen-regulated gene expression in human cells induced by the agricultural and horticultural herbicide glyphosate. *Hum Exp Toxicol* 2007; 26: 747–752.
28. Gasnier C, Dumont C, Benachour N, et al. Glyphosate-based herbicides are toxic and endocrine disruptors in human cell lines. *Toxicology* 2009; 262: 184–191.
29. Cattani D, de Liz Oliveira Cavalli VL, Heinz Rieg CE, et al. Mechanisms underlying the neurotoxicity induced by glyphosate-based herbicide in immature rat hippocampus: Involvement of glutamate excitotoxicity. *Toxicology* 2014; 320: 34–45.
30. Parajuli K, Zhang Q, Liu S, et al. Aminomethylphosphonic Acid and Methoxyacetic Acid Induce Apoptosis in Prostate Cancer Cells. *Int J Mol Sci* 2015; 16: 11750–11765.
31. Li Q, Lambrechts MJ, Zhang Q, et al. Glyphosate and AMPA inhibit cancer cell growth through inhibiting intracellular glycine synthesis. *Drug Des Devel Ther* 2013; 7: 635–643.
32. IARC. *Some organophosphate insecticides and herbicides*. Leon: International Agency for Research on Cancer, https://monographs.iarc.fr/wp-content/uploads/2018/07/mono112.pdf (2015).
33. Efsa. Conclusion on the peer review of the pesticide risk assessment of the active substance glyphosate. *Efsa Journal* 2015; 13: 107.

34. EPA. National Primary Drinking Water Regulations, https://www.epa.gov/ground-water-and-drinking-water/national-primary-drinking-water-regulations (2009).
35. Wang S, Liu B, Yuan D, et al. A simple method for the determination of glyphosate and aminomethylphosphonic acid in seawater matrix with high performance liquid chromatography and fluorescence detection. *Talanta* 2016; 161: 700–706.
36. Khrolenko M v, Wieczorek PP. Determination of glyphosate and its metabolite aminomethylphosphonic acid in fruit juices using supported-liquid membrane preconcentration method with high-performance liquid chromatography and UV detection after derivatization with p-toluenesulphonyl chloride. *J Chromatogr A* 2005; 1093: 111–117.
37. Sun L, Kong D, Gu W, et al. Determination of glyphosate in soil/sludge by high performance liquid chromatography. *J Chromatogr A* 2017; 1502: 8–13.
38. Guo H, Riter LS, Wujcik CE, et al. Direct and sensitive determination of glyphosate and aminomethylphosphonic acid in environmental water samples by high performance liquid chromatography coupled to electrospray tandem mass spectrometry. *J Chromatogr A* 2016; 1443: 93–100.
39. Guo H, Wang H, Zheng J, et al. Sensitive and rapid determination of glyphosate, glufosinate, bialaphos and metabolites by UPLC–MS/MS using a modified Quick Polar Pesticides Extraction method. *Forensic Sci Int* 2018; 283: 111–117.
40. Chen M-X, Cao Z-Y, Jiang Y, et al. Direct determination of glyphosate and its major metabolite, aminomethylphosphonic acid, in fruits and vegetables by mixed-mode hydrophilic interaction/weak anion-exchange liquid chromatography coupled with electrospray tandem mass spectrometry. *J Chromatogr A* 2013; 1272: 90–99.
41. Bernal J, Martin MT, Soto ME, et al. Development and Application of a Liquid Chromatography-Mass Spectrometry Method To Evaluate the Glyphosate and Aminomethylphosphonic Acid Dissipation in Maize Plants after Foliar Treatment. *J Agric Food Chem* 2012; 60: 4017–4025.
42. Tseng S-H, Lo Y-W, Chang P-C, et al. Simultaneous Quantification of Glyphosate, Glufosinate, and Their Major Metabolites in Rice and Soybean Sprouts by Gas Chromatography with Pulsed Flame Photometric Detector. *J Agric Food Chem* 2004; 52: 4057–4063.
43. Zhang W, Feng Y, Ma L, et al. A method for determining glyphosate and its metabolite aminomethyl phosphonic acid by gas chromatography-flame photometric detection. *J Chromatogr A* 2018; 1589: 116–121.

44. Hu JY, Chen CL, Li JZ. A simple method for the determination of glyphosate residues in soil by capillary gas chromatography with nitrogen phosphorus. *Journal of Analytical Chemistry* 2008; 63: 371–375.
45. Royer A, Beguin S, Tabet JC, et al. Determination of glyphosate and aminomethylphosphonic acid residues in water by gas chromatography with tandem mass spectrometry after exchange ion resin purification and derivatization. Application on vegetable matrixes. *Anal Chem* 2000; 72: 3826–3832.
46. Motojyuku M, Saito T, Akieda K, et al. Determination of glyphosate, glyphosate metabolites, and glufosinate in human serum by gas chromatography–mass spectrometry. *Journal of Chromatography B* 2008; 875: 509–514.
47. Guo Z-X, Cai Q, Yang Z. Determination of glyphosate and phosphate in water by ion chromatography—inductively coupled plasma mass spectrometry detection. *J Chromatogr A* 2005; 1100: 160–167.
48. See HH, Hauser PC, Sanagi MM, et al. Dynamic supported liquid membrane tip extraction of glyphosate and aminomethylphosphonic acid followed by capillary electrophoresis with contactless conductivity detection. *J Chromatogr A* 2010; 1217: 5832–5838.
49. Chiu HY, Lin ZY, Tu HL, et al. Analysis of glyphosate and aminomethylphosphonic acid by capillary electrophoresis with electrochemiluminescence detection. *J Chromatogr A* 2008; 1177: 195–198.
50. Chang SY, Liao C-H. Analysis of glyphosate, glufosinate and aminomethylphosphonic acid by capillary electrophoresis with indirect fluorescence detection. *J Chromatogr A* 2002; 959: 309–315.
51. Lanaro R, Costa JL, Cazenave SO, et al. Determination of herbicides paraquat, glyphosate, and aminomethylphosphonic acid in marijuana samples by capillary electrophoresis. *J Forensic Sci* 2015; 60 Suppl 1: S241-7.
52. Rubio F, Veldhuis LJ, Clegg BS, et al. Comparison of a direct ELISA and an HPLC method for glyphosate determinations in water. *J Agric Food Chem* 2003; 51: 691–696.
53. Clegg BS, Stephenson GR, Hall JC. Development of an enzyme-linked immunosorbent assay for the detection of glyphosate. *J Agric Food Chem* 1999; 47: 5031–5037.
54. Selvi AA, Sreenivasa MA, Manonmani HK. Enzyme-linked immunoassay for the detection of glyphosate in food samples using avian antibodies. *Food Agric Immunol* 2011; 22: 217–228.

55. Sánchez-Bayo F, Hyne R v, Desseille KL. An amperometric method for the detection of amitrole, glyphosate and its aminomethyl-phosphonic acid metabolite in environmental waters using passive samplers. *Anal Chim Acta* 2010; 675: 125–131.
56. Sato K, Jin JY, Takeuchi T, et al. Integrated pulsed amperometric detection of glufosinate, bialaphos and glyphosate at gold electrodes in anion-exchange chromatography. *J Chromatogr A* 2001; 919: 313–320.
57. Coutinho CFB, Coutinho LFM, Lanças FM, et al. Development of instrumentation for amperometric and coulometric detection using ultramicroelectrodes. *J Braz Chem Soc* 2008; 19: 131–139.
58. Coutinho CFB, Coutinho LFM, Mazo LH, et al. Direct determination of glyphosate using hydrophilic interaction chromatography with coulometric detection at copper microelectrode. *Anal Chim Acta* 2007; 592: 30–35.
59. Arkan T, Molnár-Perl I. The role of derivatization techniques in the analysis of glyphosate and aminomethyl-phosphonic acid by chromatography. *Microchemical Journal* 2015; 121: 99–106.
60. Sakamoto S, Putalun W, Vimolmangkang S, et al. Enzyme-linked immunosorbent assay for the quantitative/qualitative analysis of plant secondary metabolites. *J Nat Med* 2018; 72: 32–42.
61. Islam MA, Mahbub P, Nesterenko PN, et al. Prospects of pulsed amperometric detection in flow-based analytical systems - A review. *Anal Chim Acta* 2019; 1052: 10–26.
62. Friestad HO, Brønstad JO. Improved polarographic method for determination of glyphosate herbicide in crops, soil, and water. *Journal of the Association of Official Analytical Chemists* 1985; 68: 76–79.
63. Zuman P. Role of mercury electrodes in contemporary analytical chemistry. *Electroanalysis* 2000; 12: 1187–1194.
64. Christian GD. Pulse polarography at the hanging mercury drop electrode. *J Electroanal Chem Interfacial Electrochem* 1969; 22: 333–337.
65. Daňhel A, Moreira JC, Jacob S, et al. Influence of the soil organic matter content on voltammetric determination of derivatised glyphosate in herbicide contaminated soils. *Collect Czechoslov Chem Commun* 2011; 76: 1263–1275.
66. Teófilo RF, Reis EL, Reis C, et al. Experimental design employed to square wave voltammetry response optimization for the glyphosate determination. *J Braz Chem Soc* 2004; 15: 865–871.

67. Coutinho CFB, Mazo LH. Estudo voltamétrico e espectrofotométrico do complexo Cu(II)-Glifosato. *Pesticidas: Revista de Ecotoxicologia e Meio Ambiente*; 17. Epub ahead of print 2007. DOI: http://dx.doi.org/10.5380/pes.v17i0.4775.
68. Noori JS, Dimaki M, Mortensen J, et al. Detection of glyphosate in drinking water: A fast and direct detection method without sample pretreatment. *Sensors (Switzerland)*; 18. Epub ahead of print 2018. DOI: 10.3390/s18092961.
69. Coutinho CFB, Mazo LH. Complexos metálicos com o herbicida glifosato: revisão. *Quim Nova* 2005; 28: 1038.
70. Purgel M, Takacs Z, Jonsson CM, et al. Glyphosate complexation to aluminium(III). An equilibrium and structural study in solution using potentiometry, multinuclear NMR, ATR-FTIR, ESI-MS and DFT calculations. *J Inorg Biochem* 2009; 103: 1426–1438.
71. dos Santos SC, Galli A, Felsner ML, et al. Development of an electroanalytical methodology for determination of pesticide glyphosate in environmental samples. *Revista Virtual de Quimica* 2014; 6: 866–883.
72. Aguirre MDC, Urreta SE, Gomez CG. A Cu2+-Cu/glassy carbon system for glyphosate determination. *Sens Actuators B Chem* 2019; 284: 675–683.
73. Regiart M, Kumar A, Gonçalves JM, et al. An Electrochemically Synthesized Nanoporous Copper Microsensor for Highly Sensitive and Selective Determination of Glyphosate. *ChemElectroChem* 2020; 7: 1558–1566.
74. Heineke D, Franklin SJ, Raymond KN. Coordination chemistry of glyphosate: Structural and spectroscopic characterization of bis (glyphosate) metal (III) complexes. *Inorg Chem* 1994; 33: 2413–2421.
75. Sierra EV, Méndez MA, Sarria VM, et al. Electrooxidación de glifosato sobre electrodos de níquel y cobre. *Quim Nova* 2008; 31: 220–226.
76. Therese GHA, Kamath PV. Electrochemical Synthesis of Metal Oxides and Hydroxides. *Chemistry of Materials* 2000; 12: 1195–1204.
77. Leckie HP. The Anodic Polarization Behavior of Copper. *J Electrochem Soc* 1970; 117: 1478.
78. Khenifi A, Derriche Z, Forano C, et al. Glyphosate and glufosinate detection at electrogenerated NiAl-LDH thin films. *Anal Chim Acta* 2009; 654: 97–102.
79. Zhang C, Liang X, Lu Y, et al. Performance of CuAl-LDH/Gr Nanocomposite-Based Electrochemical Sensor with Regard to Trace Glyphosate Detection in Water. *Sensors* 2020; 20: 4146-undefined.
80. Švancara I, Vytřas K, Barek J, et al. Carbon Paste Electrodes in Modern Electroanalysis. *Crit Rev Anal Chem* 2001; 31: 311–345.

81. Oliveira PC, Maximiano EM, Oliveira PA, et al. Direct electrochemical detection of glyphosate at carbon paste electrode and its determination in samples of milk, orange juice, and agricultural formulation. *J Environ Sci Health B* 2018; 53: 817–823.
82. Pintado S, Amaro RR, Mayen M, et al. Electrochemical Determination of the Glyphosate Metabolite Aminomethylphosphonic Acid (AMPA) in Drinking Waters with an Electrodeposited Copper Electrode. *Int J Electrochem Sci* 2012; 7: 305–312.
83. Pintado S, Montoya MR, Rodriguez-Amaro R, et al. Electrochemical Determination of Glyphosate in Waters Using Electrogenerated Copper Ions. *Int J Electrochem Sci* 2012; 7: 2523–2530.
84. Wong A, de Lima DG, Ferreira PA, et al. Voltammetric sensing of glyphosate in different samples using carbon paste electrode modified with biochar and copper(II) hexadecafluoro-29H,31 phtalocyanine complex. *J Appl Electrochem* 2021; 51: 761–768.
85. Mbokana JGY, Dedzo GK, Ngameni E. Grafting of organophilic silane in the interlayer space of acid-treated smectite: Application to the direct electrochemical detection of glyphosate. *Appl Clay Sci* 2020; 188: 105513.
86. Li M, Li YT, Li DW, et al. Recent developments and applications of screen-printed electrodes in environmental assays-A review. *Anal Chim Acta* 2012; 734: 31–44.
87. Alkire RC, Bartlett PN, Lipkowski J. *Electrochemistry of Carbon Electrodes*. Wiley, https://books.google.com.ec/books?id=ChglCgAAQBAJ (2015).
88. Habekost A. Rapid and sensitive spectroelectrochemical and electrochemical detection of glyphosate and AMPA with screen-printed electrodes. *Talanta* 2017; 162: 583–588.
89. Martín-Yerga D, González-García MB, Costa-García A. Electrochemical determination of mercury: A review. *Talanta* 2013; 116: 1091–1104.
90. Li M, Gou H, Al-Ogaidi I, et al. Nanostructured Sensors for Detection of Heavy Metals: A Review. *ACS Sustain Chem Eng* 2013; 1: 713–723.
91. Gholivand MB, Akbari A, Norouzi L. Development of a novel hollow fiber- pencil graphite modified electrochemical sensor for the ultra-trace analysis of glyphosate. *Sens Actuators B Chem* 2018; 272: 415–424.
92. Rowley-Neale SJ, Randviir EP, Abo Dena AS, et al. An overview of recent applications of reduced graphene oxide as a basis of electroanalytical sensing platforms. *Appl Mater Today* 2018; 10: 218–226.
93. Robinson JT, Perkins FK, Snow ES, et al. Reduced Graphene Oxide Molecular Sensors. *Nano Lett* 2008; 8: 3137–3140.

94. Backes C, Abdelkader AM, Alonso C, et al. Production and processing of graphene and related materials. *2d Mater*; 7. Epub ahead of print 29 January 2020. DOI: 10.1088/2053-1583/ab1e0a.
95. Setznagl S, Cesarino I. Copper nanoparticles and reduced graphene oxide modified a glassy carbon electrode for the determination of glyphosate in water samples. *Int J Environ Anal Chem* 2020; 1–13.
96. Santos JS, Pontes MS, Santiago EF, et al. An efficient and simple method using a graphite oxide electrochemical sensor for the determination of glyphosate in environmental samples. *Science of The Total Environment* 2020; 749: 142385.
97. Furukawa H, Cordova KE, O'Keeffe M, et al. The Chemistry and Applications of Metal-Organic Frameworks. *Science (1979)* 2013; 341: 1230444.
98. Ghosh SK, Kitagawa S. 1 - Introduction. *Metal-Organic Frameworks (MOFs) for Environmental Applications* 2019; 1–4.
99. Vikrant K, Tsang DCW, Raza N, et al. Potential Utility of Metal–Organic Framework-Based Platform for Sensing Pesticides. *ACS Appl Mater Interfaces* 2018; 10: 8797–8817.
100. Cao Y, Wang L, Shen C, et al. An electrochemical sensor on the hierarchically porous Cu-BTC MOF platform for glyphosate determination. *Sens Actuators B Chem* 2019; 487–494.
101. Gu C, Wang Q, Zhang L, et al. Ultrasensitive non-enzymatic pesticide electrochemical sensor based on HKUST-1-derived copper oxide @ mesoporous carbon composite. *Sens Actuators B Chem* 2020; 305: 127478.
102. Moraes FC, Mascaro LH, Machado SAS, et al. Direct electrochemical determination of glyphosate at copper phthalocyanine/multiwalled carbon nanotube film electrodes. *Electroanalysis* 2010; 22: 1586–1591.
103. Marinho MIC, Cabral MF, Mazo LH. Is the poly (methylene blue)-modified glassy carbon electrode an adequate electrode for the simple detection of thiols and amino acid-based molecules? *Journal of Electroanalytical Chemistry* 2012; 685: 8–14.
104. Shrivastava S, Kumar A, Verma N, et al. Voltammetric Detection of Aqueous Glyphosate on a Copper and Poly(Pyrrole)-electromodified Activated Carbon Fiber. *Electroanalysis*; n/a. Epub ahead of print 2020. DOI: https://doi.org/10.1002/elan.202060408.
105. Pardieu E, Cheap H, Vedrine C, et al. Molecularly imprinted conducting polymer based electrochemical sensor for detection of atrazine. *Anal Chim Acta* 2009; 649: 236–245.

106. Genies EM, Bidan G, Diaz AF. Spectroelectrochemical study of polypyrrole films. *J Electroanal Chem Interfacial Electrochem* 1983; 149: 101–113.
107. Diaz AF, Castillo JI, Logan JA, et al. Electrochemistry of conducting polypyrrole films. *J Electroanal Chem Interfacial Electrochem* 1981; 129: 115–132.
108. Jain R, Jadon N, Pawaiya A. Polypyrrole based next generation electrochemical sensors and biosensors: A review. *TrAC Trends in Analytical Chemistry* 2017; 97: 363–373.
109. Ramanavičius A, Ramanavičienė A, Malinauskas A. Electrochemical sensors based on conducting polymer—polypyrrole. *Electrochim Acta* 2006; 51: 6025–6037.
110. Zhang C, She Y, Li T, et al. A highly selective electrochemical sensor based on molecularly imprinted polypyrrole-modified gold electrode for the determination of glyphosate in cucumber and tap water. *Anal Bioanal Chem* 2017; 409: 7133–7144.
111. Xu J, Zhang Y, Wu K, et al. A molecularly imprinted polypyrrole for ultrasensitive voltammetric determination of glyphosate. *Microchimica Acta* 2017; 184: 1959–1967.
112. Zhang J, Wang Y, Lv R, et al. Electrochemical tolazoline sensor based on gold nanoparticles and imprinted poly-o-aminothiophenol film. *Electrochim Acta* 2010; 55: 4039–4044.
113. Do MH, Florea A, Farre C, et al. Molecularly imprinted polymer-based electrochemical sensor for the sensitive detection of glyphosate herbicide. *Int J Environ Anal Chem* 2015; 95: 1489–1501.
114. Zouaoui F, Bourouina-Bacha S, Bourouina M, et al. Electrochemical impedance spectroscopy determination of glyphosate using a molecularly imprinted chitosan. *Sens Actuators B Chem* 2020; 309: 127753.
115. Zouaoui F, Bourouina-Bacha S, Bourouina M, et al. Experimental Study and Mathematical Modeling of a Glyphosate Impedimetric Microsensor Based on Molecularly Imprinted Chitosan Film. *Chemosensors* 2020; 8: 104-undefined.
116. Aslıyüce S, Bereli N, Uzun L, et al. Ion-imprinted supermacroporous cryogel, for in vitro removal of iron out of human plasma with beta thalassemia. *Sep Purif Technol* 2010; 73: 243–249.
117. Andac M, Mirel S, Senel S, et al. Ion-imprinted beads for molecular recognition based mercury removal from human serum. *Int J Biol Macromol* 2007; 40: 159–166.
118. Esen C, Andac M, Bereli N, et al. Highly selective ion-imprinted particles for solid-phase extraction of Pb2+ ions. *Materials Science and Engineering: C* 2009; 29: 2464–2470.

119. Özkara S, Andaç M, Karakoç V, et al. Ion-imprinted PHEMA based monolith for the removal of Fe3+ ions from aqueous solutions. *J Appl Polym Sci* 2011; 120: 1829–1836.
120. Göçenoğlu Sarıkaya A, Osman B, Çam T, et al. Molecularly imprinted surface plasmon resonance (SPR) sensor for uric acid determination. *Sens Actuators B Chem* 2017; 251: 763–772.
121. Prasad BB, Jauhari D, Tiwari MP. Doubly imprinted polymer nanofilm-modified electrochemical sensor for ultra-trace simultaneous analysis of glyphosate and glufosinate. *Biosens Bioelectron* 2014; 59: 81–88.
122. de Middeleer G, Dubruel P, de Saeger S. Characterization of MIP and MIP functionalized surfaces: Current state-of-the-art. *TrAC Trends in Analytical Chemistry* 2016; 76: 71–85.
123. Gründler P. Chemical sensors. *ChemTexts* 2017; 3: 16.
124. Mishra GK, Barfidokht A, Tehrani F, et al. Food Safety Analysis Using Electrochemical Biosensors. *Foods*; 7. Epub ahead of print 2018. DOI: 10.3390/foods7090141.
125. Rubab M, Shahbaz HM, Olaimat AN, et al. Biosensors for rapid and sensitive detection of Staphylococcus aureus in food. *Biosens Bioelectron* 2018; 105: 49–57.
126. Stephen Inbaraj B, Chen BH. Nanomaterial-based sensors for detection of foodborne bacterial pathogens and toxins as well as pork adulteration in meat products. *J Food Drug Anal* 2016; 24: 15–28.
127. Lu L, Gunasekaran S. Dual-channel ITO-microfluidic electrochemical immunosensor for simultaneous detection of two mycotoxins. *Talanta* 2019; 194: 709–716.
128. Reynoso E, Torres E, Bettazzi F, et al. Trends and Perspectives in Immunosensors for Determination of Currently-Used Pesticides: The Case of Glyphosate, Organophosphates, and Neonicotinoids. *Biosensors (Basel)* 2019; 9: 20.
129. Lu X, Li Y, Tao L, et al. Amorphous metal boride as a novel platform for acetylcholinesterase biosensor development and detection of organophosphate pesticides. *Nanotechnology* 2019; 30: 55501.
130. Bagheri N, Khataee A, Hassanzadeh J, et al. Sensitive biosensing of organophosphate pesticides using enzyme mimics of magnetic ZIF-8. *Spectrochim Acta A Mol Biomol Spectrosc* 2019; 209: 118–125.
131. González-Martínez MÁ, Brun EM, Puchades R, et al. Glyphosate immunosensor. Application for water and soil analysis. *Anal Chem* 2005; 77: 4219–4227.
132. Marty JL, Leca B, Noguer T. Biosensors for the detection of pesticides. *Analusis* 1998; 26: 144–148.

133. Bickerstaff GF. Immobilization of Enzymes and Cells. In: Bickerstaff GF (ed) *Immobilization of Enzymes and Cells*. Totowa, NJ: Humana Press, pp. 1–11.
134. Sassolas A, Blum LJ, Leca-Bouvier BD. Immobilization strategies to develop enzymatic biosensors. *Biotechnol Adv* 2012; 30: 489–511.
135. Wang J. Carbon-nanotube based electrochemical biosensors: A review. *Electroanalysis* 2005; 17: 7–14.
136. Besteman K, Lee JO, Wiertz FGM, et al. Enzyme-coated carbon nanotubes as single-molecule biosensors. *Nano Lett* 2003; 3: 727–730.
137. Sotiropoulou S, Chaniotakis NA. Carbon nanotube array-based biosensor. *Anal Bioanal Chem* 2003; 375: 103–105.
138. Balasubramanian K, Burghard M. Biosensors based on carbon nanotubes. *Anal Bioanal Chem* 2006; 385: 452–468.
139. Gerard M, Chaubey A, Malhotra BD. Application of conducting polymers to biosensors. *Biosens Bioelectron* 2002; 17: 345–359.
140. Xia L, Wei Z, Wan M. Conducting polymer nanostructures and their application in biosensors. *J Colloid Interface Sci* 2010; 341: 1–11.
141. Contractor AQ, Sureshkumar TN, Narayanan R, et al. Conducting polymer-based biosensors. *Electrochim Acta* 1994; 39: 1321–1324.
142. Malhotra BD, Chaubey A, Singh SP. Prospects of conducting polymers in biosensors. *Anal Chim Acta* 2006; 578: 59–74.
143. Sekar NK, Gumpu MB, Ramachandra BL, et al. Fabrication of Electrochemical Biosensor with ZnO-PVA Nanocomposite Interface for the Detection of Hydrogen Peroxide. *J Nanosci Nanotechnol* 2018; 18: 4371–4379.
144. Wang Y, Chen X, Zhu J-J. Fabrication of a novel hydrogen peroxide biosensor based on the AuNPs–C@SiO2 composite. *Electrochem commun* 2009; 11: 323–326.
145. Ansari SA, Husain Q. Potential applications of enzymes immobilized on/in nano materials: A review. *Biotechnol Adv* 2012; 30: 512–523.
146. Borgmann S, Schulte A, Neugebauer S, et al. Amperometric Biosensors. In: Alkire RC, Kolb DM, Lipkowski J (eds) *Advances in Electrochemical Science and Engineering*, pp. 1–83.
147. Kalsoom U, Bhatti HN, Asgher M. Characterization of Plant Peroxidases and Their Potential for Degradation of Dyes: a Review. *Appl Biochem Biotechnol* 2015; 176: 1529–1550.
148. Veitch NC. Horseradish peroxidase: a modern view of a classic enzyme. *Phytochemistry* 2004; 65: 249–259.

149. Torrinha Á, Amorim CG, Montenegro MCBSM, et al. Biosensing based on pencil graphite electrodes. *Talanta* 2018; 190: 235–247.
150. Bilal M, Iqbal HMN. Chemical, physical, and biological coordination: An interplay between materials and enzymes as potential platforms for immobilization. *Coord Chem Rev* 2019; 388: 1–23.
151. Kuila T, Bose S, Khanra P, et al. Recent advances in graphene-based biosensors. *Biosens Bioelectron* 2011; 26: 4637–4648.
152. Songa EA, Somerset VS, Waryo T, et al. Amperometric nanobiosensor for quantitative determination of glyphosate and glufosinate residues in corn samples. *Pure and Applied Chemistry* 2009; 81: 123–139.
153. Songa EA, Waryo T, Jahed N, et al. Electrochemical nanobiosensor for glyphosate herbicide and Its metabolite. *Electroanalysis* 2009; 21: 671–674.
154. Songa EA, Arotiba OA, Owino JHO, et al. Electrochemical detection of glyphosate herbicide using horseradish peroxidase immobilized on sulfonated polymer matrix. *Bioelectrochemistry* 2009; 75: 117–123.
155. Cahuantzi-Muñoz SL, González-Fuentes MA, Ortiz-Frade LA, et al. Electrochemical Biosensor for Sensitive Quantification of Glyphosate in Maize Kernels. *Electroanalysis* 2019; 31: 927–935.
156. Kergaravat S v, Fabiano SN, Soutullo AR, et al. Comparison of the performance analytical of two glyphosate electrochemical screening methods based on peroxidase enzyme inhibition. *Microchemical Journal* 2021; 160: 105654.
157. Roman RL, Nagi L, Silva LL, et al. Monocrystalline silicon/polyaniline/horseradish peroxidase enzyme electrode obtained by the electrodeposition method for the electrochemical detection of glyphosate. *Journal of Materials Science: Materials in Electronics* 2020; 31: 9443–9456.
158. Oliveira GC, Moccelini SK, Castilho M, et al. Biosensor based on atemoya peroxidase immobilised on modified nanoclay for glyphosate biomonitoring. *Talanta* 2012; 98: 130–136.
159. Bettazzi F, Natale AR, Torres E, et al. Glyphosate determination by coupling an immuno-magnetic assay with electrochemical sensors. *Sensors (Switzerland)*; 18. Epub ahead of print 2018. DOI: 10.3390/s18092965.
160. Vaghela C, Kulkarni M, Haram S, et al. A novel inhibition based biosensor using urease nanoconjugate entrapped biocomposite membrane for potentiometric glyphosate detection. *Int J Biol Macromol* 2018; 108: 32–40.

161. Sok V, Fragoso A. Amperometric biosensor for glyphosate based on the inhibition of tyrosinase conjugated to carbon nano-onions in a chitosan matrix on a screen-printed electrode. *Microchimica Acta* 2019; 186: 569.
162. Dhamu VN, Prasad S. ElectrochemSENSE: A platform towards field deployable direct on-produce glyphosate detection. *Biosens Bioelectron* 2020; 170: 112609.
163. Congur G. Monitoring of glyphosate-DNA interaction and synergistic genotoxic effect of glyphosate and 2,4-dichlorophenoxyacetic acid using an electrochemical biosensor. *Environmental Pollution* 2021; 271: 116360.
164. Brønstad JO, Friestad HO. Method for determination of glyphosate residues in natural waters based on polarography of the n-nitroso derivative. *Analyst* 1976; 101: 820–824.
165. Martínez Gil P, Laguarda-Miro N, Camino JS, et al. Glyphosate detection with ammonium nitrate and humic acids as potential interfering substances by pulsed voltammetry technique. *Talanta* 2013; 115: 702–705.
166. Laguarda-Miro N, Ferreira FW, García-Breijo E, et al. Glyphosate detection by voltammetric techniques. A comparison between statistical methods and an artificial neural network. *Sens Actuators B Chem* 2012; 171–172: 528–536.
167. Bataller R, Campos I, Laguarda-Miro N, et al. Glyphosate detection by means of a voltammetric electronic tongue and discrimination of potential interferents. *Sensors (Switzerland)* 2012; 12: 17553–17568.
168. Campos I, Alcañiz M, Aguado D, et al. A voltammetric electronic tongue as tool for water quality monitoring in wastewater treatment plants. *Water Res* 2012; 46: 2605–2614.

Chapter 3

Adsorption principles.

Chapter 3 contains information on adsorption as a water purification treatment technology, adsorbent materials and adsorption mechanisms

3.1. Adsorption

The adsorption is a surface phenomenon consisting of the transfer of mass from a fluid phase (liquid or vapor) to a solid surface that is physically or chemically in contact. The substance that is concentrated on the surface or adsorbed is called “adsorbate” and the sorbent phase is called "adsorbent" (1).

According to McCabe (2) the process of adsorption involves the separation of a substance from a fluid phase accompanied by its accumulation or concentration at the surface of of a solid phase.

The contrary process is absorption, which is a process where molecules or atoms of an absorbed phase are mixed almost uniformly in network of atoms of the absorbent phase, constituting a solution. Similarly, is the ion exchange operation that occurs mainly by the diffusion of ions from the dilute electrolyte solution into the interior of a crystalline solid adsorbent (Figure 3.1) (3).

Besides other applications the adsorption process is one of the most efficient methods for removing pollutants from wastewater. In addition, the adsorption process provides an attractive alternative treatment, especially if the adsorbent is inexpensive and readily available (4).

Applications of liquid-phase adsorption include the removal of organic compounds from water or organic solutions, the removal of colored impurities from organic substances, and the removal of various fermentation products from fermenter discharges (5).

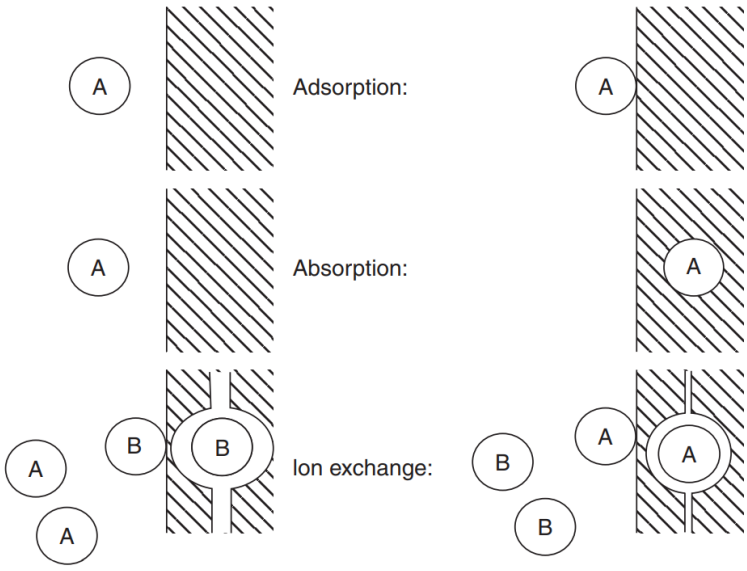


Figure 3.1. Schematic representation of the adsorption, absorption and ion exchange processes (6).

The term sorption includes both adsorption and absorption, and is a general expression of a process in which a component is displaced from one phase and accumulates in another,

especially where the second phase is a solid. The main difference between sorption (adsorption and absorption) and ion exchange is that the equations describing adsorption consider only one chemical species so the distribution of solutes between dissolved and solid responds to a simple linear or nonlinear relationship. The ion exchange equation takes into account all ions competing for exchange sites (7).

Usually, the solute dissolves by adsorption due to the lyophobic (no affinity) character of the solute for a given solvent, due to the solute's high affinity for the solid, or a combination of these two forces. The solubility of the dissolved substance is the most important factor in determining the strength of the first driving force. The more attractive a substance is to a solvent, the less likely it is to move to an interface where it can be adsorbed. Adsorption corresponds to a spontaneous phenomenon accompanied by a decrease in surface free energy (ΔG°), a decrease in the disorder of the system (loss of degrees of freedom of the adsorbed species) and a decrease in entropy (ΔS) (2). The adsorption process is considered a selective process because differences in molecular weight or polarity cause some molecules to be retained more than others (8)

3.2. Types of adsorption.

Three types of adsorption can be distinguished based on the nature of the forces that exist between the solute and the adsorbent. These forces can be electrical, van der Waals or chemical (2).

Physisorption, also known as physical adsorption involves intermolecular attraction that occurs between sites of favorable energy without exchanging electrons and is therefore independent of the electronic properties of the molecules involved. It is characterized by an energy interaction comparable to the heat of vaporization (heat of condensation). Adsorbates are bound to the surface by van der Waals forces, which are relatively weak and can form multilayers with approximately the same heat of adsorption. The heat of adsorption of physical adsorption (a few kcal mol^{-1}) is therefore stable at temperatures below 150 °C. Finally, one of the main characteristics of physisorption is that it is a reversible mechanism (desorption), due to the weak attraction mentioned above.

Chemical adsorption, is commonly known as chemisorption, involves the exchange of electrons between specific surface sites and solute molecules, resulting in chemical bonds. Chemisorption is characterized by energetic interactions between the surface and the adsorbate comparable to chemical bonds (tens of kcal mol^{-1}), and thus stronger and more stable than physisorption at high temperatures. In this way, chemisorption is characterized as an irreversible mechanism.

Electrostatic (ionic) adsorption refers to the process of creating a Coulomb attraction between ions and charged functional groups, known as ion exchange.

3.3. Adsorption mechanism.

The above mentioned adsorption mechanisms vary both with the characteristics of the adsorbent and with the chemical structure of the adsorbate. If we consider metals as adsorbates, the structural complexity of many adsorbents indicates that there are different ways in which a metal can be captured by its surface. Therefore, the mechanisms of adsorption depend in each case on the adsorbate and the sorbent material and in many occasions it is difficult to explain the mechanisms that take place in a given sorption process (2).

3.4. Sorption equilibrium.

One of the most common forms of representing the adsorption equilibrium is through the relationship between the amount adsorbed and the pressure, in the case of gases or vapors, or through the concentration in the liquid phase, in the case of adsorption of liquids, for a given temperature. This relationship is known as the adsorption isotherm for a given adsorbate-adsorbent system and for a fixed temperature.

Adsorption isotherms can be classified into six types (Figure 3.2). This classification was proposed by Brunauer and his collaborators (1938) and is currently recommended by IUPAC (International Union of Pure and Applied Chemistry) (9) .

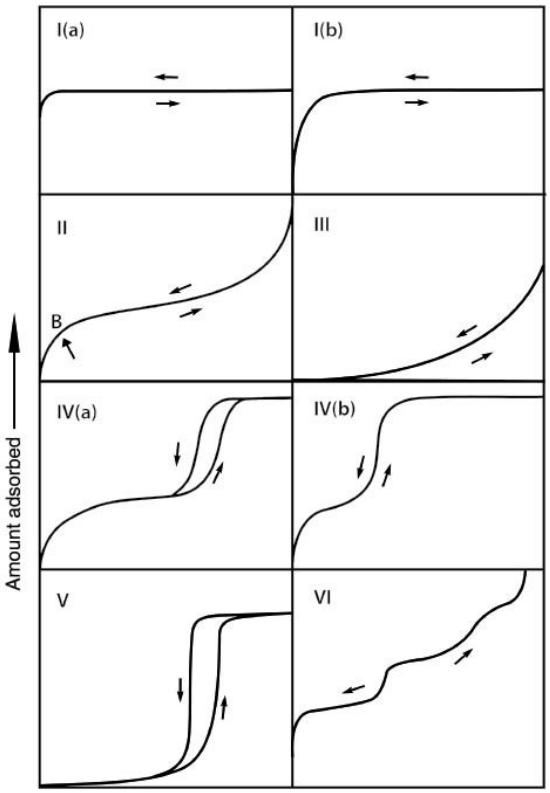


Figure 3.2. Classification of isotherms according to IUPAC (9)

Reversible type I isotherms are given by microporous solids with relatively small external areas such as some activated carbons, molecular sieve zeolites, and certain porous

oxides. The type I isotherm is concave towards the p/p0 axis, and the adsorption capacity is close to the limit. This limited adsorption is determined by accessible micropore volume rather than internal surface area. Extensive adsorption at very low p/p0 is due to enhanced sorbent-adsorption interactions in narrow micropores (those with molecular dimensions), leading to micropore filling. For the adsorption of nitrogen and argon at 77 K and 87 K, type I(a) isotherms are reported for microporous materials with predominantly narrow pores (width < 1 nm); type I(b) isotherms exist for the pore size distribution broader micropores and possibly narrower mesopores (<~2.5 nm) are included in a broad range of materials.

Physisorption of most gases on non-porous or macroporous adsorbents gives reversible type II isotherms. The shape is the result of unrestricted monolayer-multilayer adsorption up to high p/p0. When the knee is sharp, point B—the beginning of the intermediate near-linear portion—usually corresponds to the termination of the single-layer coverage. The gentler curvature indicates a significant overlap of monolayer coverage and multilayer adsorption onset. In general, when p/p0=1, the thickness of the adsorbed multilayer seems to increase infinitely. There is no point B on the type III isotherm, so there is no identifiable monolayer formation; the adsorbent-adsorbate interactions are now relatively weak, and the adsorbed molecules cluster around the most favorable locations on the non-porous or macroporous solid surface. Contrary to the type II isotherm, the amount of adsorption remains limited at the saturation pressure.

Type IV isotherms are given by mesoporous adsorbents such as many oxide gels, industrial adsorbents, and mesoporous molecular sieves. Adsorption behavior in mesopores is governed by adsorbent-adsorption interactions as well as interactions between condensed matter molecules. In this case, an initial monolayer-multilayer adsorption to the mesoporous wall follows the same path as the corresponding part of the Type II isotherm, followed by pore condensation. Pore condensation is a phenomenon in which gas condenses into the liquid phase in pores at a pressure p less than the saturation pressure p0 of the bulk liquid (10,11). A typical feature of a Type IV isotherm is a final saturation plateau of variable length (sometimes reduced to just an inflexion point).

In a Type IVa isotherm, capillary condensation is accompanied by hysteresis. This occurs when the pore size exceeds a certain critical width, which depends on the adsorption system and temperature (e.g., for nitrogen and argon adsorbed in cylindrical pores at 77 K and 87 K, respectively, when the pore width is larger than ~ 4 nm, the hysteresis starts) (10,12). A fully reversible type IVb isotherm is observed for adsorbents with narrower mesopore widths. In principle, type IVb isotherms are also given by conical and cylindrical mesopores closed at the tapered end.

In the low p/p0 regime, the shape of the type V isotherm is very similar to the type III, which can be attributed to the relatively weak adsorbent-adsorbate interactions. At higher p/p0, molecular cluster formation is followed by pore filling. For example, V-shaped isotherms for water adsorption have been observed on hydrophobic microporous and mesoporous adsorbents.

The reversible, stepwise Type VI isotherm represents stratified adsorption on a highly uniform nonporous surface. The step height now represents the capacity of each adsorbed layer, while the sharpness of the step depends on the system and temperature. The best examples of Type VI isotherms are those obtained on graphitized soot with argon or krypton at low temperatures (9).

3.5. Adsorption equilibrium models

Interpretive models of sorption of contaminants in solution are mathematical descriptions of the equilibrium distribution of adsorbates between the liquid and solid phase. In general, the basic adsorption reaction can be described as:

C + Ppl ↔ CPpl

Where Pol represents the adsorbate in solution, C represents the active group in the solid phase and CPpl represents the adsorbate adsorbed by the site (3).

This basic reaction scheme can have different modifications depending on the binding mechanism considered, the different types of active groups and the number of species (13). Generally, pollutant sorption processes have been evaluated using ideal models describing the equilibrium of the process such as Langmuir, (14), Freundlich (15), Toth (16), Sips (17), Khan (18) models, etc.

3.5.1. Langmuir Isotherm

Langmuir in 1918 (14) initially proposed a theory to describe the adsorption of gas molecules on the surface of a metal. Derived from a gas-liquid adsorption hypothesis, the usefulness of this equation for solid-liquid interfaces can be validated through direct comparison to experimental data. The model is classified to be applied to localized monolayer coating adsorption and takes into account the following considerations:

- All sites on the solid have the same activity for adsorption;
- There is no interaction between the adsorbed molecules;
- All adsorption is represented by the same mechanism and each adsorbent complex has the same structure;
- The degree of adsorption is no more than a monomolecular layer on the surface.

Furthermore, according to Langmuir's model, adsorption occurs at specific sites equally available for adsorption. All sites are equivalent and the surface is uniform. A molecule

binds at a site independent of the others, whether they are occupied or not. Theoretically, the adsorbent has an adsorption capacity limited by the adsorbate (19).

The Langmuir model is described by an equation (Equation 3.1), that can be used for example in the adsorption of pesticides, metal ions and other molecules on the surfaces of adsorbent materials.

$$q = \frac{K_L q_m C_e}{1+K_L C_e} \qquad \text{(Equation 3.1)}$$

In this equation, q_m (mmol g^{-1}) represents the amount of adsorbate retained per unit amount of sorbent, C_e (mmol L^{-1}) is the equilibrium concentration of sorbate in the liquid phase and b (L $mmol^{-1}$) is the Langmuir constant related to the affinity between sorbent and sorbate.

One of the characteristics of the Langmuir isotherm is the definition of a dimensionless factor R_L, which indicates the profile of the isotherm and whether the process is favorable or unfavorable (Equation 3.2).

$$R_L = \frac{1}{(1+K_L C_o)} \qquad \text{(Equation 3.2)}$$

In this equation, C_o (mg L^{-1}) is the initial adsorbate concentration. Sorption is considered favorable if $0 < R_L < 1$, unfavorable if $R_L > 1$, linear if $R_L = 1$ and irreversible if $R_L = 0$.

3.5.2. Freundlich Isotherm

The Freundlich isotherm (15) is empirical and corresponds to adsorption on non-uniform sites. The Freundlich adsorption isotherm model describes the reversible, non-ideal adsorption process. Unlike the Langmuir isotherm model, the Freundlich model is not limited to monolayer formation and can therefore be applied to multilayer adsorption (20).

In this case, the heat of adsorption often decreases with increasing surface coverage. The non-uniformity, however, may exist before the different adsorption sites or be caused by repulsive forces between atom and adsorbed molecules. Especially, in the case of binding between the surface and the adsorbate is partially ionic, the repulsions can become large, decreasing the heat of adsorption remarkably at higher coverages (21)

The isotherm derived from the Freundlich model (Equation 3.3) is often described as the classical equation for sorption processes and is widely used, particularly within the low to intermediate concentration range.

$$Qe = K_F C_e^{\,1/n} \qquad \text{(Equation 3.3)}$$

Where Q_e is the amount adsorbed per mass of adsorbent at equilibrium, K_F is the equilibrium constant of the Freundlich equations, C_e is the equilibrium concentration and *n* is the rate of the Freundlich isotherm.

The exponent 1/n is dimensionless and less than 1, representing the intensity with which adsorption occurs. The lower the value of 1/n, the more heterogeneous the surface.

3.5.3. Toth Isotherm

This isotherm model is a modified empirical form of the Langmuir equation, to reduce the error between the experimental value and the predicted value. In general, this isotherm model is used for the description of heterogeneous adsorption systems, satisfying low and high adsorbate concentrations. It is assumed by the correlation of this isotherm model that an asymmetric quasi-Gaussian energy distribution, in which most of the sites have adsorption energy lower than the mean or peak value (22). The nonlinear form of this isotherm model can be expressed as follows (Equation 3.4),

$$Qe = \frac{K_T * C_e}{[a_T + C_e^t]^{\frac{1}{t}}} \qquad \text{(Equation 3.4)}$$

The equation reduces to the Langmuir isotherm equation when t=1.

Thus, (t) is a parameter indicating the heterogeneity of the adsorption system where it is considered heterogeneous when (t) is not equal to unity (23). In addition, the increase in temperature leads to the rapid increase of a_t due to the independent relationship between temperature and parameter t.

3.5.4. Sips Isotherm

The combination of the Langmuir and Freundlich isotherm models resulted in the Sips isotherm model, which was used to predict the heterogeneity of the adsorption system and to circumvent the limitations of the Freundlich model associated with increasing adsorbate concentration. This in turn leads to expression with a limited restriction at high concentrations. The Sips model has the validity to localize adsorption in the absence of adsorbate-adsorbate interactions (24). The Sips equation is given by the following nonlinear expression (Equation 3.5).

$$qe = \frac{K_s * C_e^n}{1 + k_s C_e^n} \qquad \text{(Equation 3.5)}$$

Where Q_e (mg g^{-1}) is the maximum amount of adsorbate adsorbed, C_e (mg L^{-1}) is the concentration of the aqueous phase at equilibrium, Ks (L mg^{-1}) is the Sips constant and *n* is the index of heterogeneity.

The Sips isotherm model does not obey Henry's Law due to reversion to the Freundlich model at low adsorbate concentrations. On the other hand, it predicts the monolayer adsorption properties of the Langmuir model when the adsorbate concentration is high.

3.5.5. Khan isotherm

This isotherm model is a generalized model proposed for the adsorption of adsorbates from pure solutions, in which the Langmuir and Freundlich models are represented. This isotherm model was developed for both single-component and multi-component adsorption systems. The equation of the model is expressed as follows:

$$q_e = \frac{q_s b_k C_e}{(1+b_k C_e)^{a_K)}}$$ (Equation 3.6)

The maximum adsorption value is well determined by a high correlation coefficient, as are the minimum chi-square and overall mean square error (ERRSQ) values. The Khan model degenerates to a Freundlich isotherm for large values of equilibrium concentration. Furthermore, when a_K equals 1, the isotherm model reduces to the Langmuir isotherm system (18).

3.6. Kinetics of the sorption process

The speed of the sorption process and the dynamic behavior of the system are very important factors for process design, performance control and any practical application. A good mathematical model is essential, as it describes the behaviour of all adsorbates retained by a given sorbent.

The kinetics of numerous adsorption processes have been investigated and it has been found that the vast majority of processes fit the pseudo-first order model, while others fit mainly pseudo second-order and intraparticle diffusion models (25).

The application of kinetic models is seen through graphical analysis and evaluation of the data by analysis of the direct correlation coefficient R^2 which must have a value close to 1 for a satisfactory fit of the data for a given kinetic model (26).

3.6.1. Pseudo-First Order Kinetic Equation

The first equation established for a solid/liquid adsorption system was the Lagergren equation (1898) also called the pseudo-first order equation (27). This equation is widely used in the adsorption processes of solutes from a liquid solution and is based on the sorption capacity of the solid.

Lagergren's (1898) model assumes that the variation of solute uptake over time is directly proportional to the difference between the amount adsorbed at equilibrium and the amount adsorbed at any time.

The pseudo-first order equation is established from a differential equation, this being the most commonly used in adsorption processes.

$$\frac{dq_t}{d_t} = K_1(q_e - q_t)$$ (Equation 3.7)

$$\ln(q_e - q_t) = \ln q_e - k_1 t$$ (Equation 3.8)

In both equations, q_t (mg g^{-1}) represents the amount of adsorbate retained per unit mass of sorbent over time, q_e (mg g^{-1}) represents the amount of adsorbate retained per unit mass of sorbent at equilibrium, t (min) is the time and K_1 (min^{-1}) is the pseudo-first order rate constant.

If the experimental data fit to this model, a plot of ln (q_e - q_t) versus t should present a straight line with angular coefficient K_1 and line coefficient ln(q_e). The half-life time for this model is calculated from the following equation:

$$t_{\frac{1}{2}} = \frac{\ln 2}{k_1} \qquad \text{(Equation 3.9)}$$

In many cases, the pseudo-first equation does not fit the entire contact time range, being applicable when it exceeds 20 to 30 minutes from the beginning of the adsorption process. When the Lagergren equation is used it is also necessary to consider that many times q_e is unknown, since the process is extremely slow. In this case, it is necessary to obtain the real adsorption capacity at equilibrium, q_e, by extrapolating the experimental data for infinite time or by estimation and error method.

3.6.2. Pseudo-Second Order Kinetic Equation

The pseudo second-order kinetic model is also based on the adsorption capacity of the solid phase and manifests the behavior of the process throughout the contact time phase. It is described by fitting experimental data according to the following equation.

$$\frac{dq_t}{d_t} = K_2(q_e - q_t) \qquad \text{(Equation 3.10)}$$

$$\frac{t}{q} = \frac{1}{K_2 q_e^2} + \frac{1}{q_e} t \qquad \text{(Equation 3.11)}$$

In addition, to perform the calculation of the initial adsorption velocity it can be done from the following equation:

$$h_1 = k_2 q_e^2 \qquad \text{(Equation 3.12)}$$

In the above equations, k_2 (mg g^{-1} min^{-1}) is the pseudo-second order sorption rate constant. The half-life for this model is calculated as follows:

$$t_{\frac{1}{2}} = \frac{\ln 2}{k_1} \qquad \text{(Equation 3.13)}$$

3.6.3. Bangham Kinetic Model

The Bangham model is used to describe pore diffusion during the sorption process, which is represented by the following equation 3.14.

$$\log\left[\log\left(\frac{C_0}{C_0 - q.m}\right)\right] = \log\left(\frac{k_B.m}{2{,}303.V}\right) + \lambda.\log t \qquad \text{(Equation 3.14)}$$

K_B and λ are the empirical constants of the equation, C_o (mg L^{-1}) is the initial concentration of the adsorbate in solution, V is the volume of the solution (L), m (g) the mass of the adsorbent, and q (mg g^{-1}) the amount of adsorbate retained per unit sorbent.

3.6.4. Avrami Kinetic Model

This model assumes that the reaction is localized at the surface active sites of the solid support and its equation adopts an exponential form represented by Equation 3.15 (28)

$$Qt = Qe[1 - \exp(-K_{AV} t^{n_{AV}})] \qquad \text{Equation 3.15}$$

The specific Avrami adsorption equation evaluates the changes in adsorption mechanisms as a function of contact time (29) (Equation 3.15 and 3.16), where k_{AV} is the Avrami kinetic constant (min^{-1}) and n_{AV} is the Avrami exponent which reflects adsorption mechanism.

To verify this model, it is convenient to plot Q_t as a function of contact time t for the exponential model or Ln (-Ln(1-Q_t)) as a function of Ln (t) for the double logarithmic model and determine the coefficient R^2.

3.6.5. Weber-Morris Kinetic Model

Weber and Morris (1963) derived a model to describe the intraparticle diffusion process (30). This model is presented as follows:

$$q_t = k_{dif} t^{0,5} + C \qquad \text{(Equation 3.15)}$$

Where K_{dif} (mg g^{-1} $min^{-0.5}$) is the kinetic constant of Weber and Morris and C is the constant related to the boundary layer. This factor is added by the authors to represent exactly the possible difference presented in the regression at the origin of the graph.

By plotting q_t vs $t^{0.5}$, one can estimate the parameter k_{dif}. The plot of q_t vs $t^{0.5}$ is a straight line and passes through the origin of the Cartesian plane when intraparticle diffusion is the controlling process. Otherwise, adsorption is controlled by multiple processes.

3.7. Study of the sorption process under dynamic conditions.

In general, experiments performed in systems under static conditions provide important information on the equilibrium characteristics and kinetics of adsorption. However, this type of operation is not economically viable for application on an industrial scale. That is why the data obtained in column systems are considered essential for the design of industrial adsorbers (31).

In fixed-bed column adsorption, the concentrations in the fluid phase and the solid phase vary with time and position in the layer. As the water flows through the column, the contaminant is gradually removed as the wastewater flows through the column (32).

At the beginning of a column's operation, most of the mass transfer takes place near the inlet of the column, where the fluid contacts the adsorbent. Over time, the solid near the inlet is nearly saturated and most of the mass transfer takes place away from the inlet. The

region where most of the concentration change occurs is called the mass transfer zone (MTZ), which separates the virgin zone of the adsorbent from the saturation zone. As the operating time of the column elapses, the mass transfer zone in the bed shifts until it reaches its lower end (31,33).

The analysis of solid layers in columns is based on the development of effluent concentration versus time or versus eluate volume curves, which are a function of sorbent geometry, operating conditions and sorption equilibrium data. The effluent concentration versus time curve is commonly referred to as a penetration curve. This is obtained by introducing a fluid containing the solute with an initial concentration of C_0 through a bed filled with a clean or regenerated adsorbent. As the fluid flow continues, the bed becomes saturated at a given position and a distribution of concentrations within the bed is established as shown in Figure 3.3 (34).

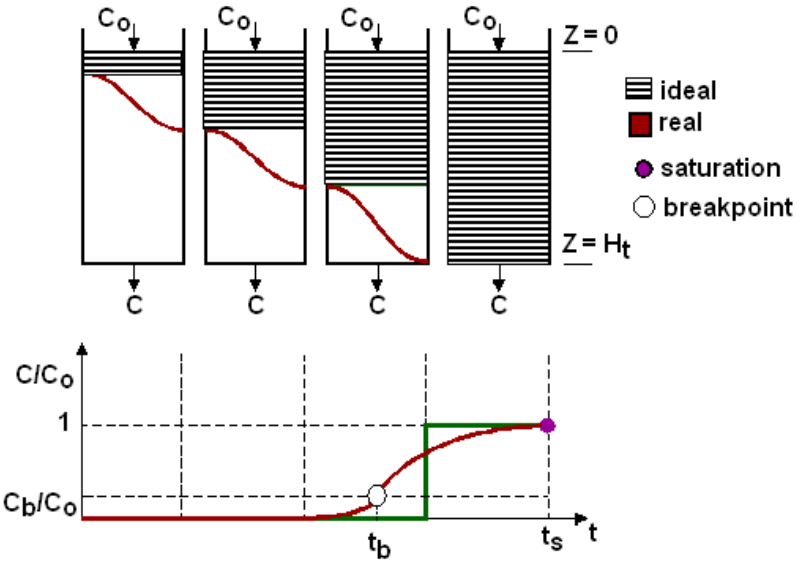


Figure 3.3. Breakthrough curve (34)

At time t_i, the solute appears for the first time in the effluent stream. The time t_b is defined as the time required to reach the change-point concentration (C_b) which corresponds to the maximum concentration admissible in the effluent. The time t_s is the time in which the bed becomes saturated with adsorbate, which requires the bed to regenerate. The period of time from t_i to t_s corresponds to the thickness of the adsorption or mass transfer zone in the bed and is related to the mechanism of the adsorption process. It can be easily observed that the area behind the breakthrough curve represents the amount of adsorbate retained in the column. This corresponds to a point of the equilibrium isotherm.

After the breakthrough point, the column outflow concentration increases rapidly, which characterizes the beginning of system saturation. Finally, when the eluent concentration

does not show significant changes and is approximately equal to the initial concentration feeding the column, the system has reached the saturation point, i.e., there is no longer mass transfer and the concentration of the column feed and effluent are equal and consequently C/C_o is equal to one (34).

3.8. Adsorbents.

3.8.1. Agroindustrial wastes

The study of natural sorbents (biosorbents) is a much discussed topic nowadays due to their great advantages for the economy of implementation costs in pollutant removal processes (35).

Among the different types of natural sorbents is biomass. This is constituted by organic material of plant, animal or microbial origin, including the material of its transformation, natural or artificial. They can be classified as natural (found in nature), produced (cultivated by man to be marketable) and of residual origin (generated as by-products of anthropogenic activity) (36).

The use of agricultural residues as adsorbents is currently receiving great attention due to their abundant availability and low cost due to the relatively high fixed carbon content and the presence of porous structure (37).

One of the most important agricultural wastes is the husks of different fruits and cereals, which can serve as potential adsorbents for the removal of various types of contaminants (38-40). Different types of husks have been investigated so far for wastewater treatment (41-43) and the objective behind their use as adsorbents is that they provide a double advantage to environmental pollution. Firstly, the volume of waste could be partly reduced and, secondly, the adsorbent can treat toxic industrial effluents at a reasonable cost (44).

Agroindustrial by-products have been explored as potential adsorbent materials for the adsorption process, for which notable advantages have been reported, such as the removal of the entire pollutant molecule, high retention efficiency, low cost and ease process implementation, as well as the absence of sludge formation and/or toxic products (45,46).

The adsorption capacity of these agricultural residues depends on multiple factors, such as pH value, dosage, pollutant concentration, particle size, temperature, contact time and agitation speed, i.e. the conditions under which the process is carried out and the nature of the pollutant (47). However, the adsorption capacity of the residue is determined by its particular chemical composition and by the distribution of charges on its surface (48).

3.8.2. Rice husk as adsorbent material

World rice utilization in 2022/23 will amount to 519.0 million tons, about 600,000 tons more than forecast in November 2022, but still 0.6% below the all-time high of 2021/22. It is estimated that between 20-25% of the production represents paddy rice, so it is estimated at approximately 130 million tons (49).

Rice husk is a promising adsorbent material for removing different pollutants because it is a renewable and low-cost resource. The typical chemical composition of rice husk is about 32% cellulose, 20% hemicellulose, 21% lignin and 20% other organic matter, such as proteins and fats (50). At present, much of the rice husk is directly disposed of on the ground or burned, resulting in environmental pollution. However, rice husk has been widely used to adsorb heavy metals (51), phenolic compounds (52), dyes (53), pesticides (54), etc.

As indicated above, waste from this type of product is easy to handle and to acess making it attractive for the decontamination process since contributes for solving directly environmental problems. This is evidenced in the multiple studies that have been developed in this field and with this material (55). However, in terms of adsorbent performance, one of the problems faced by this type of material in its natural state is its low adsorption capacity. This implies the use of large amounts of material, so its application without structural chemical modifications is being strongly discussed. Despite this, there is currently a tendency to use these biomasses to develop new modified materials with better adsorption performance (56).

3.8.3. Metal-organic frameworks as adsorbent material

Organometallic frameworks (MOFs) are strongly adsorbing nanoporous materials that initially consist of two structures: organic (organic ligands) and inorganic (metal cations) structures, each linked by coordinate bonds (Figure 3.4). Metal ions or metal nodes, also known as inorganic secondary bonding units, are used to design organometallic structures with diverse spatial arrangements, which facilitates the discovery of various structures (57).

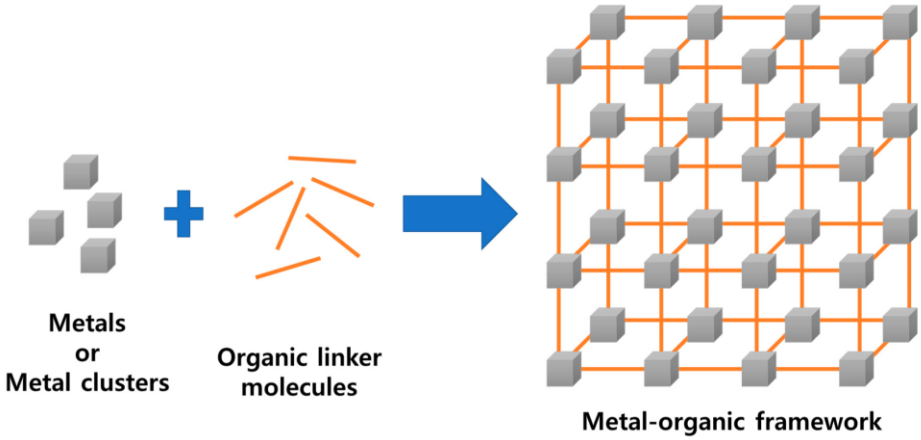


Figure 3.4. Schematic illustration of a metal-organic framework assembled from organic linkers and metal clusters (58)

According to the Cambridge Structural Database, more than 90,000 MOFs have been synthesized worldwide to date (59). In recent decades, these materials have been widely used as adsorbents due to their high surface area and large pore size. MOFs have a wide range of topological structures, so their applications mainly involve gas storage and separation, heavy metal adsorption, dyes, pesticides, drugs, refractory materials, and personal care (60).

Although MOFs are excellent adsorbent materials and, due to their properties and characteristics, can be used to reduce the presence of almost all pollutants, they have some limitations that threaten their future use in a traditional way. The particle size for most MOF series is relatively small compared to other adsorbent materials such as residual biomass, ranging from 0.3 to 1.2 mm depending on need and treatment (61). According to Jia et al.(62), the average pore size of MOF is generally in the range of 0.1~1 nm, the basic unit of MOF is in the range of 1~100 nm, and the MOF particles can be measured between 100~1000 nm and agglomeration of several 10000 nm particles of the same material. These particle sizes are poorly suited for applications where the use of adsorption columns is necessary and where particle size plays an important role in operating conditions from a hydrodynamic point of view. Materials in the form of small crystals or powders are rarely used in fixed beds because they create a pressure drop that can lead to plugging in the column. Thus, technical operational disadvantages become apparent, but also a waste of the enormous potential that these materials may have as unique structures in adsorption columns. On the other hand, another disadvantageous aspect to consider is their production cost despite the high yields of MOF synthesis (typically 90% at laboratory scale) and the large volumes used in any procedure. During the synthesis process, high amounts of organic reagents are applied with a consequent environmental impact, in addition to high

operating costs (63). In this sense, it can be generalized that for adsorption processes in continuous and batch systems, the use of pure MOFs is disadvantageous from a technical and economic point of view.

3.8.4. MOF@biomass hybrids as adsorbent material

As mentioned above, MOFs have some limitations due to their high production costs, and the use of toxic solvents during synthesis (64,65). Finding alternative materials is crucial for MOF-based composites to become more promising adsorbent materials. So far, functionalization of biosorbents with MOFs has been shown to lead to desirable hybrid sorbents, which according to Gurav et al. (66), these materials fulfil several requirements: high surface area and adaptability, low toxicity, easy recycling, economical cost-effectiveness, disposable and synthesis on a commercial scale from readily available starting materials. Therefore, according to the literature, a series of biomass-hybridized MOFs were synthesized as a strategy to provide new adsorbents, enhance selectivity, and facilitate morphological changes to analyze their properties and possibilities and improve their efficiency (67).

According to Rivadeneira-Mendoza et al. (67), the study of hybrids between MOFs and biomass for adsorption processes is new (since 2017). Once used, the new hybrid is mechanically stable after several adsorption cycles (from 5 to 8) and maintains a high level of removal efficiency (between 67% and 98.5%) relative to the initial adsorption. The improved mechanical stability is due to the uptake of biomass, which leads to the formation of a hierarchical mesoporous structure, which enhances the hydrophobicity of the composite, especially after heat treatment of the new hybrid (68). This characteristic represents an important contribution to the commercialization and economic efficiency of industrial adsorption processes.

In general, it can be said that the new MOF@biomass hybrids are highly selective in terms of competition between adsorbates and are considered suitable for the remediation of practical residues when their complexity is justified by the impact of contamination.

3.9. References

1. Kurniawan TA, Chan GYS, Lo WH, Babel S. Physico–chemical treatment techniques for wastewater laden with heavy metals. Chem Eng J. 2006;118(1):83–98.
2. McCabe WL, Smith JC, Harriott P. Unit Operations of Chemical Engineering [Internet]. McGraw-Hill Education (India) Private Limited; 2014. (McGraw-Hill's chemical engineering series).
3. Rodríguez-Díaz JM. Caracterização e Avaliação das Cinzas do Bagaço de Cana-de-Açúcar como Adsorvente na Remoção dos Íons Cd(II), Ni(II) e Zn(II) de Soluções

Aquosas. [Pernambuco]: Universidade Federal de Pernambuco; 2013.

4. Zambrano-Intriago LA, Gorozabel-Mendoza ML, Córdova Mosquera A, Delgado-Demera MH, Duarte MMMB, Rodríguez-Díaz JM. Kinetics, equilibrium, and thermodynamics of the blue 19 dye adsorption process using residual biomass attained from rice cultivation. Biomass Convers Biorefinery. 2020;
5. Geankoplis CJ. Transport Processes and Unit Operations [Internet]. Prentice Hall; 1992.
6. Appelo CAJ, Postma D. Geochemistry, Groundwater and Pollution, Second Edition [Internet]. Taylor & Francis; 2005.
7. Martínez PJ. Operaciones de separacion en ingeniería [Internet]. Pearson Educación; 2004.
8. McKetta JJ. Unit Operations Handbook: Volume 1 (In Two Volumes) [Internet]. CRC Press; 2018.
9. Thommes M, Kaneko K, Neimark A V, Olivier JP, Rodriguez-Reinoso F, Rouquerol J, et al. Physisorption of gases, with special reference to the evaluation of surface area and pore size distribution (IUPAC Technical Report). 2015;87(9–10):1051–69.
10. Thommes M, Cychosz KA. Physical adsorption characterization of nanoporous materials: progress and challenges. Adsorption. 2014;20(2):233–50.
11. Monson PA. Understanding adsorption/desorption hysteresis for fluids in mesoporous materials using simple molecular models and classical density functional theory. Microporous Mesoporous Mater. 2012;160:47–66.
12. Landers J, Gor GY, Neimark A V. Density functional theory methods for characterization of porous materials. Colloids Surfaces A Physicochem Eng Asp. 2013;437:3–32.
13. Volesky B. Biosorption process simulation tools. Hydrometallurgy. 2003;71(1–2):179–90.
14. Langmuir I. THE ADSORPTION OF GASES ON PLANE SURFACES OF GLASS, MICA AND PLATINUM. J Am Chem Soc. 1918;40(9):1361–403.
15. Freundlich HMF. Over the adsorption in solution. J Phys chem. 1906;57(385471):1100–7.
16. Toth J. State equation of the solid-gas interface layers. Acta chim hung. 1971;69:311–28.
17. Sips R. Combined form of Langmuir and Freundlich equations. J Chem Phys. 1948;16(429):490–5.
18. Khan AR, Ataullah R, Al-Haddad A. Equilibrium Adsorption Studies of Some Aromatic Pollutants from Dilute Aqueous Solutions on Activated Carbon at Different

Temperatures. J Colloid Interface Sci. 1997;194(1):154–65.

19. Ernst B, Bodmann J, Dick DP, Dick YP. An Adsorption Isotherm from a Micro-state Model. Adsorption. 2005;10(4):277–86.
20. Adamson AW, Gast AP. Physical Chemistry of Surfaces [Internet]. Wiley; 1997.
21. Gupta VK, Mittal A, Malviya A, Mittal J. Adsorption of carmoisine A from wastewater using waste materials—Bottom ash and deoiled soya. J Colloid Interface Sci. 2009;335(1):24–33.
22. Ho YS, Porter JF, McKay G. Equilibrium Isotherm Studies for the Sorption of Divalent Metal Ions onto Peat: Copper, Nickel and Lead Single Component Systems. Water Air Soil Pollut. 2002;141(1):1–33.
23. Podder MS, Majumder CB. Studies on the removal of As(III) and As(V) through their adsorption onto granular activated carbon/MnFe2O4 composite: isotherm studies and error analysis. Compos Interfaces. 2016;23(4):327–72.
24. Saadi R, Saadi Z, Fazaeli R, Fard NE. Monolayer and multilayer adsorption isotherm models for sorption from aqueous media. Korean J Chem Eng. 2015;32(5):787–99.
25. Rudzinski W, Plazinski W. On the applicability of the pseudo-second order equation to represent the kinetics of adsorption at solid/solution interfaces: a theoretical analysis based on the statistical rate theory. Adsorption. 2009;15(2):181–92.
26. Yang X, Al-Duri B. Kinetic modeling of liquid-phase adsorption of reactive dyes on activated carbon. J Colloid Interface Sci. 2005;287(1):25–34.
27. Lagergren SK. About the theory of so-called adsorption of soluble substances. Sven Vetenskapsakad Handingarl. 1898;24:1–39.
28. George R, Sugunan S. Kinetics of adsorption of lipase onto different mesoporous materials: Evaluation of Avrami model and leaching studies. J Mol Catal B Enzym. 2014;105:26–32.
29. Oladoja NA. A critical review of the applicability of Avrami fractional kinetic equation in adsorption-based water treatment studies. Desalin Water Treat. 2016;57(34):15813–25.
30. Weber Jr WJ, Morris JC. Kinetics of adsorption on carbon from solution. J Sanit Eng Div. 1963;89(2):31–59.
31. Ali I. Water Treatment by Adsorption Columns: Evaluation at Ground Level. Sep Purif Rev. 2014;43(3):175–205.
32. Fernández-Andrade KJ, González-Vargas MC, Rodríguez-Rico IL, Ruiz-Reyes E, Quiroz-Fernández LS, Baquerizo-Crespo RJ, et al. Evaluation of mass transfer in packed column for competitive adsorption of Tartrazine and brilliant blue FCF: A statistical analysis. Results Eng. 2022;14:100449.

33. Xu Z, Cai J guo, Pan B cai. Mathematically modeling fixed-bed adsorption in aqueous systems. J Zhejiang Univ Sci A. 2013;14(3):155–76.
34. Barros MASD, Arroyo PA, Silva EA. General Aspects of Aqueous Sorption Process in Fixed Beds. In: Nakajima H, editor. Rijeka: IntechOpen; 2013. p. Ch. 14.
35. Nayak A, Bhushan B. An overview of the recent trends on the waste valorization techniques for food wastes. J Environ Manage. 2019;233:352–70.
36. Fomina M, Gadd GM. Biosorption: current perspectives on concept, definition and application. Bioresour Technol. 2014;160:3–14.
37. Bhatnagar A, Minocha AK, Sillanpää M. Adsorptive removal of cobalt from aqueous solution by utilizing lemon peel as biosorbent. Biochem Eng J. 2010;48(2):181–6.
38. Hokkanen S, Bhatnagar A, Sillanpää M. A review on modification methods to cellulose-based adsorbents to improve adsorption capacity. Water Res. 2016;91:156–73.
39. Solangi NH, Kumar J, Mazari SA, Ahmed S, Fatima N, Mubarak NM. Development of fruit waste derived bio-adsorbents for wastewater treatment: A review. J Hazard Mater. 2021;416:125848.
40. Yaashikaa PR, Kumar PS, Saravanan A, Vo DVN. Advances in biosorbents for removal of environmental pollutants: A review on pretreatment, removal mechanism and future outlook. J Hazard Mater. 2021;420:126596.
41. Onu CE, Ohale PE, Obiora-Okafo IA, Asadu CO, Okoye CC, Ojukwu EV, et al. Application of Rice Husk-Based Biomaterial in Textile Wastewater Treatment BT - Textile Wastewater Treatment: Sustainable Bio-nano Materials and Macromolecules, Volume 2. In: Muthu SS, Khadir A, editors. Singapore: Springer Nature Singapore; 2022. p. 231–50.
42. Pode R. Potential applications of rice husk ash waste from rice husk biomass power plant. Renew Sustain Energy Rev. 2016;53:1468–85.
43. Varsha M, Senthil Kumar P, Senthil Rathi B. A review on recent trends in the removal of emerging contaminants from aquatic environment using low-cost adsorbents. Chemosphere. 2022;287:132270.
44. Annadurai G, Juang RS, Lee DJ. Use of cellulose-based wastes for adsorption of dyes from aqueous solutions. J Hazard Mater. 2002;92(3):263–74.
45. Crini G. Non-conventional low-cost adsorbents for dye removal: A review. Bioresour Technol. 2006;97(9):1061–85.
46. Gouamid M, Ouahrani MR, Bensaci MB. Adsorption Equilibrium, Kinetics and Thermodynamics of Methylene Blue from Aqueous Solutions using Date Palm Leaves. Energy Procedia. 2013;36:898–907.

47. Vijayakumar G, Tamilarasan R, Dharmendirakumar M. Adsorption, Kinetic, Equilibrium and Thermodynamic studies on the removal of basic dye Rhodamine-B from aqueous solution by the use of natural adsorbent perlite. J Mater Environ Sci. 2012;3(1):157–70.
48. Appel C, Ma LQ, Dean Rhue R, Kennelley E. Point of zero charge determination in soils and minerals via traditional methods and detection of electroacoustic mobility. Geoderma. 2003;113(1):77–93.
49. FAO. Global cereal production and trade forecast to fall to three-year lows [Internet]. 2022.
50. Wan Ngah WS, Hanafiah MAKM. Removal of heavy metal ions from wastewater by chemically modified plant wastes as adsorbents: A review. Bioresour Technol. 2008;99(10):3935–48.
51. Okoro HK, Alao SM, Pandey S, Jimoh I, Basheeru KA, Caliphs Z, et al. Recent potential application of rice husk as an eco-friendly adsorbent for removal of heavy metals. Appl Water Sci. 2022;12(12):259.
52. Shamsollahi Z, Partovinia A. Recent advances on pollutants removal by rice husk as a bio-based adsorbent: A critical review. J Environ Manage. 2019;246:314–23.
53. Chuah TG, Jumasiah A, Azni I, Katayon S, Thomas Choong SY. Rice husk as a potentially low-cost biosorbent for heavy metal and dye removal: an overview. Desalination. 2005;175(3):305–16.
54. Ogura AP, Lima JZ, Marques JP, Massaro Sousa L, Rodrigues VGS, Espíndola ELG. A review of pesticides sorption in biochar from maize, rice, and wheat residues: Current status and challenges for soil application. J Environ Manage. 2021;300:113753.
55. Llanos Páez O, Ríos Navarro A, Jaramillo Páez CA, Rodríguez Herrera LF. La cascarilla de arroz como una alternativa en procesos de descontaminación . Vol. 11, Producción + Limpia . scieloco ; 2016. p. 150–60.
56. Fernández-Andrade KJ, Fernández-Andrade AA, Zambrano-Intriago LÁ, Arteaga-Perez LE, Alejandro-Martin S, Baquerizo-Crespo RJ, et al. Microwave-assisted MOF@biomass layered nanomaterials: Characterization and applications in wastewater treatment. Chemosphere. 2022;137664.
57. Doan H V, Amer Hamzah H, Karikkethu Prabhakaran P, Petrillo C, Ting VP. Hierarchical Metal–Organic Frameworks with Macroporosity: Synthesis, Achievements, and Challenges. Nano-Micro Lett. 2019;11(1):54.
58. Heo DY, Do HH, Ahn SH, Kim SY. Metal-Organic Framework Materials for Perovskite Solar Cells. Polymers (Basel). 2020;12(9).

59. Moghadam PZ, Li A, Liu XW, Bueno-Perez R, Wang SD, Wiggin SB, et al. Targeted classification of metal–organic frameworks in the Cambridge structural database (CSD). Chem Sci. 2020;11(32):8373–87.
60. Duan J, Pan Y, Liu G, Jin W. Metal-organic framework adsorbents and membranes for separation applications. Curr Opin Chem Eng. 2018;20:122–31.
61. Nguyen DTC, Le HTN, Nguyen TT, Nguyen TTT, Liew RK, Bach LG, et al. Engineering conversion of Asteraceae plants into biochars for exploring potential applications: a review. Sci Total Environ. 2021;797:149195.
62. Jia X, Zhang B, Chen C, Fu X, Huang Q. Immobilization of chitosan grafted carboxylic Zr-MOF to porous starch for sulfanilamide adsorption. Carbohydr Polym. 2021;253:117305.
63. Luo H, Cheng F, Huelsenbeck L, Smith N. Comparison between conventional solvothermal and aqueous solution-based production of UiO-66-NH2: Life cycle assessment, techno-economic assessment, and implications for CO2 capture and storage. J Environ Chem Eng. 2021;9(2):105159.
64. Sathishkumar P, Arulkumar M, Palvannan T. Utilization of agro-industrial waste Jatropha curcas pods as an activated carbon for the adsorption of reactive dye Remazol Brilliant Blue R (RBBR). J Clean Prod. 2012;22(1):67–75.
65. Zhu L, Zong L, Wu X, Li M, Wang H, You J, et al. Shapeable fibrous aerogels of metal–organic-frameworks templated with nanocellulose for rapid and large-capacity adsorption. ACS Nano. 2018;12(5):4462–8.
66. Gurav R, Bhatia SK, Choi TR, Choi YK, Kim HJ, Song HS, et al. Adsorptive removal of crude petroleum oil from water using floating pinewood biochar decorated with coconut oil-derived fatty acids. Sci Total Environ. 2021;781:146636.
67. Rivadeneira-Mendoza BF, Estrela Filho OA, Fernández-Andrade KJ, Curbelo F, Fred da Silva F, Luque R, et al. MOF@biomass hybrids: Trends on advanced functional materials for adsorption. Environ Res. 2023;216:114424.
68. Qi L, Jiang H, Lin T, Chang X, Jiang B. Fabrication of MIL-53 (Al) based composites from biomass activated carbon (AC) for efficient p-nitrophenol adsorption from aqueous solution. J Taiwan Inst Chem Eng. 2021;127:220–7.

Chapter 4

Experimental section

This section provides an overview of the analytical techniques, methods, and instrumentation used throughout the research work.

4.1. Overview of Electrochemical Technology

In the study of electrochemical sensors and biosensors, probably the most important and commonly used electrochemical techniques are cyclic voltammetry (CV), differential pulse voltammetry (DPV), and amperometry (AMP). Therefore, these three techniques are mainly applied to characterize electrodes and evaluate the performance of developed biosensors. Other technique such as electrochemical impedance spectroscopy (EIS) are also used.

4.1.1. Cyclic voltammetry

Cyclic voltammetry (CV) is perhaps the most versatile electrochemical technique for the investigation of electroactive molecules. Its versatility and simplicity have led to it being employed in numerous fields of chemistry, including inorganic, organic, and biochemistry. The CV is often the first technique used in the electrochemical investigation of a substance, biological material, or an electrode's surface (1). It is useful to quickly find information about thermodynamics of redox processes and the kinetics of heterogeneous electron transfer. It makes it possible to monitor reaction intermediates, to evaluate the stability of reaction products or adsorption processes, or the adsorption of other substances (2).

CV consists of measuring the current response of a redox active solution to a linearly cycled potential sweep. CV is performed by cycling the potential of a working electrode, and measuring the resulting current. The potential of the working electrode is measured against a reference electrode, such as a saturated calomel electrode (SCE) or a silver/silver chloride (Ag/AgCl) electrode , which maintains a constant potential. The resulting applied potential produces an excitation signal. The excitation signal for CV is a linear potential sweep with a triangular waveform. This triangular potential excitation signal moves the electrode potential between two values, sometimes called a switching potential (1).

Depending on the analysis, partial cycles, complete cycles, or series of cycles can be performed (3). A potentiostat/galvanostat measures the current generated by a redox process, which is obtained in a graph of current versus applied potential (Figure 4.1) (4).

The average of the maximum forward and reverse potentials is usually taken as the official reduction potential of the redox couple. This is the most accurate approximation when the electron transfer process is reversible and the diffusion coefficients of the oxidized and reduced forms are the same. When the reaction is reversible, the separation at the peak potential ΔEp is close to $58/n$ mV (25 °C), where n is the number of electrons participating in the redox reactions (this relationship can be used to estimate n).

Reversible means that the reaction is fast enough to balance the concentrations of the oxidized and reduced forms at the electrode surface. Considering the following reversible

system O + ne ↔ R, the correct equilibrium ratio at a given potential is determined by the Nernst equation (Equation 4.1)

$$E = E^0 - \frac{RT}{nF} ln\left(\left[\frac{R}{O}\right]\right) \qquad \text{(Equation 4.1)}$$

where O is the oxidized form and R is the reduced form of the sme species and ne is the number of electrons required for the reaction when a potential time perturbation is applied to the system (5).

Assume that initially, only the R form exists. Starting with a potential value at which no reactions occur, select a positive sampling potential for the first half of the cycle. When the applied potential approaches the standard reduction potential (E°) characteristic of the redox process, the anodic current begins to increase until it reaches a peak value. After passing through the potential region where the oxidation process takes place, the potential scanning direction is reversed. During the reverse scan, O molecules (generated in the forward scan and accumulated near the electrode surface) were reduced to R and a cathodic peak was observed (Figure 4.1) (4).

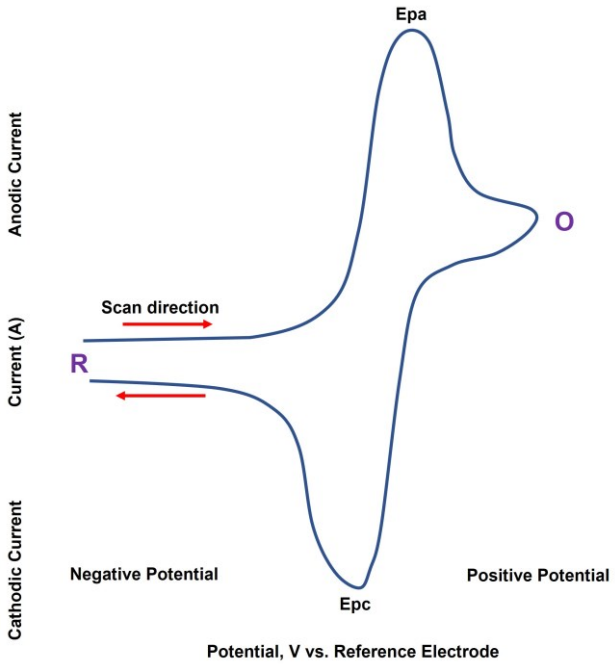


Figure 4.1. Cyclic voltammogram of a electron oxidation-reduction

Another characteristic of reversible systems is that the peak height depends on the square root of the scan rate. At 25°C the peak current is

$$i_p = (2.69\ x\ 10^5) n^{3/2} A D_0^{1/2} v^{1/2} C_0 \qquad \text{(Equation 4.2)}$$

The current can be in amperes when the electrode surface area (A) is in cm^2, the diffusion coefficient (D_o) is in cm^2 sec^{-1}, the sweep rate (v) is in volts sec^{-1}, and C_o is the bulk concentration in moles ml^{-1}.

The peak current of a quasi-reversible system is not proportional to $v^{1/2}$, unless the peaks are so far apart that the system is best described as completely irreversible (5). Therefore, peak separation can be used to calculate the number of electrons transferred and also serve as a criterion for Nernstian behavior (4).

CV is an important technique in the preparation of enzyme biosensors, for example, to assess the correct immobilization of enzymes and verify the possibility of biocatalytic reactions between enzymes and their substrates (analytes).

In addition to cyclic voltammetry, it is normal to use other types of techniques for the characterization of electrochemical sensors. As an example, refer to amperometry, a more sensitive technique.

4.1.2. Amperometry

Amperometry is one of the most widely used techniques in bioanalysis. It involves the application of a constant reducing or oxidizing potential to an indicator (working) electrode and the subsequent measurement of the resulting steady-state current. For some cell and electrode configurations, the decomposition current almost reaches a steady state after a certain time (Figure 4.2). The current becomes effectively time-independent as shown in the following equation 4.3.

$$i = \frac{n\,F\,A\,D^{1/2}\,C_{ox}}{(\pi t)^{1/2}} \qquad \text{(Equation 4.3)}$$

where *i* is the monitored current, *n* is the number of electrons transferred in the redox reaction, *F* is the Faraday constant (96.485 C mol^{-1}), *A* is the area of the electrode, *Co* is the initial concentration of the reducible analyte, *D* is the diffusion coefficient of the reducible analyte in the medium, and *t* is the time elapsed since the potential was applied (6).

This method can be used when the concentration of the substance to be tested is not very low and there are no other reactive substances within the working potential range in the solution.

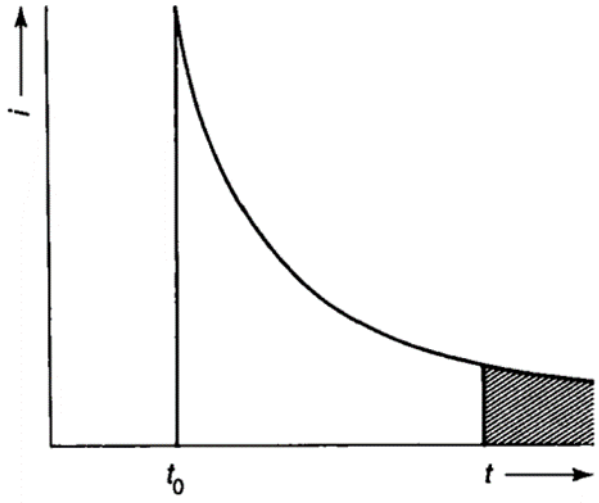


Figure 4.2. The current-time profile associated with a potential step redox process (6).

In the amperometric technique, mass transport under these conditions occurs only by diffusion, so the current-time curve reflects the change in the concentration gradient in the proximity of the electrode surface. Initially, a large amount of current flows, (mostly due to the formation of the electrical double layer (EDL) on the surface of the electrode) which is the result of excess charges of opposite sign accumulating near the interface as required by the change of potential. The maximum current and EDL charging time depend not only on the system and electrode size but also on the parameters of the potentiostat used. When this process is concluded, mainly the faradaic component of the current remains, which in particular will produce changes in surface concentrations (7). This implies a gradual expansion of the diffusion layer associated with the depletion of the reagent, and thus the decrease of the slope of the concentration profile as time progresses (4).

4.1.3. Differential Pulse Voltammetry (DPV)

This technique scans the potential with a series of pulses with a small fixed amplitude (10-100 mV) and is superimposed on a slowly changing base potential (8). This technique resembles normal pulse voltammetry, but with two important differences: the base potential is increased between pulses, these increases being equal, and the current is measured immediately before and at the end of the pulse, to record the difference between the two currents.

As DPV is a differential technique, the response is similar to the first derivative of a differential voltammogram, i.e., a peak. The peak potential, Ep, can be approximately identified with $E_{1/2}$. With increasing irreversibility Ep moves way from $E_{1/2}$ (reversible system), while the peak length increases and its height decreases. The degree of

reversibility of an electrode reaction is similar to that in NPV, because the time scale is the same.

The quantitative treatment for reversible systems is applied with the following Equation 4.4.

$$E_{max} = E_{1/2} \pm \frac{\Delta E}{2} \qquad \text{(Equation 4.4)}$$

where ΔE is the pulse amplitude. The peak current is

$$|(\delta i)_{max}| = \frac{nFAD_o^{1/2}C_\infty}{\pi^{1/2}(t-\tau')^{1/2}}\left(\frac{1-\sigma}{1+\sigma}\right) \qquad \text{(Equation 4.5)}$$

σ is determined by

$$\sigma = exp\left(\frac{nF}{RT}\frac{\Delta E}{2}\right) \qquad \text{(Equation 4.6)}$$

the term (1 - σ)/(1 + σ) describes the effect of ΔE on (δi)max. This term can increase proportionally to |ΔE|, but the use of larger |ΔE| values (near 100 mV is not feasible) results in the peak for half-height $W_{1/2}$ also increasing, and thus losing resolution. In the limit when ΔE → 0

$$W_{1/2} = 3{,}52RT/nF \qquad \text{(Equation 4.7)}$$

4.1.4. Electrochemical impedance spectroscopy

Electrochemical impedance spectroscopy, EIS, is a common method of studying the effects of impedances (i.e. impediments that limit the flow of charges) in electrochemical systems. It's more common to discuss electrode capacitance and heterogeneous charge transfer rates. In alternate-current (AC) systems, the potential and current are both altered in complex ways over time. To relate them, Ohm's law resistance (R) is replaced by impedance (Z), a form of resistance to electron flow that changes with frequency (Equation 4.8).

$$E(t)=I(t)Z \qquad \text{(Equation 4.8)}$$

The potential E is expressed as Volts, the current I is measured in Amperes, and the impedance Z is measured in Ohms. According to the electronic theory, resistors convert the electric energy that is available to drive electric charges into heat. The result is a decreased number of charges that flow across the circuit, and its magnitude is measured as the resistance to electron flow. In turn, capacitors and inductors can store energy in the form of electrical and magnetic fields, respectively. This field's buildup causes typical temporary alterations in the flow of charges that are easily observed in AC conditions as capacitive or inductive impedances. Similarly, the second layer formed at the electrode's surface, the

electrode's kinetics and diffusion processes all affect the flow of charges in an electrochemical cell. EIS measurements are accomplished by applying small AC voltages or currents at different frequencies that are pre-determined. The impedance is then calculated at each frequency value (Figure 4.3) (9).

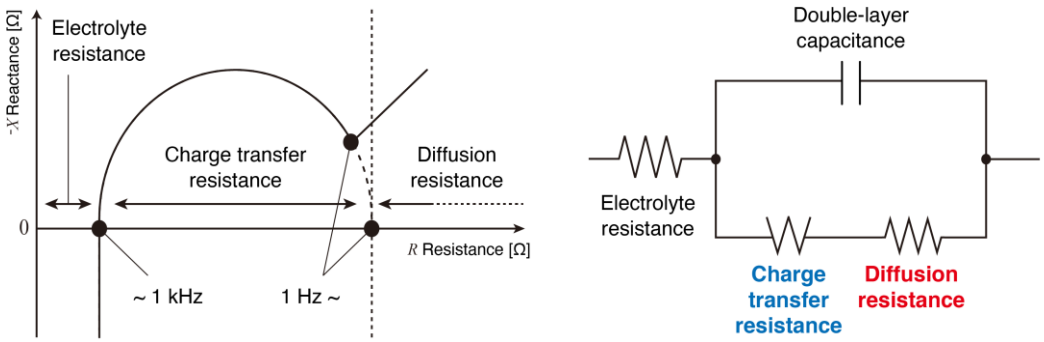


Figure 4.3. Examples of Nyquist plots and equivalent circuit models (10)

Recently, this technique has been employed to understand the consequences of electron transfer from electrodes that have different layers of conductive material, bioentities and biofilms (11).

4.2. Instrumentation

4.2.1. Apparatus for electrochemical determinations

All voltammetric and amperometric measurements were performed with a potentiostat/galvanostat Metrohm, model Autolab PGSTAT10, controlled by GPES v3.9 software (Herisau, Switzerland). The equipment was connected to a Penthium II computer with a Windows 98 operating system (Figure 4.4).



Figure 4.4. Electrochemical workstation composed by the potentiostat Autolab PGSTAT10, computer and electrochemical cell.

For EIS measurements a potentiostat/galvanostat Metrohm, model Autolab FRA32M was used (Figure 4.5). The equipment was controlled by NOVA software from the same brand.

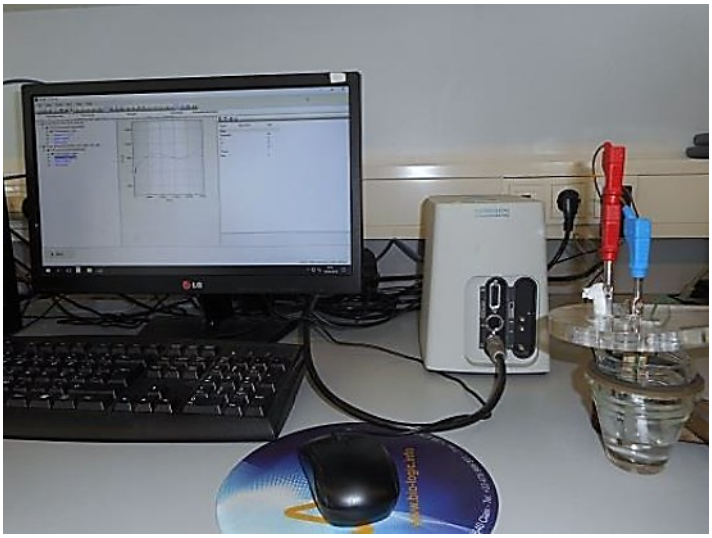


Figure 4.5. Impedance workstation composed by potentiostat with impedance module (Autolab FRA32M), computer and electrochemical cell.

4.2.2. Electrodes

The characteristics of the developed biosensor were evaluated using the usual three-electrode configuration in a conventional electrochemical cell. For this purpose, an Ag/AgCl (KCl, 3M) electrode ref. 6.0727.000 Metrohm (Figure 4.6a) was used as reference electrode, and a platinum rod (Figure 4.6b) as counter electrode.

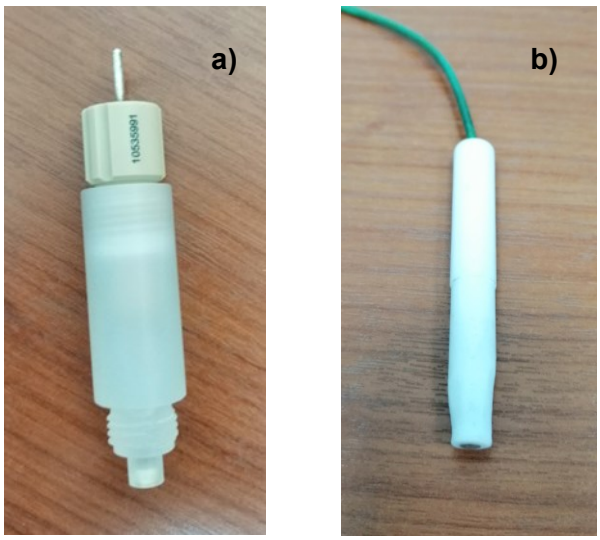


Figure 4.6. a) Ag/AgCl reference electrode, and b) platinum counter electrode

As working electrodes, pencil graphite electrodes (PGEs) represented in Figure 4.7 were used for biosensor studies. Pencil leads of 2 mm diameter (type HB, 4B and 4H) were

placed in contact with the inner copper wire of a shielded coaxial cable and insulated with a flexible polymer sleeve (Tygon) so that only the tip of the graphite lead was exposed. The PGEs were then polished with sandpaper (P1200) and finally washed with distilled water.



Figure 4.7. PGE working electrode used in the development of the biosensor. Inside: 25 cent coin as size reference

4.3. Other equipment

4.3.1. UV-VIS spectrophotometer

In the adsorption studies, measurements of glyphosate were carried out and the values compared with the results obtained electrochemically. For this purpose, Thermo Scientific UV-VIS Spectrophotometer, model Evolution 60-S (Figure 4.8), operated by VisionLite software was used .



Figure 4.8. UV-VIS Spectrophotometer, Thermo Scientific, Evolution 60-S.

4.3.2. Microwave system for synthesis

The hybrid adsorbent material Mil-53(Al)@RH was synthesized with the assistance of microwave radiation as a new alternative to conventional synthesis methods. For this purpose, a microwave system of the CEM brand, model Mars 6, with Teflon vessels was used (Figure 4.9).



Figure 4.9. Microwave system of the CEM brand, model Mars 6.

4.3.3. Equipment employed in adsorption studies

All adsorption tests in batch system were carried out using a shaker with cooling/heating system, Eppendorf, model New Brunswick Excella E24/E24R (Figure 4.10).

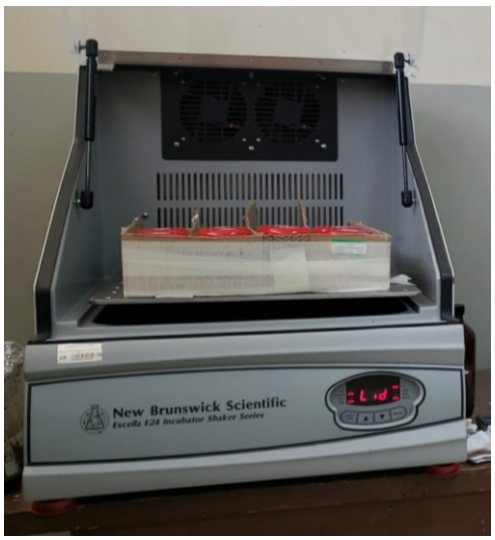


Figure 4.10. Shaker system Eppendorf New Brunswick Excella E24/E24R

For column adsorption studies (Figure 4.11), a 5 mm diameter × 30 mm height laboratory polypropylene column, packed with 0.2 g of Mil-53(Al)@RH was used. A Masterflex L/S 7535-04 multichannel peristaltic multichannel pump was employed to supply the continuous fluid. Finally, a Gilson FC203B fraction collector was used to take the samples at the column outlet.



Figure 4.11. a) Packed column of Mil-53(Al)@RH, b) Column adsorption system, including peristaltic pump, packed column, and fraction collector.

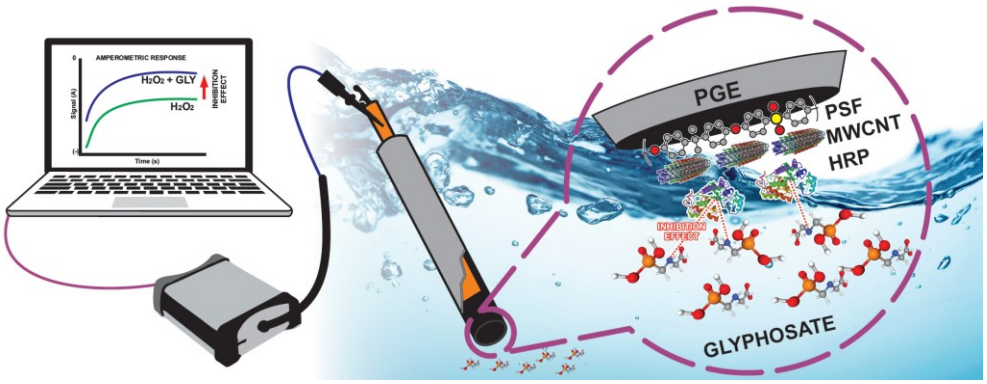
4.4. References

1. Kissinger PT, Heineman WR. Cyclic voltammetry. J Chem Educ. 1983;60(9):702.
2. Wang J. Analytical Electrochemistry [Internet]. Wiley; 2004.
3. Labib M, Sargent EH, Kelley SO. Electrochemical Methods for the Analysis of Clinically Relevant Biomolecules. Chem Rev. 2016;116(16):9001–90.
4. Hoyos-Arbelaez J, Vazquez M, Contreras-Calderon J. Electrochemical methods as a tool for determining the antioxidant capacity of food and beverages: A review. Food Chem. 2017;221:1371–81.
5. Mabbott GA. An introduction to cyclic voltammetry. J Chem Educ. 1983;60(9):697.
6. Eggins BR. Chemical Sensors and Biosensors [Internet]. Wiley; 2002.
7. Bagotsky VS. Fundamentals of Electrochemistry [Internet]. Wiley; 2005.
8. Brett CMA, Brett AMO. Electrochemistry: Principles, Methods, and Applications [Internet]. Oxford University Press; 1993.
9. Bard AJ, Faulkner LR, White HS. Electrochemical Methods: Fundamentals and Applications [Internet]. Wiley; 2022.
10. HIOKI. Nyquist Plot for Impedance Measurement of Lithium-ion Batteries [Internet].

11. Lvovich VF. Impedance Spectroscopy: Applications to Electrochemical and Dielectric Phenomena [Internet]. Wiley; 2012

Chapter 5

Development of an inexpensive and rapidly preparable enzymatic pencil graphite biosensor for monitoring of glyphosate in waters.



Chapter 5 describes the development of a low-cost amperometric enzymatic biosensor for the indirect detection of glyphosate[2]

[2] This is a partial translation of the article *Zambrano-Intriago LA, Amorim CG, Araújo AN, Gritsok D, Rodríguez-Díaz JM, Montenegro MCBSM. Development of an inexpensive and rapidly preparable enzymatic pencil graphite biosensor for monitoring of glyphosate in waters. Sci Total Environ. 2023;855:158865.*
Copyright 2023, with permission from Elsevier

5.1. Introduction

Glyphosate (GLY), the N-(phosphonomethyl) glycine, is a broad-spectrum, non-selective, systemic herbicide for weed control (1). It acts as an inhibitor of essential aromatic amino acid biosynthesis in the shikimic acid pathway (phenylalanine, tyrosine, and tryptophan), with impairment in protein synthesis which results in plant death (2). Since its commercial inception in 1974, GLY became the most used herbicide worldwide, as a component of more than 750 agricultural, forestry, urban and domestic application products (3). Owing to high demand, with a particular focus on transgenic crops, an exceeding 6.1 billion kg GLY had been produced in the last decade (4,5). The World Health Organization (WHO) also contributed to a general acceptance by considering it harmless to humans (6). Nonetheless, recent warnings on the potential carcinogenicity of GLY were issued by the International Agency for Research on Cancer (IARC) (7). GLY in trace amounts was found in cereals and food (8), vegetables and fruits (9), in the environment (10), and even in human and animal fluids (11,12). Different studies point out a positive correlation between exposure to GLY and epithelial diseases (13), cardiocirculatory and muscular disorders (14,15), neural disturbance (15), neoplasia, and teratogenic effects (16–20). In accordance, residues on any food or feed item are safe for consumers only if the amounts comply with the established tolerances. Hence, maximum tolerable levels of 700 μg L^{-1} and 0.1 μg L^{-1} GLY were set for potable waters, respectively by the US and by the EU authorities (21,22).

The determination of GLY residues in different matrices has been addressed with the use of sensitive approaches based on chromatography, spectroscopy, capillary electrophoresis, and enzyme-linked immunosorbent assay (ELISA) (23). The procedures yield reliable results, but in general with the utilization of sophisticated benchtop instrumentation and expensive reagent kits. Proposals that make use of electrochemical methods for pesticide determination otherwise evidence significant gains in terms of equipment expenditure, ease of operation and transport, and simpler determination procedures (24). One of the important advantages of this detection process is versatility in modifying the working electrode, to carry out selective and sensitive detection of several compounds, even those that are not electroactive such as GLY (25–27). Electrochemical sensors have been thus developed based on nanoparticles, metal-organic frameworks (MOFs), molecular imprinting polymers (MIPs), and biological recognition molecules (enzymes and antibodies) as modifying materials (28). In turn, the quality of immobilization of these materials is of utmost importance towards analytical response since it conditions the final operating characteristics of the electrochemical sensor, especially its sensitivity, reproducibility, and shelf life.

Widely used in membrane technology, polysulfone (PSF) is a polymer whose thermal, chemical, and mechanical resistance favors the incorporation of different molecules in

particular those of biological origin, and allows simple morphology adjustments to end-use (29). PSF is readily soluble in solvents such as dimethylformamide (30) or 1-methyl-2-pyrrolidone (NMP) (31) which is essential for membrane preparation through the phase inversion technique. Membranes prepared with this polymer are thus prepared with bio-elements like horseradish peroxidase (32), tyrosinase (33), and anti-rabbit IgG peroxidase-conjugated (34) or only modified with nanomaterials (such as carbon-based, and metal nanoparticles) as described to coat glassy carbon rods or screen-printed electrodes (33,35). Besides selective detection, PSF membranes overturned fouling problems due to the adhesion of the analyte or intermediate products formed in the course of the electrochemical reaction on the carbon-based electrodes. Based on these advantages, a novel enzymatic biosensor for the detection of GLY is described and subsequently reported. A low-cost pencil graphite electrode with an overlaid membrane composed of PSF modified with multi-walled carbon nanotubes and horseradish peroxidase was accomplished to achieve good operational characteristics for GLY detection in real samples. Pencil graphite electrodes (PGE) have been used in electrochemical applications, because of their electrical properties, good stability, lower toxicity, easy disability, reproducibility, and uniform quality when compared to other conventional carbonaceous electrodes (e.g. glassy carbon electrodes), thus making them valuable analytical tools (36). The proposed strategy enables a procedure suited for routine analysis of surface and tap water since it's easy to implement, environmentally clean, and has a low inherent cost.

5.2. Materials and methods

5.2.1. Materials and reagents

Analytical grade chemicals without any additional purification and ultrapure water (resistivity = 18.2 MΩcm) obtained from Brandstead EasyPure II equipment (Waltham, US) were used for solution preparation.

Horseradish peroxidase (HRP, 141.9 U mg^{-1}), glyphosate (GLY), potassium hexacyanoferrate (III), hydroquinone (HQ), potassium phosphate dibasic, multi-walled carbon nanotube (MWCNT, carboxylic acid functionalized), 1-methyl-2-pyrrolidone (NMP), polysulfone (PSF) in pellets (Mw ~ 35,000), polyvinylpyrrolidone (PVP) K30, dimethoate, methomyl, and mesosulfuron-methyl were obtained from Sigma-Aldrich. Hydrogen peroxide (30% v/v), and ascorbic acid were purchased from Fisher Scientific. Potassium dihydrogen phosphate was purchased from Applichem. Potassium hexacyanoferrate (II) trihydrate, potassium chloride, sodium chloride, glucose monohydrate, and sodium bicarbonate were obtained from Merck. Pencil mines of the HB type with 2 mm diameter were purchased from BIC (Clichy, France). Copper coaxial shielded cable and flexible polymer sleeve (Tygon) were purchased in local stores of electronic materials.

5.2.2. Instrumentation

All electrochemical experiments were performed with a Metrohm potentiostat, model Autolab PGSTAT10, controlled by GPES v3.9 software (Herisau, Switzerland). All experiments were conducted in a conventional three-electrode cell composed of the biosensor as the working electrode, Ag/AgCl (KCl, 3 mol L^{-1}) as the reference electrode (Metrohm, Ref. 6.0727.000), and a platinum wire as the auxiliary electrode. Electrochemical impedance spectroscopy (EIS) experiments were performed with an Autolab PGSTAT204, model FRA32M, controlled by NOVA v1.10.1.9 software, all from the same brand.

Fourier transform infrared (FTIR) spectra were obtained using a PerkinElmer FTIR equipment, model Spectrum BX (Waltham, US), equipped with a DTGS detector and a PIKE Technologies Gladi ATR accessory.

The Scanning Electron Microscopy/Energy Dispersive X-Ray Spectroscopy (SEM-EDS) analysis was performed in a High resolution (Schottky) Environmental Scanning Electron Microscope with X-Ray Microanalysis and Electron Backscattered Diffraction analysis: Quanta 400 FEG ESEM/EDAX Genesis X4M.

5.2.3. Working electrode development

For electrode construction, steps shown in Figure 5.1 were followed. First, the electrical contact between an inner copper wire of a 10 cm coaxial shielded cable piece and the graphite pencil mine rod (HB 2 mm, 1 cm length) was promoted by heat inside of a thermo-retractable insulating sleeve. Then, a transversal cut near the distal ending exposed a pristine PGE surface which was further polished mechanically using sandpaper (P1200) and washed with distilled water. About 5 µL of 1-methyl-2-pyrrolidone solution containing 5% (w/w) PSF and 0.5% (w/w) MWCNT was dripped upon the PGE surface that was immediately immersed in a coagulation bath (1 mL) consisting of HRP (100 U mL^{-1}) in buffer solution (pH= 6, 0.1 mol L^{-1} PBS) for 5 min to achieve the phase inversion process. The composition of the recognition membrane was determined after execution of a 5^2 factorial design. This allowed the entrapment of the HRP enzyme and the MWCNTs in/on PSF polymeric membrane. Finally, the electrode, now designated as HRP/PSF/MWCNT/PGE biosensor, was washed thoroughly, with distilled water and kept soaked in 0.1 mol L^{-1} PBS (pH 6) at 4°C between usages.

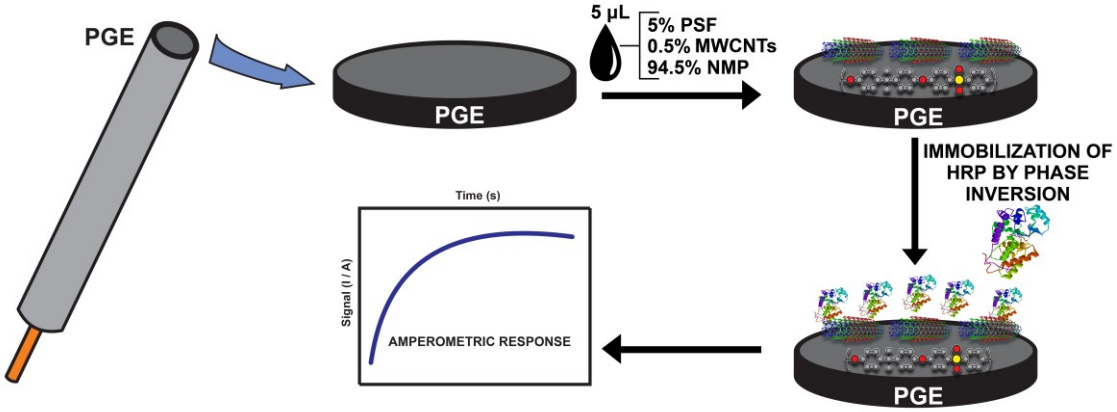


Figure 5.1. Schematic representation of the different construction phases of the HRP/PSF/MWCNT/PGE biosensor.

5.2.4. Electroanalytical measurements

The electrochemical characterization of the biosensor using the $Fe(CN)_6^{3-/4-}$ probe was investigated by cyclic voltammetry (CV) in the potential range of -0.4 to +0.8 V (vs. Ag/AgCl) with a scan rate of 10 mV s^{-1} in 5 mmol L^{-1} of the probe in 0.1 mol L^{-1} KCl solution (solution resistance, R_{sol} = 180 Ω). The electrocatalytic activity of the HRP enzyme was also evaluated using the same electrochemical method for different concentrations of the H_2O_2 substrate and 1.8 mol L^{-1} HQ redox mediator, when PBS (pH 6 at 0.1 mol L^{-1}) is used in the potential range from -0.2 to +0.6 V (vs. Ag/AgCl) at a scan rate of 10 mV s^{-1}.

Amperometric measurements (AMP) with HRP/PSF/MWCNT/PGE biosensor were carried out in 0.1 mol L^{-1} KCl, PBS buffer solution (0.01 mol L^{-1}, pH = 6), 0.5 mmol L^{-1} HQ, under continuous stirring at 200 rpm, and with cell potential poised at -0.05 V vs Ag/AgCl. After current stabilization (about 150 s), ten substrate solution replicates corresponding to 0.05 mL of 10 mmol L^{-1} of H_2O_2, were added to assess the linear range of the analytical response, sensitivity, and the catalytic Michaelis-Menten constant. The determinations of GLY were performed in a volume of electrolyte solution with 10 mL consisting of 0.075 mmol L^{-1} H_2O_2, 0.5 mmol L^{-1} HQ, 0.1 mol L^{-1} KCl in PBS buffer solution (0.01 mol L^{-1}, pH = 6). The initial I_0 current value corresponding to native enzyme activity was registered, after which the biosensor was exposed to different concentrations of GLY solutions for 5 min. The peak current I_1 was recorded for each concentration of the herbicide and transformed into a percentage of inhibition value (%IR) calculated according to Equation 5.1:

$$\%IR = \frac{(I_0 - I_1)}{I_0} x100 \qquad \text{(Equation 5.1)}$$

The effect of interfering compounds was evaluated in the same way but in the presence of 1 mg L^{-1} of GLY.

The determination in real samples was carried out on river water samples from an agricultural zone (collected in Rocafuerte, Ecuador; coordinates -0.875681, -80.494858) and tap water (collected in the laboratory). The samples were filtered through 0.22 µm membranes (nylon) to remove solid particles. The ionic strength and pH were adjusted to achieve the same previously described conditions (PBS (pH 6) 0.01 mol L^{-1} and 0.1 mol L^{-1} KCl). All raw results of this study are available at Mendeley Data (https://doi.org/10.17632/9ccvdmjrm5.2).

5.3. Results and discussion

5.3.1. Electrochemical characterization of the biosensor

The initial studies of this work considered for the biosensor configuration the use of a polymeric membrane on the electroactive surface of PGE. Besides keeping the sensor components immobilized, the use of the membrane was considered to regulate the entry and diffusion kinetics of the analyte while keeping away possible interfering species (37). In this context, to address the last aspect of pesticide detection, some authors alternatively considered the doping of carbon-based electrodes with polymeric materials and carbon nanomaterials (38–40). The PSF membrane was easily prepared in one single step, i.e., by phase inversion in water via immersion precipitation. It acts as a physical barrier to the diffusion of molecules and electroactive ions. By adding a pore-former compound like PVP in the initial formulation it is further possible to widen the intended properties of membranes regarding pore size and abundance of finger-like pores or/and microvoids (41).

Membranes with different compositions were prepared. For that a 5^2 factorial design for the main component of the membrane PSF and the pore-forming PVP has been established. The levels for each variable were respectively, PSF: 1, 5, 10, 15, and 20% (w/w); PVP: 0, 5, 10, 15, and 20% (w/w) in the organic solvent (NMP), in a total of 25 different implemented sensors (Table S1). Fixed amounts of 0.5% (w/w) MWCNTs and 100 U mL^{-1} HRP of enzyme concentration were settled.

The electrochemical study of membranes started with the use of $Fe(CN)_6^{3-/4-}$ probe as electroactive mediator. Detachment of membranes during immersion in the electrolyte solution for electroanalysis and reduced mechanical resistance were promptly noticed for higher PVP concentrations in the initial formulation. The CV results (Table S2 and Figure S1) in the potential range of -0.4 to +0.8 V (vs. Ag/AgCl) and at the scan rate of 10 mV s^{-1} showed that the lower PSF concentration used corresponded to the highest intensity of the anodic/cathodic peaks, as noticed from results obtained for sensors 21, 1, 24 and 3. The PSF content in these sensors decreases in the described order (20, 15, 10, and 5%). The highest anodic/cathodic peaks intensities ($i_{p,a}$ $7.52x10^{-5}$; $i_{p,c}$ $-7.45x10^{-5}$ A) and lowest peak-to-peak separation (ΔEp = 0.13 V) were indicative of less sluggish kinetics in sensor 3. The

low dielectric constant of PSF (ε=3.1) (42) explains this inverse dependence once it favors low ion mobility and concentration within the membrane. In addition, sensor 3 showed excellent mechanical strength, confirmed by the finger rubbing test, indicating a strong adhesion of the membrane to the PGE surface. In the presence of the PVP pore-forming additive, a decrease in peak intensity (Table S2) and a poor resolution of voltammograms were observed (data not shown), due to its low conductive property once its dielectric constant ε is 7.7 (43), therefore, the use of PVP was discarded in the following biosensor membrane preparations.

Carbon nanotubes have attracted attention from various technology and engineering applications due to their unique mechanical and electronic properties combined with their chemical stability (44). Particularly multi-walled carbon nanotubes (MWCNTs) have been used in electrochemical biosensors for pesticide detection (45). The basic configuration consists of sp^2 carbon units oriented as multiple concentric tubes of rolled-up graphene (single-walled nanotubes inside each other). MWCNTs exhibit remarkable active surface area (about 1600 $m^2.g^{-1}$), chemical inertness, high physical resistance, and exceptional electrical conductivity (current densities up to 109 $A.cm^{-2}$) (46,47). The optimal amount of MWCNTs in the implemented biosensor membrane was 0.5% (w/w) (Figure S2). Higher amounts (1% and 1.5%(w/w)) conferred high viscosity to the solution that is deposited on the PGE surface and irreproducible analytical response as well.

Pencil mines are extruded mixtures of graphite and clay that vary the percentages of each component (36). Since the electrical properties of electrodes such as conductivity are largely dependent on the carbonaceous content, the study of the influence of the type of pencil mine on the electrochemical response was also studied. For this purpose, PGEs were constructed with 4B, 4H, and HB mines (BIC; Clichy, France) with 2 mm diameter: the first being a softer mine with higher graphite content; 4H a harder thread with higher binder content; and HB a mid-scale term that typically contains about (w/w) 68% graphite, 26% clay and 5% wax (48). Thus, the surface of the PGE electrode was modified with the optimized membrane containing 5% (w/w) PSF and 0.5% (w/w) MWCNTs. Under these conditions, higher voltammetric peaks were obtained for HB PGEs concerning the 4B and 4H varieties, although without a clear trend between the latter two (Figure S3).

The lower peak separation ΔE_p obtained for HB also denoted a higher heterogeneous electron transfer rate during the redox reaction. These differences in electrochemical properties are related to the extent of the carbonaceous component with carbon-carbon bonds in the sp^2 configuration and variations in size and orientation of graphitic inter-and intraplate microcrystallites (36). The E_{pa} and E_{pc} values shifted slightly towards the positive and negative direction of the potential throughout the sweep rate increasing from 3 to 140

mV s^{-1} (Figure 5.2a), while I_{pa} and I_{pc} increased linearly (Figure 5.2b). The probe electrochemistry was not hindered by the PSF-modified active surface of the electrode since this response trend evidences a diffusion-controlled response, according to the Randles-Sevcik model.

EIS has been widely used in the development of PGE-based sensors (49,50). EIS studies aim a comparison between PSF/MWCNT/PGE and HRP/PSF/MWCNT/PGE electrode's response with the unmodified PGE at the open circuit potential of 0.15 V (vs Ag/AgCl) in deaerated equimolar 5 mmol L^{-1} $Fe(CN)_6^{3-/4-}$ in 0.1 mol L^{-1} KCl solution (R_{sol} = 180Ω), typically revealed by the Nyquist plots (Figure 5.2c).

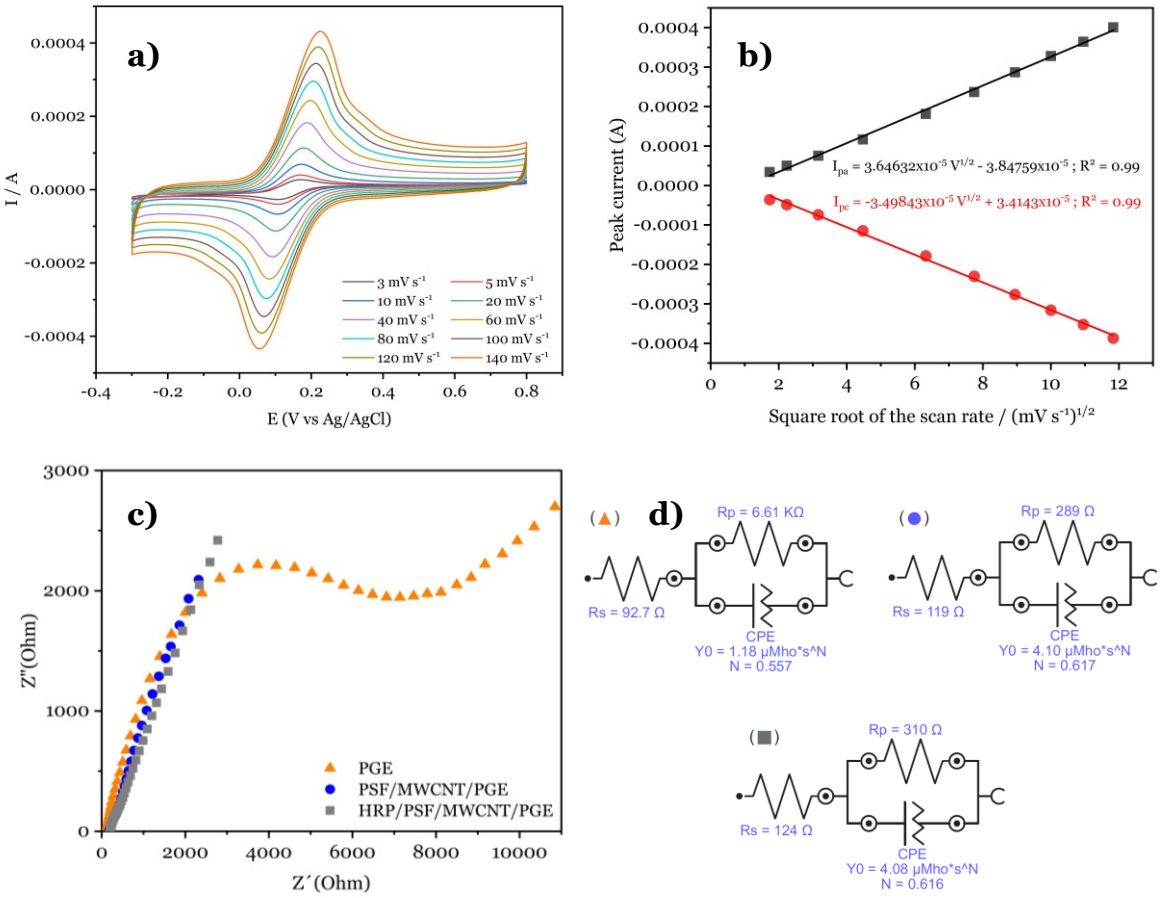


Figure 5.2. a) Cyclic voltammetry results for the effect of HRP/PSF/MWCNT/PGE scan rate in an equimolar 5 mmol L^{-1} solution of $Fe(CN)_6^{3-/4-}$ with 0. 1 mol L^{-1} KCl (3 to 140 mV s^{-1}), b) I_{pa} and I_{pc} versus square root of the scan rate, c) Electrochemical impedance spectroscopic measurements of PGE (▲), PSF/MWCNT/PGE (●), and HRP/PSF/MWCNT/PGE (■), and d) circuit model for evaluation of the parameters.

For mechanical polished PGE, an impedance semicircle centred below the x-axis was obtained at higher frequencies due to surface roughness and double-layer capacitance at the electrode/electrolyte interface translated by the electron charge transfer resistance of

about R_{ct} = 6610Ω (51). The straight line at low frequencies, corresponding to Warburg impedance, showed near quadrant bisector slope due to response dictated by controlled diffusion and the absence of adsorptive phenomena. On contrary, the highly electrically-conductive MWCNT present in the membrane of both modified PGEs significantly decreased the impedance to heterogeneous charge transfer, with a slight increase in electrical resistance, for the low conductivity of HRP coating the electroactive surface of the electrode (R_{ct} = 310 Ω). This change in the charge-transfer resistance also confirms the immobilization of the enzyme on the PSF/MWCNT membrane as previously reported by others (52).

5.3.2. Morphological characterization of the glyphosate biosensor

The effective entrapment of the HRP enzyme in the PSF/MWCNT membrane was ascertained by FTIR-ATR vibrational spectroscopic analysis, a technique reported by other authors to determine enzyme immobilization (53–56). To this, FTIR spectra from HRP/PSF/MWCNT membranes were compared with those assigned to PSF (57). Here, peaks with typical wavenumbers of the amide group and peptide bond were determined, which are indicative of successful enzyme immobilization (Figure 5.3).

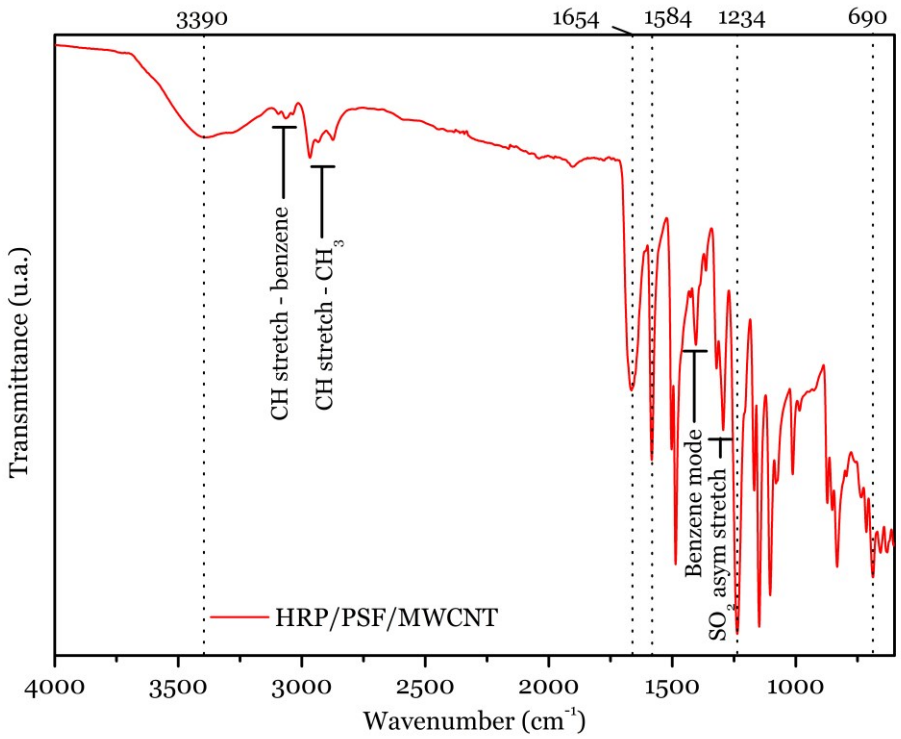


Figure 5.3. FTIR-ATR of the membrane with the immobilized enzyme. The main features of the PSF polymer are indicated in blue color.

A new broad spectral band appeared between 3100-3700 cm^{-1} indicating N-H stretch vibrations from amide or amine groups restrained by hydrogen bridges. However, the broad band centered at 1654 cm^{-1} resulting from a ~30 cm^{-1} bathochromic shift of the C=O stretch vibration in the vicinity of N-H (80% of C=O stretch) points out to amide groups. The intense peaks at respectively 1584 and 1234 cm^{-1} N–H bend and C–N stretch, are typical of secondary amides prevalent in the parallel β-sheet structure of HRP. Finally, the peak at 690 cm^{-1} was due to the out-of-plane N-H bend (58).

A rough and heterogeneous membrane was in turn observed in SEM-EDS micrographs, in which the PSF is evidenced by bright zones and the presence of dark zones revealing the discrete phase composed by MWCNT (Figure 5.4a). For the correct assignment of these regions, Energy-Dispersive X-Ray spectroscopic analysis was applied to the identified membrane regions (Z1, Z2, and Z3) (Figure 5.4b-d). While carbon prevailed in darker region Z1, a higher presence of both carbon and oxygen in the backbone of PSF polymer was associated with whiter regions. The widespread presence of sulfur is related to PSF since it is a constituent of its chemical structure. The presence of iron is observed at brighter locations such as point Z3 (Figure 5.4d) and corresponded to the presence of the enzyme in higher amounts since the active site of HRP possesses an iron atom coordinated equatorially by a porphyrin ring and axially by the imidazole group of His170 of HRP. The presence of this element proves the successful immobilization of HRP on the PSF/MWCNT membrane. This determination corroborates the use of EDS to confirm the immobilization of HRP on a recognition membrane (56,59). Finally, the presence of elements such as P and K are related to the PBS solution used in the coagulation bath that contained the enzyme. The chemical and physical properties of PSF polymer, as well as the membrane morphology, enabled a proper distribution and immobilization of MWCNTs and HRP on the surface, maintaining the appropriate mechanical resistance, necessary to be attached to the transducer.

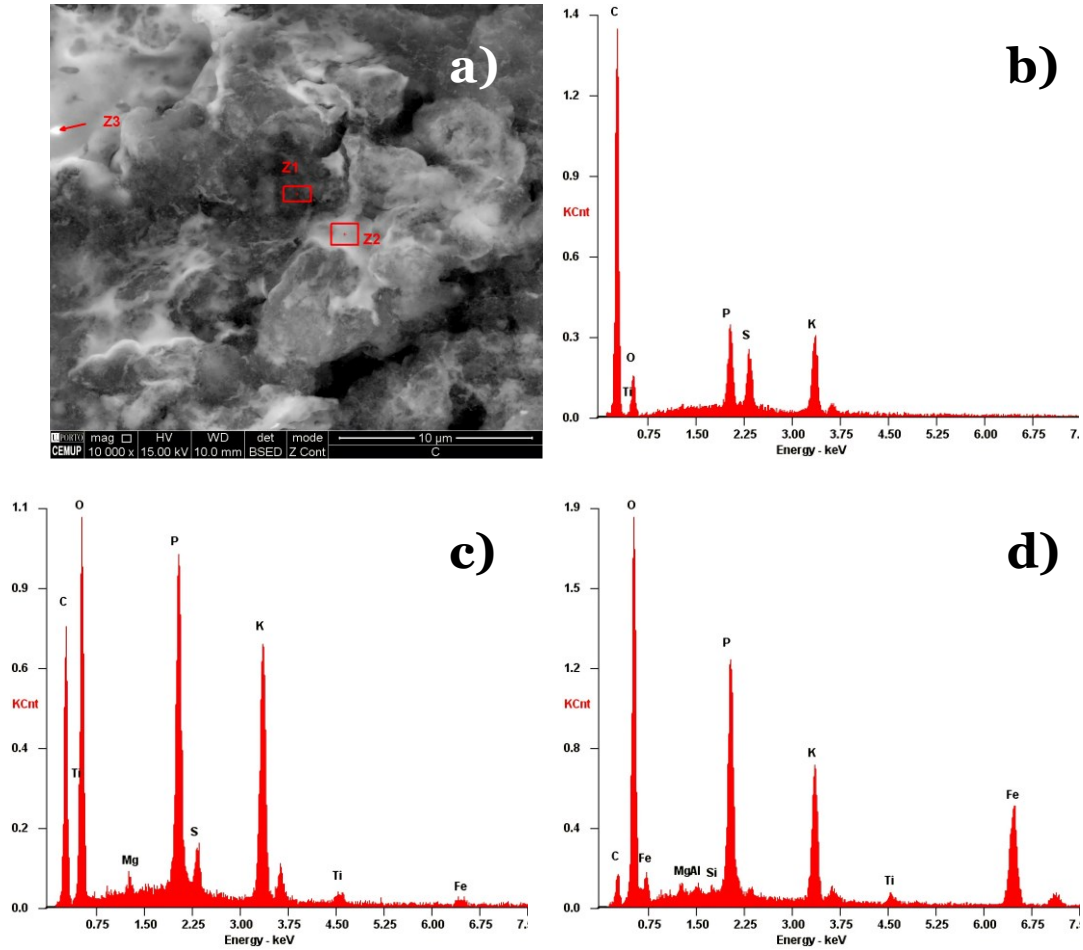


Figure 5.4. SEM micrographs of the HRP/PSF/MWCNT membrane (a); EDS spectrum for Z1 (b), Z2 (c), Z3 (d)

5.3.3. Characterization of the electrochemical GLY biosensor

The electron transfer responsible for the electrochemical reduction or oxidation of the redox center of the HRP enzyme was observed in the presence of the enzyme-substrate H_2O_2, thus excluding the described electrode from the third-generation biosensors group.

In second-generation amperometric biosensors, dissolved charge transfer redox mediators are applied to diffuse their oxidized/reduced forms between the redox active site of the enzyme to the electrode (60). As shown in Figure 5.5a, the electrode response changed significantly after increasing the volumes of substrate added to the electrolyte solution which consists of 10 mL of a 0.1 mol L^{-1} solution of PBS (pH 6) and 1.8 mmol L^{-1} of HQ as mediator. The potential anodic sweep from -0.2 up to +0.6 V (scan rate of 10 mV s^{-1}) revealed a potential peak at +0.075 V (vs Ag/AgCl) related to the oxidation of hydroquinone to p-benzoquinone. After reversing the sweep direction, a cathodic peak at approximately -0.02 V (vs Ag/AgCl), corresponding to the electrochemical reduction of p-benzoquinone on the biosensor surface, became apparent. Accordingly, a positive correlation was obtained

between the H_2O_2 concentration in the range of 1 to 20 mmol L^{-1} (Figure 5.5b), and the peak intensity of the catalytic reduction, which was related to the electrochemical reduction of H_2O_2 on the biosensor surface.

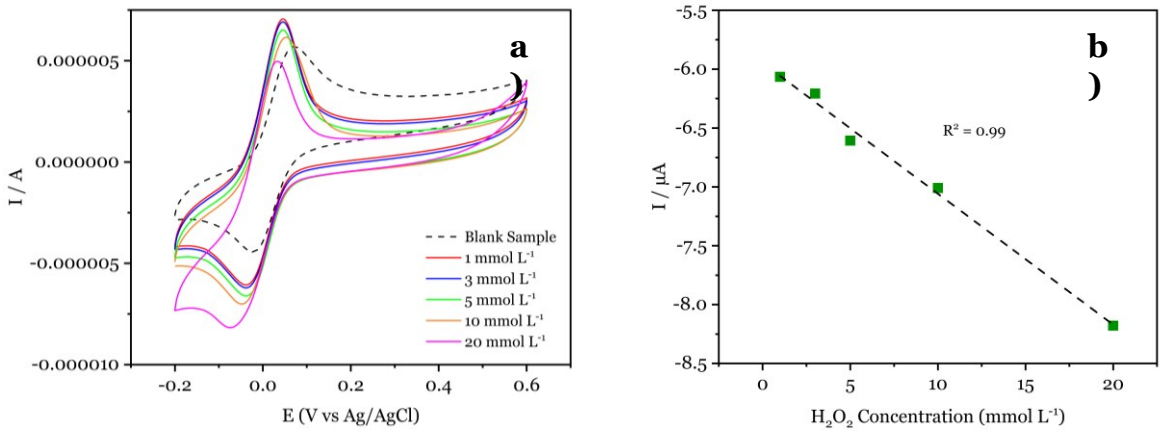


Figure 5.5. a) Cyclic voltammetry for HRP/PSF/MWCNT/PGE biosensor under different H_2O_2 concentrations, and b) Linear representation of the CV test for catalytic reduction. Conditions: 1.8 mmol L^{-1} of HQ; 0.1 mol L^{-1} PBS (pH 6); scan rate 10 mV s^{-1} (vs Ag/AgCl).

It should be noted that in addition to charge transfer between the enzyme and the electrode, it is important to understand the charge carrier pathways and their dynamics within the applied peroxidase. For this reason, the catalytic mechanism of peroxidase (HRP) in the presence of H_2O_2 and quinones (benzoquinone and hydroquinone (HQ)) is represented by the following sequence of reactions (Figure 5.6) (61). This catalytic cyclic representation demonstrates the importance of the connection between the electrode, the enzyme, and the redox mediator, to ensure the transport of charge for hydrogen peroxide reduction, and to maintain the HQ oxidation/reduction cycle for other generated quinones.

Finally, voltammetric tests showed a reduction peak shift from -0.02 V to -0.05 V (vs Ag/AgCl), when H_2O_2 concentration increases (Figure 5.5). Therefore, the latter was selected as the working potential for the subsequent amperometric tests since it guarantees the reduction of H_2O_2.

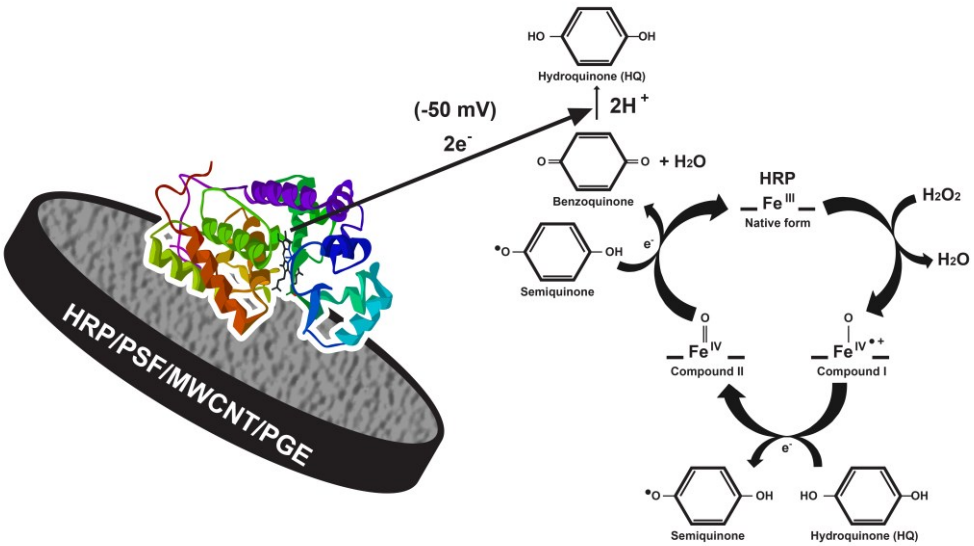


Figure 5.6. The catalytic cycle representation of the proposed sensing mechanism between HRP with H_2O_2 and HQ (compounds I and II denote enzyme intermediates in the reaction)

To improve the amperometric response of the proposed biosensor, different HRP concentrations in the coagulation bath were used (50, 100, 200, and 300 U mL^{-1}), and consequently the amount of enzyme immobilized in the PSF membrane. The slope of the linear regression equation, representing the sensitivity of the biosensor (μA $μM^{-1}$), was used as the selection criterion for choosing the best membrane composition. The correspondent biosensors were evaluated under the following conditions: 10 mL of 0.1 mol L^{-1} PBS (pH 6), 1.8 mmol L^{-1} HQ, 200 rpm stirring agitation, and -0.05 V potential (vs Ag/AgCl). After a current stabilization (around 150 s), 10 successive H_2O_2 injections of 50 μL at 10 mmol L^{-1} (prepared in the same bulk solution to avoid HQ dilution effects) were applied. Based on this, the biosensor which showed the best sensitivity ($5.27x10^{-3}$ ± $9.53x10^{-5}$ μA $μM^{-1}$; Figure S4) was the one prepared with 100 U mL^{-1} of HRP. For 50 U mL^{-1} enzyme concentration, the reduction of H_2O_2 did not follow a zero-order kinetic reaction. On the other hand, at 200 and 300 U mL^{-1} HRP concentrations, the overpopulation of HRP on the surface may generate resistance to electron transfer. These results were confirmed by EIS, where the membranes prepared in a coagulation bath with 100 U mL^{-1} HRP showed no significant difference in the electrical resistance when compared to the membrane without enzyme.

The influence of the pH of the bulk solution on the biosensor response was also tested. For this, PBS buffer 0.1 mol L^{-1} was prepared at pH 5.8, 6.0, 6.6, 7.0, and 7.4. Under the conditions previously reported (HQ concentration, electrolyte, stirring, and H_2O_2 injections), the sensitivity of the biosensor at each pH was calculated (Figure S5). The best response

was obtained for the already reported pH, which is optimum for the HRP activity (pH 6; $5.27x10^{-3} \pm 9.53x10^{-5}$ μA $μM^{-1}$) (62). The PBS concentration was evaluated, as well as the influence of the ionic strength. This test was performed at 0.01, 0.05, and 0.1 mol L^{-1} of PBS (pH 6), in the presence of KCl at 0.1 mol L^{-1}. No significant differences in sensitivity with the change in PBS electrolyte concentration (Figure S6) were obtained for ionic strength changes. Nevertheless, 0.01 mol L^{-1} PBS concentration was selected with 0.1 mol L^{-1} of KCl as the electrolyte solution, in which the biosensor sensitivity is $5.42x10^{-3} \pm 3.01x10^{-5}$ μA $μM^{-1}$. Finally, the concentration of HQ in the bulk solution was optimized in the range of 10 nmol L^{-1} to 1.8 mmol L^{-1}. A logarithm growth (Figure S7) of the sensitivity was observed up to about 0.25 mmol L^{-1} HQ, being constant for higher concentrations. Therefore, to ensure the best sensitivity of the biosensor ($5.46x10^{-3} \pm 5.32x10^{-5}$ μA $μM^{-1}$), 0.5 mmol L^{-1} HQ was selected for the final detection tests.

The amperometric response of the optimized biosensor as well as the respective analytical curve for H_2O_2 is depicted in Figure 5.7.

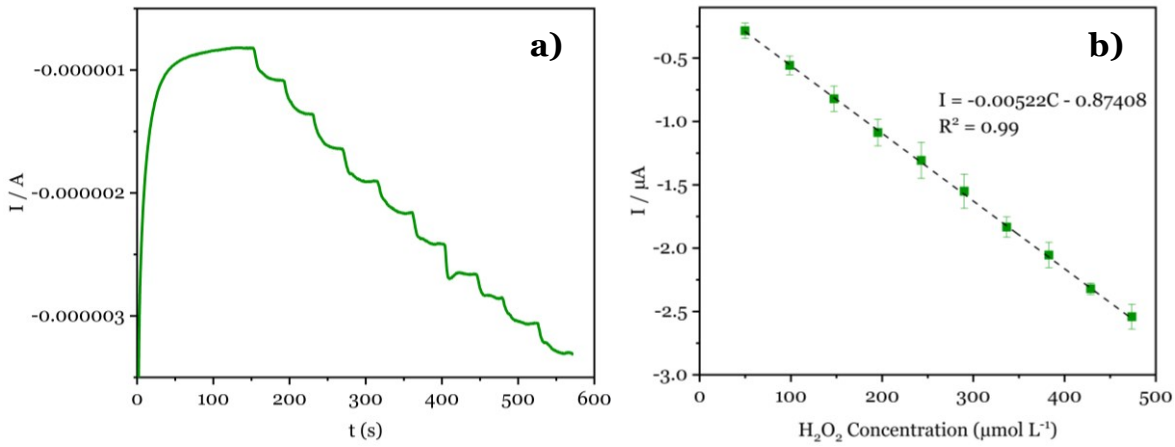


Figure 5.7. a) Amperometric measurements of H_2O_2 with HRP/PSF/MWCNT/PGE; b) Calibration curve plot of the HRP/PSF/MWCNT/PGE. Conditions: 0.01 mol L^{-1} PBS buffer (pH 6); 0.5 mM of HQ; applied potential -0.05 V (vs Ag/AgCl).

The optimized biosensor gave rise to a calibration curve with an analytical range from 49.75 to 473.79 μmol L^{-1} (sensitivity of $5.43 \pm 5.29x10^{-5}$ μA $μM^{-1}$) and with an R^2 of 0.99. Furthermore, the limit of detection (LOD) and limit of quantification (LOQ), calculated based on the signal-to-noise ratio, was 3s/m and 10s/m, respectively, where "s" is the standard deviation of the blank peak currents, and "m" is the slope of the calibration plot. The LOD and LOQ for the proposed sensor were $3.31 \pm 5.61x10^{-2}$ and 11.12 ± 0.87 μmol L^{-1}, respectively.

The maximum rate of the enzyme reaction and the apparent Michaelis-Menten constant can be calculated from the steady-state current and the fitting of the Lineweaver-Burk equation:

$$\frac{1}{I} = \frac{1}{I_{max}} + \frac{K_M}{I_{max}[S]} \qquad \text{(Equation 5.2)}$$

where I (amperes) is the steady-state current obtained after the reaction of the substrate with the enzyme on the biosensor surface; I_{max} (amperes) is the maximum rate of the enzyme reaction; [S] is the molar concentration of the substrate; K_M (mol L^{-1}) is the apparent Michaelis-Menten constant (63). I_{max} and K_M can be calculated from the intercept and the slope are respectively $-3.50 \times 10^{-6} \pm 1.98 \times 10^{-7}$ A and $7.32 \times 10^{-5} \pm 1.33 \times 10^{-7}$ mol L^{-1}. The low concentration reported for K_M indicates the high affinity of the biosensor for H_2O_2. The affinity of this biosensor to the substrate can be compared with the results provided by Yuan et al. (64) and Zhang et al. (65) who reported a K_M of 0.01157 mol L^{-1} and 0.00138 mol L^{-1} for HRP immobilized on chitosan/2D layered double hydroxide composite, and HRP immobilized on magnetic dextran microspheres, respectively, evidencing the higher affinity of the proposed one regarding the described ones. This high affinity is attributed to the optimization of materials and their composition in the recognition membrane to guarantee the immobilization of HRP. In addition, the conditions of the medium ensure that the biocatalytic reaction is adequate between HRP, HQ and H_2O_2, as shown in Figure 5.6.

5.3.4. GLY determination

In this study, the GLY detection was based on the inhibition of HRP activity. The presence of the inhibitor in the peroxidase environment enables its coordination with compound I (Fe(IV)═O) inhibiting the electrocatalytic activity, and thus decreasing the response of the biosensor toward the substrate (66,67).

For a better understanding of the inhibition mechanism, the amperometric response of the biosensor was recorded under different GLY concentrations (0.1, 1.0, 5.0, and 10 mg L^{-1}) after the addition of H_2O_2 up to the concentrations of 0.075 (close to K_M value), 0.33, and 1 mmol L^{-1}. Although, the assay was carried out with three levels of substrate concentration, the Lineweaver-Burk plot (Figure 5.8) shows that the V_{max} was maintained constant for all the studied GLY concentrations (same linear regression intercept), while K_m increased. Based on this, it was concluded that the inhibition mechanism is competitive. According to Songa et al. (68), GLY can coordinate with oxygen atoms in the C=O groups of HRP through its $^{+}NH_2$ group, generating conformational changes in the microstructure of HRP, which obstructs the electron transfer of Fe(III) in the porphyrin cycle of the heme group, thereby inhibiting the catalytic activity of HRP for H_2O_2 reduction. However, as the mechanism of inhibition is competitive, high substrate concentrations will cause the substrate reaction with

the active center of the enzyme, thus displacing the inhibitor. Under these conditions, the effect of the competitive inhibitor can be masked (69). For this reason, the concentration of 0.075 mmol L^{-1} H_2O_2, a concentration near K_M (Michaelis-Menten constant), was set for optimal sensitivity.

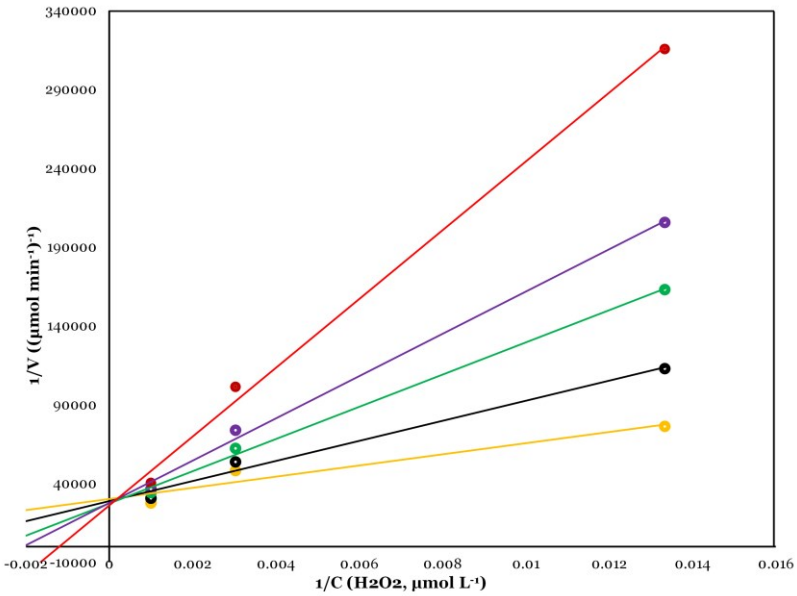


Figure 5.8. Lineweaver-Burk plot for the biosensor response to H_2O_2 in the absence and presence of GLY.

After each test, the biosensor was washed several times and its amperometric response was retested with 10 successive injections of 50 µL of 10 mmol L^{-1} of H_2O_2 (biosensor calibration). The signal return to baseline was evaluated as well as the sensitivity. The results obtained for the purposed show a reversible response of the biosensor sensor. Figure 5.9 represents the amperometric response of the sensor for different GLY concentrations (Figure 5.9a) as well as the corresponding analytical curve (Figure 5.9b). The analytical calibration curve of the percentage of HRP inhibition as a function of the logarithm of GLY concentration shows that the LOD and LOQ are 0.025 ± 0.002 and 0.084 ± 0.007 mg L^{-1}, respectively. The values obtained show that they are suitable for GLY determination in environmental samples since are included in the range of regulated concentrations by EPA (0.7 mg L^{-1}) (21). Additionally, the wide linear range of the GLY biosensor response (0.1 to 10 mg L^{-1}) makes possible its use in the study of the effectiveness of GLY remediation in agricultural and non-agricultural settings. The affordable material for the biosensor preparation as well as the simplicity and easy manipulation make this biosensor a competitive tool for GLY analysis.

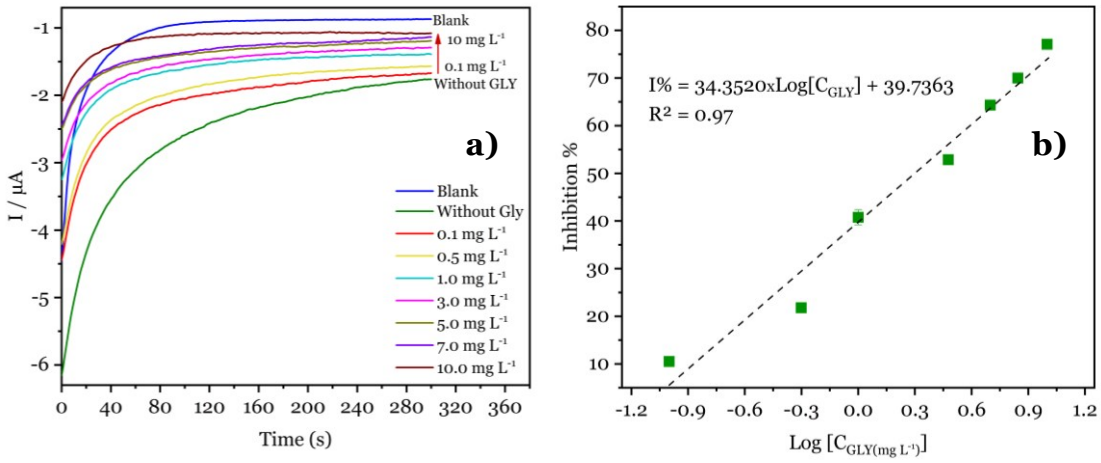


Figure 5.9. a) Amperometric responses for HRP/PSF/MWCNT/PGE in the presence of 0.075 mmol L^{-1} H_2O_2 after interaction with solutions of 0.1, 0.5, 1, 3, 5, 7, and 10 mg L^{-1} of GLY (Conditions: 0.01 mol L^{-1} PBS (pH 6), 0.1 mol L^{-1} KCl, and 0.5 mmol L^{-1} HQ), b) Calibration curve for GLY.

The analytical performance of the developed biosensor was comparable to other GLY detection biosensors reported in the literature (Table S3).Concerning to the LOD value obtained with the developed biosensor is much lower than those reported for Cu/Nanoclay/Graphite Powder/MWCNTs/Atemoya Peroxidase based electrode (30 µg L^{-1}) (70), and for the Agarose-guar gum-Urease-AuNPs based electrode with potentiometric transduction (500 µg L^{-1}) (71). Also about non-enzymatic GLY sensors such as Cu-oxide/hydroxide layers, with 5073 µg L^{-1} (72), NiAl-LDH/Pt with 169.1 µg L^{-1} (73), Cu/GC with 31.45 µg L^{-1} (74), GC/rGO-CuNPs with 32 µg L^{-1} (75), and AuNPs/PB/GLY-Py-MIP with 92 µg L^{-1} (76), the result obtained with the developed biosensor is much better. The good detection sensitivity concerning the sensors above indicated can be attributed to the strong adsorption affinity of HRP by MWCNTs, promoting an improvement in their electrocatalytic activity. In addition, PSF promotes adequate immobilization of the enzyme and also preserves its entire chemical structure. Although other electrochemical detectors with lower detection limits are described in the literature (68,77,78), the materials used in the construction of the developed biosensor compete favorably with conventional electrode support materials, such as copper, gold, and vitreous carbon since, in addition to producing robust detectors that meet the requirements for the detection of GLY imposed by the EPA, provide more reproducible and also cheaper units.

5.3.5. Selectivity, stability, and reproducibility

The effect on the electrochemical signal of the presence of other organic and inorganic species in real samples during the GLY measurements is of great importance. For this

purpose, the study of the interferences was performed in the presence of the pesticides such as dimethoate, methomyl, and mesosulfuron-methyl and also regarding ascorbic acid, glucose, sodium chloride, and sodium bicarbonate. The concentration of these interfering compounds was equal to the GLY in the sample (1 mg L^{-1}). The obtained recovering signals changed between 95.21±0.64% and 103.45±0.94% (Table S4), demonstrating the high selectivity of the biosensor for GLY. It is difficult to make a comparison with the literature data since most authors do not reveal them (27,68,70,77,78). In cases where it is mentioned (71,79,80), the interference values found were better when compared to those presented by other authors, taking into account that the studies were carried out with levels of GLY much lower than the Interfering.

For the evaluation of stability and reproducibility, amperometric tests were run on 3 biosensors for 15 consecutive days, performing the calibration of the biosensor with H_2O_2 before and after being tested with GLY to monitor the sensitivity/catalytic activity of HRP on the substrate. This study shows (Figure 5.10) that the biosensors maintain their catalytic activity for about 10 days, with a decrease from the 11th day demonstrating that can be used for a wide range of time.

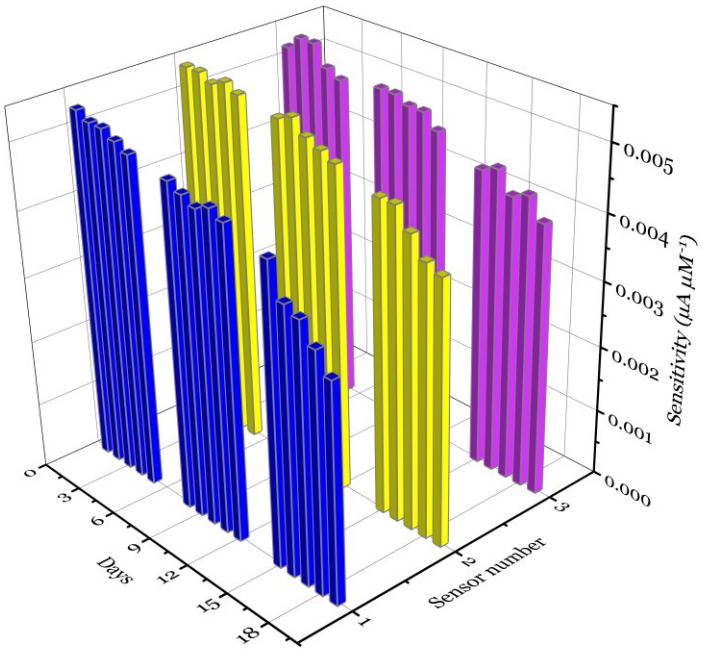


Figure 5.10. The sensitivity (μA μM^{-1}) of three-parallel HRP/PSF/MWCNT/PGE towards H_2O_2 (biosensor calibration process), and the stability within 15 days.

5.3.6. GLY in real samples

The analysis of real water samples (river and tap water) was performed using the standard addition method, to evaluate the matrix effects on the response of the biosensor. For this, the samples were dopped with 1 mg L^{-1} of GLY and analyzed under the same optimized validation conditions. The results show that the biosensor is applicable for the analysis of real water samples since the responses were similar to those of standard samples prepared with ultrapure water from the validation process (data not shown). GLY recoveries in river and tap water were 98.18±0.11% and 97.32±0.23%, respectively. These results indicate that electrochemical detection of GLY by the biosensor HRP/PSF/MWNT/PGE is accurate and suitable as a detection method to be used in real aqueous samples.

5.4. Conclusions

In this study, a new GLY biosensor was developed based on a polysulfone membrane incorporating an enzyme which is deposited on a graphite mine physical support. The electrochemical biosensor response is based on the competitive inhibition of the HRP enzyme by coordination of the NH_2 group with the oxygen atoms present in the carbonyl groups of peroxidase, forming a GLY-enzyme complex not available for further interaction with H_2O_2. The sequence of assays for the optimization of the biosensor response, such as the composition of the membrane, mine type, and variables in the bulk solution, gives rise to a biosensor with high sensitivity for the determination of H_2O_2 and later for GLY. This biosensor was able to respond to H_2O_2 in a wide linear detection range of 49.75 to 473.79 µmol L^{-1} with a LOD of 3.3 µmol L^{-1}. On the other hand, the versatility of the biosensor to be applied to GLY detection showed that this herbicide can be detected in the linear detection range of 0.1 to 10 mg L^{-1}, with a LOD of 0.025 ± 0.002 mg L^{-1}, an ideal condition to comply with regulations such as EPA. The sensitivity and the selectivity of the proposed biosensor against interferences were high making it a valuable tool for routine analysis in real sample waters. The simplicity of construction and the estimated cost for each electrode of about $2 makes this analytical tool a good alternative to the others presented in the literature. This new approach to preparing PSF membranes for biosensors, based on the phase inversion process, in which the recognition element is immobilized, can be extended to other biological entities, sometimes so challenging to ensure the integrity of recognition structures. Furthermore, the results show that the biosensor can be optimized for the detection of other inhibitors, such as other pesticides, heavy metals, etc.

5.5. References

1. Heap I, Duke SO. Overview of glyphosate-resistant weeds worldwide. Pest Manag Sci. 2018;74(5):1040–9.

2. Brito IP, Tropaldi L, Carbonari CA, Velini ED. Hormetic effects of glyphosate on plants. Pest Manag Sci. 2018;74(5):1064–70.

3. Guyton KZ, Loomis D, Grosse Y, El Ghissassi F, Benbrahim-Tallaa L, Guha N, et al. Carcinogenicity of tetrachlorvinphos, parathion, malathion, diazinon, and glyphosate. Lancet Oncol. 2015;16(5):490–1.

4. Muenchen DK, Martinazzo J, Brezolin AN, de Cezaro AM, Rigo AA, Mezarroba MN, et al. Cantilever Functionalization Using Peroxidase Extract of Low Cost for Glyphosate Detection. Appl Biochem Biotechnol. 2018;186(4):1061–73.

5. Pengue WA. Transgenic Crops in Argentina: The Ecological and Social Debt. Bull Sci Technol Soc. 2005;25(4):314–22.

6. WHO/FAO. Report of the joint meeting of the FAO Panel of Experts on pesticide residues in food and the environment and the WHO Core Assessment Group on Pesticide Residues (JMPR). [Internet]. FAO Plant Production and Protection Paper. Rome: World Health Organization/Food and Agriculture Organization of the United Nations.; 2004 Sep.

7. IARC. Some organophosphate insecticides and herbicides [Internet]. Vol. 112, IARC Monographs. Leon: International Agency for Research on Cancer; 2015.

8. Xu J, Smith S, Smith G, Wang W, Li Y. Glyphosate contamination in grains and foods: An overview. Food Control. 2019;106:106710.

9. Melton LM, Taylor MJ, Flynn EE. The utilisation of ion chromatography and tandem mass spectrometry (IC-MS/MS) for the multi-residue simultaneous determination of highly polar anionic pesticides in fruit and vegetables. Food Chem. 2019;298:125028.

10. Van Bruggen AHC, He MM, Shin K, Mai V, Jeong KC, Finckh MR, et al. Environmental and health effects of the herbicide glyphosate. Sci Total Environ. 2018;616–617:255–68.

11. Peillex C, Pelletier M. The impact and toxicity of glyphosate and glyphosate-based herbicides on health and immunity. J Immunotoxicol. 2020;17(1):163–74.

12. Gill JPK, Sethi N, Mohan A, Datta S, Girdhar M. Glyphosate toxicity for animals.

Environ Chem Lett. 2018;16(2):401–26.

13. Samsel A, Seneff S. Glyphosate's Suppression of Cytochrome P450 Enzymes and Amino Acid Biosynthesis by the Gut Microbiome: Pathways to Modern Diseases. Entropy. 2013;15(12):1416–63.

14. Manas F, Peralta L, Raviolo J, Ovando HG, Weyers A, Ugnia L, et al. Genotoxicity of glyphosate assessed by the comet assay and cytogenetic tests. Env Toxicol Pharmacol. 2009;28(1):37–41.

15. Thongprakaisang S, Thiantanawat A, Rangkadilok N, Suriyo T, Satayavivad J. Glyphosate induces human breast cancer cells growth via estrogen receptors. Food Chem Toxicol. 2013;59:129–36.

16. Hokanson R, Fudge R, Chowdhary R, Busbee D. Alteration of estrogen-regulated gene expression in human cells induced by the agricultural and horticultural herbicide glyphosate. Hum Exp Toxicol. 2007;26:747–52.

17. Koller VJ, Fürhacker M, Nersesyan A, Mišík M, Eisenbauer M, Knasmueller S. Cytotoxic and DNA-damaging properties of glyphosate and Roundup in human-derived buccal epithelial cells. Arch Toxicol. 2012;86(5):805–13.

18. Kwiatkowska M, Reszka E, Wozniak K, Jablonska E, Michalowicz J, Bukowska B. DNA damage and methylation induced by glyphosate in human peripheral blood mononuclear cells (in vitro study). Food Chem Toxicol. 2017;105:93–8.

19. Richard S, Moslemi S, Sipahutar H, Benachour N, Seralini GE. Differential effects of glyphosate and roundup on human placental cells and aromatase. Env Heal Perspect. 2005;113(6):716–20.

20. Wozniak E, Sicinska P, Michalowicz J, Wozniak K, Reszka E, Huras B, et al. The mechanism of DNA damage induced by Roundup 360 PLUS, glyphosate and AMPA in human peripheral blood mononuclear cells - genotoxic risk assessement. Food Chem Toxicol. 2018;120:510–22.

21. EPA. National Primary Drinking Water Regulations [Internet]. 2009.

22. Efsa. Conclusion on the peer review of the pesticide risk assessment of the active substance glyphosate. Efsa J. 2015;13(11):107.

23. Valle AL, Mello FCC, Alves-Balvedi RP, Rodrigues LP, Goulart LR. Glyphosate detection: methods, needs and challenges. Environ Chem Lett. 2019;17(1):291–317.

24. Noori JS, Mortensen J, Geto A. Recent Development on the Electrochemical Detection of Selected Pesticides: A Focused Review. Sensors. 2020;20(8).

25. Kimmel DW, LeBlanc G, Meschievitz ME, Cliffel DE. Electrochemical Sensors and Biosensors. Anal Chem. 2012;84(2):685–707.

26. Windmiller JR, Wang J. Wearable Electrochemical Sensors and Biosensors: A Review. Electroanalysis. 2013;25(1):29–46.

27. Balciunas D, Plausinaitis D, Ratautaite V, Ramanaviciene A, Ramanavicius A. Towards electrochemical surface plasmon resonance sensor based on the molecularly imprinted polypyrrole for glyphosate sensing. Talanta. 2022;241:123252.

28. Zambrano-Intriago LA, Amorim CG, Rodríguez-Díaz JM, Araújo AN, Montenegro MCBSM. Challenges in the design of electrochemical sensor for glyphosate-based on new materials and biological recognition. Sci Total Environ. 2021;793:148496.

29. Majewska-Nowak K. Synthesis and properties of polysulfone membranes. Desalination. 1989;71(2):83–95.

30. Bărdacă Urducea C, Nechifor AC, Dimulescu IA, Oprea O, Nechifor G, Totu EE, et al. Control of Nanostructured Polysulfone Membrane Preparation by Phase Inversion Method. Vol. 10, Nanomaterials . 2020.

31. Kohlová M, Rocha S, Gomes Amorim C, de Nova Araújo A, Santos-Silva A, Solich P, et al. Doping Polysulfone Membrane with Alpha-Tocopherol and Alpha-Lipoic Acid for Suppressing Oxidative Stress Induced by Hemodialysis Treatment. Macromol Biosci. 2020;20(7):2000046.

32. Sanchez S, Pumera M, Cabruja E, Fabregas E. Carbon nanotube/polysulfone composite screen-printed electrochemical enzyme biosensors. Analyst. 2007;132(2):142–7.

33. Phelane L, Gouveia-Caridade C, Barsan MM, Baker PGL, Brett CMA, Iwuoha EI. Electrochemical Determination of Tyrosine using a Novel Tyrosinase Multi-Walled Carbon Nanotube (MWCNT) Polysulfone Modified Glassy Carbon Electrode (GCE). Anal Lett. 2020;53(2):308–21.

34. Sanchez S, Pumera M, Fabregas E. Carbon nanotube/polysulfone screen-printed electrochemical immunosensor. Biosens Bioelectron. 2007;23(3):332–40.

35. Macanás J, Farre M, Muñoz M, Alegret S, Muraviev DN. Preparation and characterization of polymer-stabilized metal nanoparticles for sensor applications.

Phys status solidi. 2006;203(6):1194–200.

36. Torrinha Á, Amorim CG, Montenegro MCBSM, Araújo AN. Biosensing based on pencil graphite electrodes. Talanta. 2018;190:235–47.

37. Li T, Wu Y, Huang J, Zhang S. Gas sensors based on membrane diffusion for environmental monitoring. Sensors Actuators B Chem. 2017;243:566–78.

38. Kawde AN, Baig N, Sajid M. Graphite pencil electrodes as electrochemical sensors for environmental analysis: a review of features, developments, and applications. RSC Adv. 2016;6(94):91325–40.

39. Lima HRS, da Silva JS, de Oliveira Farias EA, Teixeira PRS, Eiras C, Nunes LCC. Electrochemical sensors and biosensors for the analysis of antineoplastic drugs. Biosens Bioelectron. 2018;108:27–37.

40. Jing Y, Yu B, Li P, Xiong B, Cheng Y, Li Y, et al. Synthesis of graphene/DPA composite for determination of nicotine in tobacco products. Sci Rep. 2017;7(1):14332.

41. Tan X, Rodrigue D. A Review on Porous Polymeric Membrane Preparation. Part I: Production Techniques with Polysulfone and Poly (Vinylidene Fluoride). Vol. 11, Polymers . 2019.

42. Gauthier MM, International A, Committee ASMIH. Engineered Materials Handbook, Desk Edition [Internet]. Taylor & Francis; 1995. (ASM Handbook).

43. Zhou L, Jiang Y, Chu D. Synthesis and dielectric properties of printable strontium titanate/polyvinylpyrrolidone nanocomposites. Mater Res Express. 2019;6(9):0950c6.

44. Ghiazza M, Vietti G, Fenoglio I. 8 - Carbon nanotubes: properties, applications, and toxicity. In: Njuguna J, Pielichowski K, Zhu HBTH and ES of N, editors. Woodhead Publishing; 2014. p. 147–74.

45. Kukovecz Á, Kozma G, Kónya Z. Multi-Walled Carbon Nanotubes BT - Springer Handbook of Nanomaterials. In: Vajtai R, editor. Berlin, Heidelberg: Springer Berlin Heidelberg; 2013. p. 147–88.

46. Abdallah B, Elhissi AMA, Ahmed W, Najlah M. Chapter 16 - Carbon nanotubes drug delivery system for cancer treatment. In: Ahmed W, Phoenix DA, Jackson MJ, Charalambous CPBTA in M and SE, editors. Academic Press; 2020. p. 313–32.

47. Oliveira TMBF, Morais S. New Generation of Electrochemical Sensors Based on Multi-Walled Carbon Nanotubes. Vol. 8, Applied Sciences . 2018.

48. Down MP, Foster CW, Ji X, Banks CE. Pencil drawn paper based supercapacitors. RSC Adv. 2016;6(84):81130–41.

49. Samukaite-Bubniene U, Valiūnienė A, Bucinskas V, Genys P, Ratautaite V, Ramanaviciene A, et al. Towards supercapacitors: Cyclic voltammetry and fast Fourier transform electrochemical impedance spectroscopy based evaluation of polypyrrole electrochemically deposited on the pencil graphite electrode. Colloids Surfaces A Physicochem Eng Asp. 2021;610:125750.

50. Magar HS, Hassan RYA, Mulchandani A. Electrochemical Impedance Spectroscopy (EIS): Principles, Construction, and Biosensing Applications. Sensors. 2021;21(19).

51. Torrinha Á, Jiyane N, Sabela M, Bisetty K, Montenegro MCBSM, Araújo AN. Nanostructured pencil graphite electrodes for application as high power biocathodes in miniaturized biofuel cells and bio-batteries. Sci Rep. 2020;10(1):16535.

52. Sun M, Shen G, Bai Z, Zhang H, Liu H, Liang X. Electrochemical Determination of Hydrogen Peroxide Using a Horseradish Peroxidase (HRP) Modified Gold–Nickel Alloy Nanoparticles Glassy Carbon Electrode (GCE). Anal Lett. 2021;54(16):2565–73.

53. Wang Q, Xue R, Guo H, Wei YL, Yang W. A facile horseradish peroxidase electrochemical biosensor with surface molecular imprinting based on polyaniline nanotubes. J Electroanal Chem. 2018;817:184–94.

54. Wang A, Ding Y, Li L, Duan D, Mei Q, Zhuang Q, et al. A novel electrochemical enzyme biosensor for detection of 17β-estradiol by mediated electron-transfer system. Talanta. 2019;192:478–85.

55. Waifalkar PP, Chougale AD, Kollu P, Patil PS, Patil PB. Magnetic nanoparticle decorated graphene based electrochemical nanobiosensor for H2O2 sensing using HRP. Colloids Surfaces B Biointerfaces. 2018;167:425–31.

56. Xiong J, Sun Z, Yu J, Liu H, Wang X. Thermal self-regulatory smart biosensor based on horseradish peroxidase-immobilized phase-change microcapsules for enhancing detection of hazardous substances. Chem Eng J. 2022;430:132982.

57. Vico S, Palys B, Buess-Herman C. Hydration of a Polysulfone Anion-Exchange Membrane Studied by Vibrational Spectroscopy. Langmuir. 2003;19(8):3282–7.

58. Smith BC. Organic Nitrogen Compounds, VII: Amides—The Rest of the Story [Internet]. Spectroscopy. 2020. p. 10–5.

59. Behrouzifar F, Shahidi SA, Chekin F, Hosseini S, Ghorbani-HasanSaraei A. Colorimetric assay based on horseradish peroxidase/reduced graphene oxide hybrid for sensitive detection of hydrogen peroxide in beverages. Spectrochim Acta Part A Mol Biomol Spectrosc. 2021;257:119761.

60. Ramanavicius S, Ramanavicius A. Charge Transfer and Biocompatibility Aspects in Conducting Polymer-Based Enzymatic Biosensors and Biofuel Cells. Nanomaterials. 2021;11(2):371.

61. Amine A, Arduini F, Moscone D, Palleschi G. Recent advances in biosensors based on enzyme inhibition. Biosens Bioelectron. 2016;76:180–94.

62. Schomburg D, Salzmann M, Stephan D. Peroxidase BT - Enzyme Handbook 7: Class 1.5–1.12: Oxidoreductases. In: Schomburg D, Salzmann M, Stephan D, editors. Berlin, Heidelberg: Springer Berlin Heidelberg; 1994. p. 747–53.

63. Alarcon-Angeles G, Álvarez-Romero GA, Merkoçi A. Electrochemical Biosensors: Enzyme Kinetics and Role of Nanomaterials. In: Wandelt KBTE of IC, editor. Oxford: Elsevier; 2018. p. 140–55.

64. Yuan J, Xu S, Zeng HY, Cao X, Pan AD, Xiao GF, et al. Hydrogen peroxide biosensor based on chitosan/2D layered double hydroxide composite for the determination of H2O2. Bioelectrochemistry. 2018;123:94–102.

65. Zhang HL, Lai GS, Han DY, Yu AM. An amperometric hydrogen peroxide biosensor based on immobilization of horseradish peroxidase on an electrode modified with magnetic dextran microspheres. Anal Bioanal Chem. 2008;390(3):971–7.

66. Marques PRB de O, Yamanaka H. Biosensors based on the enzymatic inhibition process. Quim Nova. 2008;31(7):1791–9.

67. Yang Y, Yang M, Wang H, Jiang J, Shen G, Yu R. An amperometric horseradish peroxidase inhibition biosensor based on a cysteamine self-assembled monolayer for the determination of sulfides. Sensors Actuators B Chem. 2004;102(1):162–8.

68. Songa EA, Arotiba OA, Owino JHO, Jahed N, Baker PGL, Iwuoha EI. Electrochemical detection of glyphosate herbicide using horseradish peroxidase immobilized on sulfonated polymer matrix. Bioelectrochemistry. 2009;75(2):117–23.

69. Engelking LR. Chapter 6 - Enzyme Kinetics. In: Engelking LRBTT of VPC (Third E,

editor. Boston: Academic Press; 2015. p. 32–8.

70. Oliveira GC, Moccelini SK, Castilho M, Terezo AJ, Possavatz J, Magalhães MRL, et al. Biosensor based on atemoya peroxidase immobilised on modified nanoclay for glyphosate biomonitoring. Talanta. 2012;98:130–6.

71. Vaghela C, Kulkarni M, Haram S, Aiyer R, Karve M. A novel inhibition based biosensor using urease nanoconjugate entrapped biocomposite membrane for potentiometric glyphosate detection. Int J Biol Macromol. 2018;108:32–40.

72. Sierra EV, Méndez MA, Sarria VM, Cortés MT. Electrooxidación de glifosato sobre electrodos de níquel y cobre. Quim Nova. 2008;31(2):220–6.

73. Khenifi A, Derriche Z, Forano C, Prevot V, Mousty C, Scavetta E, et al. Glyphosate and glufosinate detection at electrogenerated NiAl-LDH thin films. Anal Chim Acta. 2009;654(2):97–102.

74. Aguirre MDC, Urreta SE, Gomez CG. A Cu2+-Cu/glassy carbon system for glyphosate determination. Sensors Actuators, B Chem. 2019;284:675–83.

75. Setznagl S, Cesarino I. Copper nanoparticles and reduced graphene oxide modified a glassy carbon electrode for the determination of glyphosate in water samples. Int J Environ Anal Chem. 2020;1–13.

76. Xu J, Zhang Y, Wu K, Zhang L, Ge S, Yu J. A molecularly imprinted polypyrrole for ultrasensitive voltammetric determination of glyphosate. Microchim Acta. 2017;184(7):1959–67.

77. Roman RL, Nagi L, Silva LL, Fernandes SC, de Mello JMM, Magro JD, et al. Monocrystalline silicon/polyaniline/horseradish peroxidase enzyme electrode obtained by the electrodeposition method for the electrochemical detection of glyphosate. J Mater Sci Mater Electron. 2020 [2021 May 19];31(12):9443–56.

78. Sok V, Fragoso A. Amperometric biosensor for glyphosate based on the inhibition of tyrosinase conjugated to carbon nano-onions in a chitosan matrix on a screen-printed electrode. Microchim Acta. 2019;186(8):569.

79. Cahuantzi-Muñoz SL, González-Fuentes MA, Ortiz-Frade LA, Torres E, Ţălu Ş, Trejo G, et al. Electrochemical Biosensor for Sensitive Quantification of Glyphosate in Maize Kernels. Electroanalysis. 2019;31(5):927–35.

80. Kergaravat S V, Fabiano SN, Soutullo AR, Hernández SR. Comparison of the performance analytical of two glyphosate electrochemical screening methods based on peroxidase enzyme inhibition. Microchem J. 2021;160:105654.

5.6. Supplementary Data

Table S1. Factorial designs for biosensor

Sensor No.	PSF %	PVP %	MWCNT %	HRP (U/mL)
1	15	0	0.5	100
2	5	20	0.5	100
3	5	0	0.5	100
4	10	10	0.5	100
5	10	20	0.5	100
6	5	5	0.5	100
7	5	10	0.5	100
8	20	5	0.5	100
9	1	5	0.5	100
10	20	15	0.5	100
11	15	20	0.5	100
12	15	15	0.5	100
13	10	5	0.5	100
14	15	10	0.5	100
15	20	20	0.5	100
16	20	10	0.5	100
17	15	5	0.5	100
18	5	15	0.5	100
19	10	15	0.5	100
20	1	20	0.5	100
21	20	0	0.5	100
22	1	15	0.5	100
23	1	10	0.5	100
24	10	0	0.5	100
25	1	0	0.5	100

Table S2. Voltammetric responses of the biosensor constituents of the factorial design.

Scan Rate 10mV s^{-1}		
Sensor	**Ip, a**	**Ip, c**
0	1.513E-05	-1.563E-05
1	4.426E-06	-4.607E-06
3	**7.521E-05**	**-7.451E-05**
4	2.296E-05	-2.551E-05
5	1.674E-05	-1.823E-05
6	2.109E-05	-2.647E-05
7	2.208E-05	-2.906E-05
8	7.353E-06	-1.022E-05
10	7.467E-06	-1.346E-05
11	1.773E-05	-2.109E-05
12	1.341E-05	-1.672E-05
13	4.70E-06	-6.736E-06
14	1.2926E-05	-1.708E-05
15	1.807E-05	-2.667E-05
16	8.185E-06	-1.005E-05
17	1.291E-05	-1.337E-05
19	1.975E-05	-2.201E-05
24	3.465E-05	-3.887E-05

Table S3. Comparison of the biosensors for the detection of GLY

Sensor configuration	**Linear range (µg L^{-1})**	**LOD (µg L^{-1})**	**Ref.**
Enzymatic			
HRP/PSF/MWCNT/PGE	100 - 10000	25	This work
Cu/Nanoclay/Graphite powder/MWCNTs/Atemoya Peroxidase	100 - 4550	30	(1)
Agarose-guar gum-Ureasa-AuNPs	500 - 50000	500	(2)
HRP/PDMA-PSS/Au	0.25 - 14.0	1.70	(3)

n-Si/PAni/HRP	-	16.9	(4)
SPE/Chi/CNO/TYR	2.5 - 1690	1.1	(5)
Non-enzymatic			
Cu-oxide/hydroxide layers	-	5073	(6)
NiAl-LDH/Pt	1691 - 152190	169.1	(7)
Cu/GC	67.64 - 1691	31.45	(8)
GC/rGO-CuNPs	16.9 - 186	32	(9)
AuNPs/PB/GLY-Py-MIP	400 - 1200	92	(10)

Table S4. Effects of potentially interfering species on the inhibition efficiency of GLY in the HRP/PSF/MWCNT/PGE biosensor

Interfering substances	**Recovery (%)**
Dimethoate	95.21±0.64
Methomyl	98.18±0.89
Mesosulfuron-methyl	103.45±0.94
Ascorbic acid	100.41±1.77
Glucose	101.08±2.25
Sodium chloride	96.65±1.13
Sodium bicarbonate	96.54±0.52

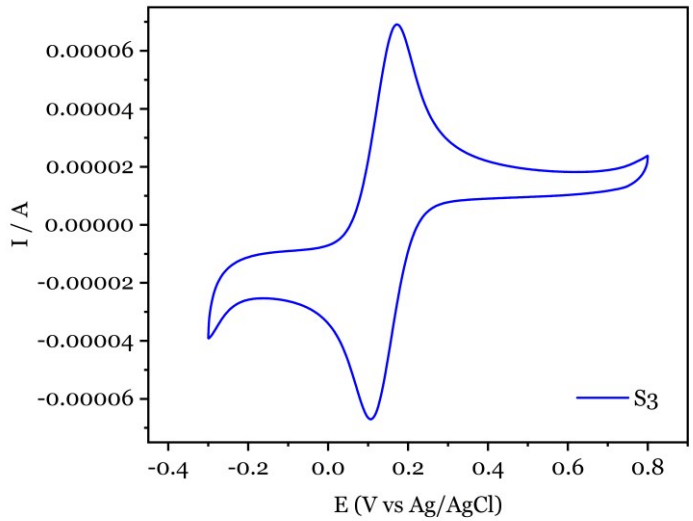


Figure S1. CV response of sensor 3 (vs Ag/AgCl, Scan rate 10 mV s^{-1}; CV measurements of the PSF/MWCNTs/PGE in 0.1M KCl, 5 mM $K_3[Fe(CN)_6]$ and 5mM $K_4[Fe(CN)_6]$ aqueous electrolyte at room temperature)

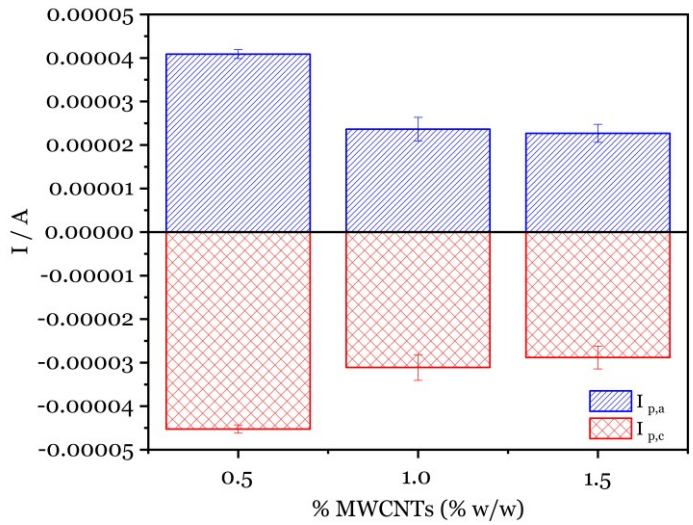


Figure S2. Analysis of the MWCNTs concentration (Obtained from CV measurements of the PSF/MWCNTs/PGE in 0.1M KCl, 5 mM $K_3[Fe(CN)_6]$ and 5mM $K_4[Fe(CN)_6]$ aqueous electrolyte at room temperature)

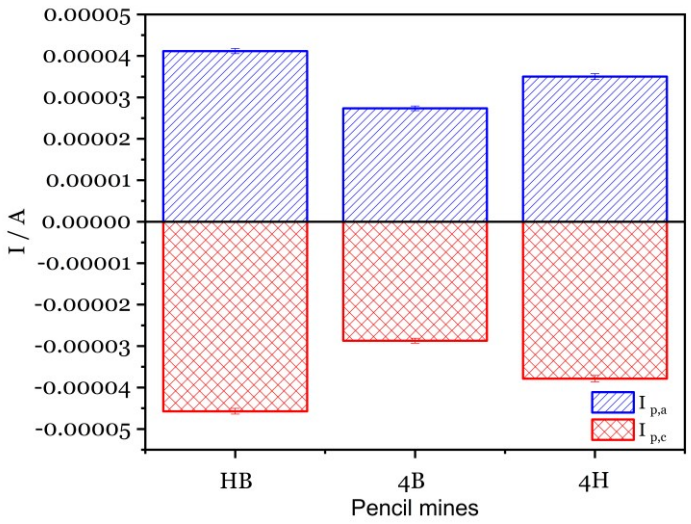


Figure S3. Analysis of the pencil mines (Obtained from CV measurements of the PSF/MWCNTs/PGE in 0.1M KCl, 5 mM $K_3[Fe(CN)_6]$ and 5mM $K_4[Fe(CN)_6]$ aqueous electrolyte at room temperature)

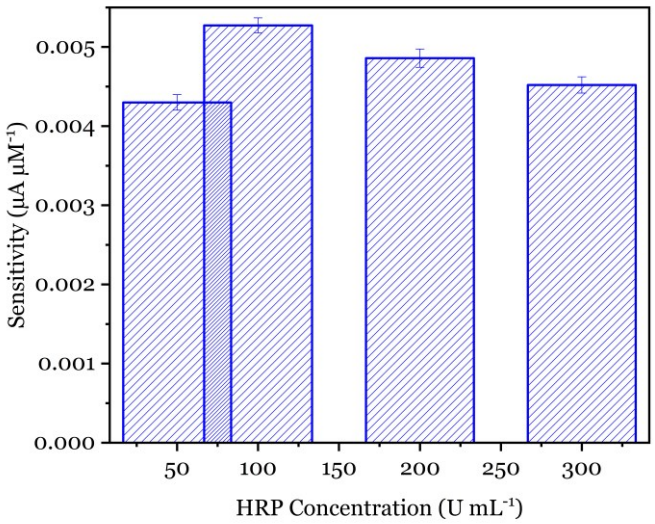


Figure S4. Influence of HRP concentration on phase inversion (Obtained from amperometric response of the HRP/PSF/MWCNTs/PGE in 0.1M PBS (pH 6.0), and 1.8 mM HQ to the successive injections of 10 mmol L^{-1} H_2O_2)

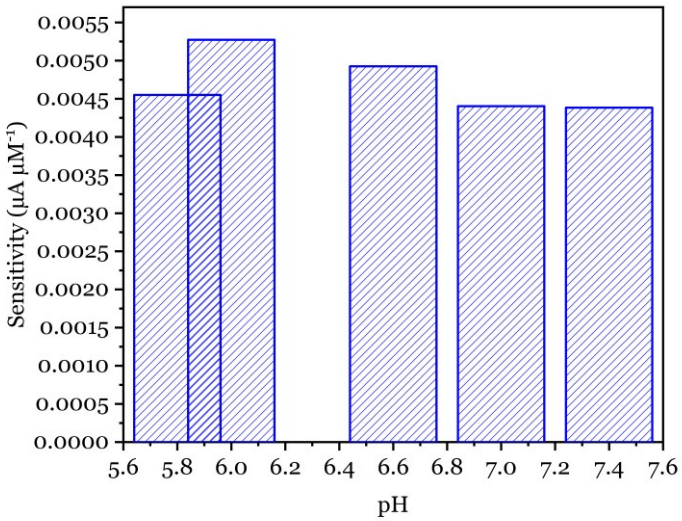


Figure S5. pH Influence in amperometric response (Obtained from amperometric response of the HRP/PSF/MWCNTs/PGE in 0.1M PBS, and 1.8 mM HQ to the successive injections of 10 mmol L^{-1} H_2O_2)

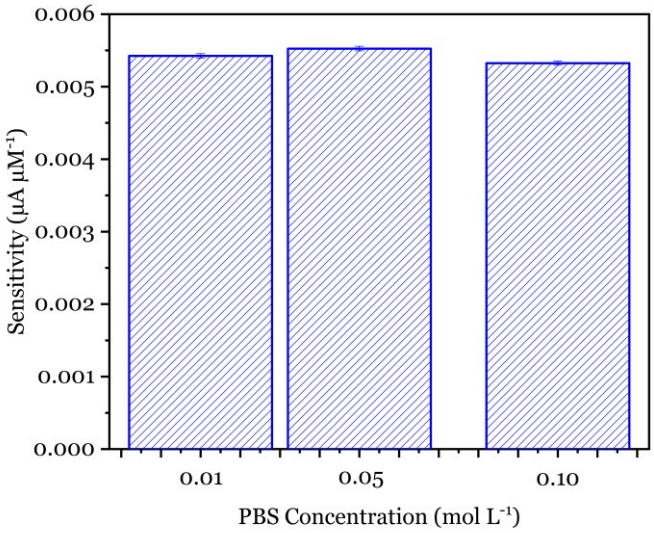


Figure S6. Ionic strength influence in the amperometric response (Obtained from amperometric response of the HRP/PSF/MWCNTs/PGE in PBS (pH 6), 0.1 M KCl, and 1.8 mM HQ to the successive injections of 10 mmol L^{-1} H_2O_2)

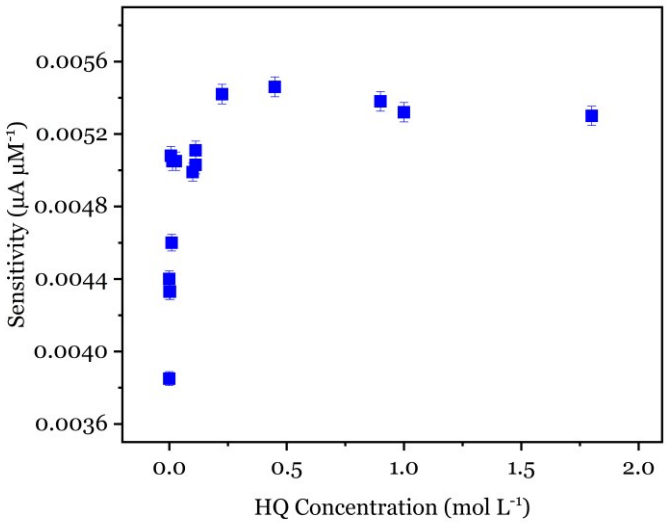


Figure S7. Influence of HQ concentration in the amperometric response (Obtained from the amperometric response of the HRP/PSF/MWCNTs/PGE in 0.01 M PBS (pH 6), and 0.1 M KCl to the successive injections of 10 mmol L^{-1} H_2O_2)

References

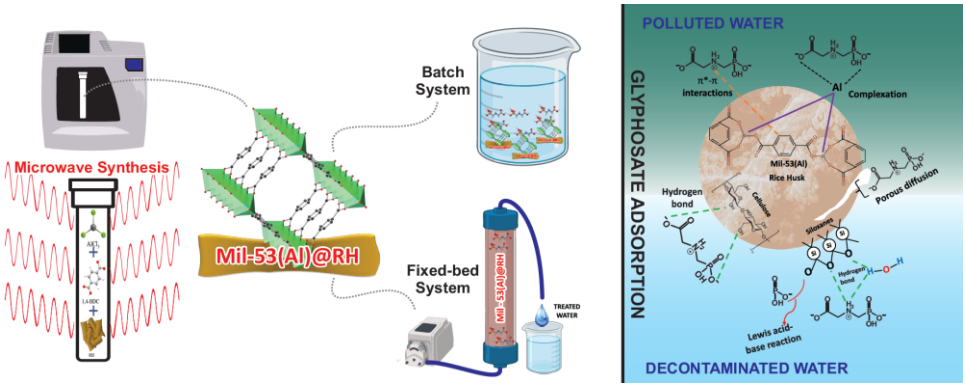
1. Oliveira GC, Moccelini SK, Castilho M, Terezo AJ, Possavatz J, Magalhães MRL, et al. Biosensor based on atemoya peroxidase immobilised on modified nanoclay for glyphosate biomonitoring. Talanta. 2012;98:130–6.
2. Vaghela C, Kulkarni M, Haram S, Aiyer R, Karve M. A novel inhibition based biosensor using urease nanoconjugate entrapped biocomposite membrane for potentiometric glyphosate detection. Int J Biol Macromol. 2018;108:32–40.
3. Songa EA, Arotiba OA, Owino JHO, Jahed N, Baker PGL, Iwuoha EI. Electrochemical detection of glyphosate herbicide using horseradish peroxidase immobilized on sulfonated polymer matrix. Bioelectrochemistry. 2009;75(2):117–23.
4. Roman RL, Nagi L, Silva LL, Fernandes SC, de Mello JMM, Magro JD, et al. Monocrystalline silicon/polyaniline/horseradish peroxidase enzyme electrode obtained by the electrodeposition method for the electrochemical detection of glyphosate. J Mater Sci Mater Electron. 2020 [2021 May 19];31(12):9443–56.
5. Sok V, Fragoso A. Amperometric biosensor for glyphosate based on the inhibition of tyrosinase conjugated to carbon nano-onions in a chitosan matrix on a screen-printed electrode. Microchim Acta. 2019;186(8):569.
6. Sierra EV, Méndez MA, Sarria VM, Cortés MT. Electrooxidación de glifosato sobre electrodos de níquel y cobre. Quim Nova. 2008;31(2):220–6.
7. Khenifi A, Derriche Z, Forano C, Prevot V, Mousty C, Scavetta E, et al. Glyphosate

and glufosinate detection at electrogenerated NiAl-LDH thin films. Anal Chim Acta. 2009;654(2):97–102.

8. Aguirre MDC, Urreta SE, Gomez CG. A Cu2+-Cu/glassy carbon system for glyphosate determination. Sensors Actuators, B Chem. 2019;284:675–83.
9. Setznagl S, Cesarino I. Copper nanoparticles and reduced graphene oxide modified a glassy carbon electrode for the determination of glyphosate in water samples. Int J Environ Anal Chem. 2020;1–13.
10. Xu J, Zhang Y, Wu K, Zhang L, Ge S, Yu J. A molecularly imprinted polypyrrole for ultrasensitive voltammetric determination of glyphosate. Microchim Acta. 2017;184(7):1959–67.

Chapter 6

Application of a novel hybrid MIL-53(Al)@rice husk for the adsorption of glyphosate in water: Characteristics and mechanism of the process.



Chapter 6 describes the study of a glyphosate adsorption system through a hybrid material Mil-53(Al)@RH, in a batch and column system[3]

[3] This is a partial translation of the article *Zambrano-Intriago LA, Daza-López EV, Fernández-Andrade A, Luque R, Amorim CG, Araújo AN, Rodríguez-Díaz JM, Montenegro MCBSM. Application of a novel hybrid MIL-53(Al)@rice husk for the adsorption of glyphosate in water: Characteristics and mechanism of the process. Chemosphere. 2023;327: 138457.* Copyright 2023, with permission from Elsevier

6.1. Introduction

Water contamination by highly harmful pesticides has been manifested all over the world, bringing great impacts to the environment and, consequently, to human health (1). Glyphosate (GLY), a non-selective post-emergence herbicide, is widely used for weed control, mainly on genetically modified crops, tolerant to GLY, owing to its high efficiency and systemic destructive effect (2). However, its excessive application has induced residues in environmental matrices such as surface and groundwater and can be introduced into the human body through food chains (3–7). The World Health Organization (WHO) considers the molecule harmless to humans (8), nonetheless, the International Agency for Research on Cancer (9), reports that it has the potential to induce cancer. Additionally, studies have demonstrated a positive association between GLY exposure and serious diseases, such as neoplasm/tumor and fetotoxicity (10–12), neuronal alterations (13), and cardiocirculatory and muscular disorders (13,14).

In this context, it is urgent to use effective methods to remove this pollutant from environmental matrices. Techniques such as biodegradation (15,16), membrane filtration (17,18), and advanced oxidation processes (19,20) have been applied for the removal of GLY from water. However, they can be compromised by the low concentration levels they can treat, the requirement of expensive technology and high energy consumption (21–23). Alternatively adsorption techniques may be viable for the removal of pollutants in aqueous matrices due to their low cost, simple procedure, flexibility, and high efficiency (24). Currently, there are commercial adsorbents that can be used for water purification, such as carbon-rich materials, activated carbon, zeolites, etc. However, their use may be compromised by low selectivity and poor adsorption capacity for pesticides such as GLY (25). For this reason, the scientific community has focused on the development of new adsorbents, with high adsorption capacity, easy separation and reuse. Lately, adsorbents based on Metal-Organic Frameworks (MOFs) typify substantial progress in the development of the new generation of adsorbent materials. MOFs are highly porous crystalline materials composed of multifunctional organic linkers and metal clusters. They possess high specific surface areas, regular pores, and abundant active sites, so they are considered promising materials in the field of in/organic pollutant treatment (26–28). Many types of MOFs have been developed for the adsorption of pollutants in wastewater, among them the MILs (Materials Institute Lavoisier) series, aluminum-based MIL-53(Al), which has a surface area of 500 $m^2\ g^{-1}$. A unique feature of MIL-53(Al) is its high thermal stability and structural flexibility to expand and contract by adjusting the pore shape and size to accommodate different types of molecules (29,30). However, its application may be limited by its particle sizes (100-1000 nm) which are not very suitable for applications where

adsorption columns are necessary, as they may generate pressure drops and thus plug inside the column. In addition, their application can be limited by the difficulty of phase separation at the end of treatment. For this reason, in recent years work has been carried out on alternatives to solve these disadvantages of MOFs, with functionalization-hybridization with bioadsorbents being the most frequently reported (31). Bioadsorbents, such as rice husk (RH), have been widely studied for the removal of pesticides (32,33), due to their chemical composition, particle size, and bioavailability, becoming an attractive material for hybridization with MOFs (MOF@biomass). Thus, a solution is provided to the problems of MOFs such as particle size, and the limited adsorption capacity for biomasses. To date, functionalization between biosorbents and MOFs has demonstrated beneficial effects on hybrid adsorbents. According Gurav et al. (34) these hybrids exhibit characteristics such as large surface area and versatility, low toxicity, reusability, cost-effectiveness, disposability, and large-scale production from readily available materials. As a result, a series of MOFs hybridized with biomass have been synthesized as new selective and efficient adsorbents. In addition, a material that takes advantage of its pristine physicochemical properties is achieved, highlighting the diversity of pore sizes and functional groups, which can promote different routes of adsorption mechanisms (31).
In the present study, a hybrid adsorbent MIL-53(Al)@RH was applied as a potential adsorbent in the removal of GLY in aqueous media in batch and column system.

6.2. Experimental section

6.2.1. Materials

Glyphosate (PESTANAL, analytical standard), HKUST-1 (Cu-BTC MOF), Nafion (5 wt.%), formic acid dimethylamide (DMF ACS reagent, ≥99.8%), potassium phosphate dibasic (ACS reagent, ≥98%), 1,4-Benzenedicarboxylic acid (for synthesis), and Aluminium chloride hexahydrate (ReagentPlus, 99%) were obtained from Sigma-Aldrich. Ethyl alcohol (absolute for analysis EMSURE), potassium chloride (for analysis EMSURE), sodium chloride (ACS reagent, ≥99.0%), hydrochloric acid (ACS reagent, 37%), and sodium hydroxide (reagent grade, ≥98%, pellets (anhydrous)) were obtained from Merck. Potassium phosphate monobasic (ACS reagent, ≥99.0%) was acquired from Applichem. A glassy carbon rod (3 mm) was obtained from Alfa Aesar. Shielded copper cable and flexible polymer sleeve were acquired from a local electronics store.

6.2.2. Measurements of GLY

GLY quantification was performed using an electrochemical sensor reproduced from Gu et al. (35) connected to a Metrohm DropSens bipotentiostat, model μStat 200. Using the DPV (Differential Pulse Voltammetry) technique between -0.3 - +0.3 V with CuOx@mC/GCE as working electrode, a reference electrode (Ag/AgCl) and a counter electrode (Pt). Applying

a sampling width of 0.0167 s, and an amplitude width of 0.2 s. Concentration measurements were performed in the presence of 0.1 M PBS and 0.05 M NaCl, in an analytical measurement range between 0.5 and 16 mg L^{-1}. The measurements had a maximum coefficient of variation (CV) of 5%. The raw data related to the analytical method can be found into the Mendeley Data base (https://doi.org/10.17632/89ghm7v984.1).

6.2.3. Synthesis of MIL-53(Al)@RH

In this work, a MIL-53(Al)@RH layered hybrid synthesized by microwave assistance, developed by our research group in a previous work was utilized (36). For this, RH was alkaline hydrolyzed by immersing 30 g of the biomass in a 15% w/w NaOH solution with subsequent heating at 180°C for 4 hours. Then it was washed several times with distilled water until neutralization was achieved, followed by drying at 105 °C for 24 hours. On the other hand, the synthesis of MIL-53(Al) was performed in the presence of hydrolyzed RH. For this purpose, in a vessel containing 6 mL of ultrapure water, 15 mmol of $AlCl_3 \bullet 6H_2O$ and 2 g of RH were dissolved in another vessel containing 60 mL of DMF, 16 mmol of 1,4-Benzenedicarboxylic acid was dissolved with vigorous stirring at 300 rpm. Finally, both solutions were combined with constant stirring to obtain a crystalline blend for placement in Teflon tubing, which was inserted in a microwave oven (CEM MARS) under radiation at 125 °C and 200 W reaction power for 60 min. The resulting material was washed three times with DMF and then with distilled water. Finally, this was dried for 24 hours at 60 °C and a MIL-53(Al)@RH layered hybrid was obtained.

Material characterization was determined through the use of standard procedures. The specific surface area was calculated from N_2 adsorption and desorption isotherms obtained on a Micromeritics Gemini VII 2390 series, which were fitted to the Brunauer-Emmett-Teller (BET) model. Thermogravimetric analyses (TGA) were performed using a Netzsch-Gerätebau GmbH - STA409 PCLuxx in a temperature range from 100 to 700 °C, at a heating rate of 10 °C min^{-1} and inert atmosphere (N_2). The morphology was analyzed by Scanning Electron Microscopy (SEM), using a JEOL JSM-6610LV, with images obtained at 3000 X magnification and 7 KV. X-Ray Diffraction (XRD) patterns were obtained using a Rigaku X-Ray Diffractometer Smartlab, with Theta-Theta Bragg-Brentano geometry, a D/teX model Ultra 250 solid-state detector, and Cu radiation (1541 Å) at 30 mA and 40 kV. Fourier Transform Infrared Spectra (FTIR) were obtained on a Thermo Scientific Nicolet Summit Pro with Thermo Scientific Everest Diamond ATR (Attenuated total reflection) Accessory. The spectra were averaged over 32 scans in the range of 4000 to 600 cm^{-1}. Finally, the point of zero charge (pHpzc) was determined by the graphical method (37).

6.2.4. Adsorption tests

Adsorption experiments were performed in batch mode with 50 mL of solution at 298.15 K employing an orbital shaker (Eppendorf). All samples were developed three times (variation less at 5%).

The adsorption capacity (qe, mg g^{-1}) was calculated employing Equation 6.1.:

$$q_e = \frac{(C_o - C_e)V}{w} \qquad \text{Equation 6.1}$$

where C_0 is the initial concentration of GLY (mg L^{-1}), Ce is the equilibrium concentration (mg L^{-1}), *w* is the mass of the adsorbent (g), and V is the volume of solution (L).

The adsorbent dosage effect (*w*) was analyzed using a solution of GLY at 100 mg L^{-1}, with the agitation of 300 rpm at 298.15 K for 180 min. The GLY solutions were contacted with exact quantities of MIL-53(Al)@RH ranging from 0.001 to 0.08 g. The adsorption capacity of each dose was calculated via Equation 6.1.

The pH effect of the solution (pH_0) on adsorption was performed by adjusting the pH_0 of GLY (100 mg L^{-1}) in the range of 2 to 10. The solutions were put in contact with the determined adsorbent dose, agitation at 300 rpm, at 298.15 K for 180 min.

The contact time effect of the adsorption process was analyzed in the GLY concentration range from 20 to 400 mg L^{-1} for 1 to 90 min, at the best conditions of adsorbent dosage, pH_0, and 298.15 K. These results were subsequently used for modeling the adsorption kinetics and equilibrium (isotherms). In addition, based on the equilibrium time established in the contact time study, equilibrium assays were also performed at 288.15, 313.15, and 328.15 K, in the same range of 20 to 400 mg L^{-1}.

6.2.5. Adsorption kinetics and isotherms

The pseudo-first order (PFO), pseudo-second order (PSO), Bangham, Avrami, and intraparticle diffusion kinetic models were then applied to interpret the kinetic data. On the other hand, Langmuir, Freundlich, Sips, Toth, and Khan models, were used to describe the adsorption equilibrium at 288.15, 298.15, 313.15, and 328.15 K. The equations of the models are shown in Supplementary data S1. The modeling to obtain the kinetic and equilibrium parameters were obtained employing non-linear estimation with the Statistica 10.0 software.

6.2.6. Estimation of adsorption thermodynamics

The thermodynamic parameters were determined by the equations shown in S2. The constants used for the application of the thermodynamic equations were obtained from the equilibrium models that presented the best fit to the adsorption isotherms at different temperatures.

6.2.7. Fixed-bed adsorption experiments

The dynamic adsorption study was performed using a 5 mm diameter × 30 mm height column filled with 0.2 g of MIL-53(Al)@RH and varying of GLY concentration (25, 50 and 100 mg L^{-1}) with a flow rate of 0.3 mL min^{-1}, with the aid of a multichannel peristaltic pump (Masterflex L/S 7535-04). Samples were collected every 20 min until bed saturation employing a fraction collector (Gilson). With the data obtained at the three concentrations evaluated, the total adsorption capacity qt (mg g^{-1}) equivalent to the amount of adsorbate retained at saturation (C = 95% Co), and adsorption capacity at breakthrough point qu (mg g^{-1}) (C = 5% Co) were calculated (38,39). The adsorption capacities qt and qu were determined through Equations 6.2, 6.3 and 6.4, where Co and C (mmol L^{-1}) are the initial and the outlet of the column concentration, M is the molar mass, Q (mL min^{-1}) is the flow of feed, tr and ts (min) are the breakthrough and saturation times, m is the mass of the adsorbent, MTZ (cm) is mass transfer zone, and H is the height of the bed

$$q_t = \frac{M \cdot C_0 \cdot Q}{1000 \cdot m} \int_0^{ts} \left(1 - \frac{C}{C_0}\right) dt \quad \text{(Equation 6.2)}$$

$$q_u = \frac{M \cdot C_0 \cdot Q}{1000 \cdot m} \int_0^{tr} \left(1 - \frac{C}{C_0}\right) dt \quad \text{(Equation 6.3)}$$

$$MTZ = \left(1 - \frac{q_u}{q_t}\right) H \quad \text{(Equation 6.4)}$$

All of the data associated with this study is available at Mendeley Data (https://doi.org/10.17632/89ghm7v984.1).

6.3. Results and discussion

6.3.1. Mil-53(Al)@RH properties

MIL-53(Al)@RH is a material that retains the physical and chemical properties of its pristine materials (MIL-53(Al) and RH) (36). Through BET analysis it was determined that MIL-53(Al)@RH is a mesoporous material (7.12 nm) with a surface area of 46 m^2 g^{-1} (Figure 6.1a). The thermal stability of MIL-53(Al)@RH was determined by TGA since it can withstand temperatures up to 140°C without suffering weight loss due to decomposition (characteristic of MIL-53(Al)) (Figure 6.1b), which is favorable for the treatment of aqueous matrices at high temperatures. Scanning electron microscopy (SEM) showed the crystalline habit orthorhombic and cubic of MIL-53(Al) adhered to the RH fibers (Figure 6.1c), which indicated the effectiveness of hybridization. In addition, the mean size of the MIL-53(Al)@RH particles is 275.67 µm. XRD determined that the hybrid has the primary material properties, mainly by the crystallinity of the main MOF peaks (Figure 6.1d). FTIR analysis of MIL-53(Al)@RH , MIL-53(Al), and RH indicates that there is a significant presence of the MOF in the biomass, once the main functional groups of both pristine materials are manifested, confirming the distribution of crystals over the RH surface (Figure 6.1e).

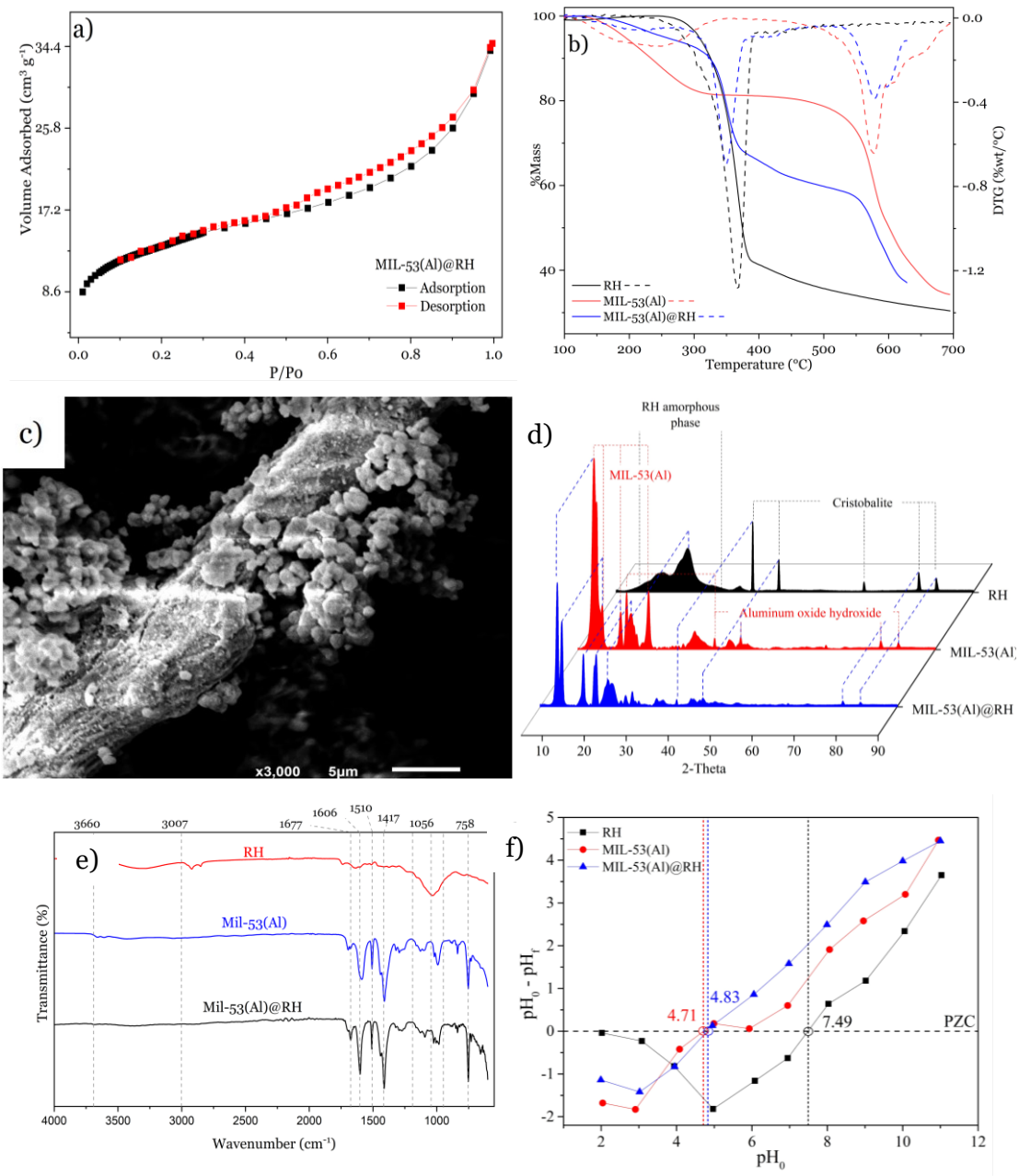


Figure 6.1. Characterization of MIL-53(Al)@RH layered hybrid a) Nitrogen adsorption and desorption isotherm, b) thermal stability (TGA-DTG) of the hybrid and its parent independent materials (RH and MIL-53), c) scanning electron microscope (SEM), d) XRD patterns , e) FTIR spectra, and f) pHpzc graphical method

The pHpzc is 4.81 (Figure 6.1f), which indicates a positive charge on the surface and a predominance of the MIL-53(Al). Moreover, pHpzc determines that the charge of the adsorbent surface will be mainly positive when the solution pH is below 4.81, due to the protonation of the groups on the surface, favoring the adsorption of anions. On the other hand, the charge of the surface is mainly negative at solution pH above 4.81, due to the

deprotonation of the functional groups, favoring cation adsorption. Lastly, the charge is zero when the pH of the solution is equal to pHpzc. These results may contribute to deciphering the adsorption mechanism.

Therefore, the application of this material as an adsorbent is favored by the combined properties of pristine materials, such as the high adsorption capacity of MOFs, and a large amount of metal active sites that can influence the adsorption mechanisms. On the other hand, the presence of biomass favors the combination of functional groups and their particle size in phase separation.

6.3.2. Batch adsorption

6.3.2.1. Effect of adsorbent dose

This assay determines the minimal quantity of sorbent necessary to obtain the highest removal of the adsorbate. This assay was developed with a solution of GLY at 100 mg L^{-1} and pH 4.52 (natural pH). Evaluating adsorption capacity in function of the adsorbent dose (Figure 6.2a), it is observed that in the range of 0.001 to 0.03 g there is a significant reduction in adsorption capacity, with a tendency to remain constant from 0.04 g onwards. Although 0.001 g can be considered the dose with the highest adsorption capacity, it does not mean that this is the optimal value since, according to equation 1, the adsorption capacity varies inversely with the adsorbent mass (w) (37). In addition, the adsorption sites are smaller at low adsorbent doses, which increase proportionally with the dose used until reaching a value at which the adsorbent saturation occurs. To corroborate this behavior, a second analysis was carried out according to the removal percentage, which indicates that from 0.04 g onwards 98.88 ± 0.036 % is removed, maintaining the same trend up to 0.08 g applied. Therefore, the dose of 0.04g/50mL is considered the adequate dose for GLY adsorption using MIL-53(Al)@RH.

6.3.2.2. pH_0 Solution Effect

The pH_0 influences the surface charge of the MIL-53(Al)@RH (pHpzc study), and also the state of the GLY molecule (charge properties). As such, GLY possesses four pK_a values: 0.78, 2.29, 5.96, and 10.98. At pH below 0.78, the molecule is positively charged due to protonation at the amine site; in the range of 0.78 to 2.29 it presents a neutral charge due to the predominance of dissociation (PO_2H^-) and protonation (NH^{2+}); finally, at pH above 2.29, it maintains an overall negative charge and its negative charge intensities increase with increasing pH_0 (40,41). These conditions allow elucidation of the behavior of the molecule as a function of the surface properties of the hybrid. With the pH_0 effect test, it was observed (Figure 6.2b), that adsorption capacity increases in the range of pH_0 2 to 4, and then decreased between pH_0 6 and 10. This indicates that at pH_0 2 the neutral charge of

GLY is not favored by the positive charges on the adsorbent, in addition to competition with H^+ which prevents the adsorption process. On the other hand, when pH_0 was 4, the adsorption capacity increased favorably, because the charge of GLY was electronegative and was favored by the electropositive charge of the adsorbent, this being a possible adsorption mechanism. Finally, from pH_0 6 onwards, GLY and the adsorbent were negatively charged, which generated electrostatic repulsion leading to a decrease in adsorption capacity. Moreover, in an alkaline solution, MIL-53(Al) could undergo a breakdown in its structure, which can negatively affect the adsorption of GLY (42,43). In this context, as the highest adsorption capacity was determined at pH_0 4, this condition was constant for the subsequent experiments.

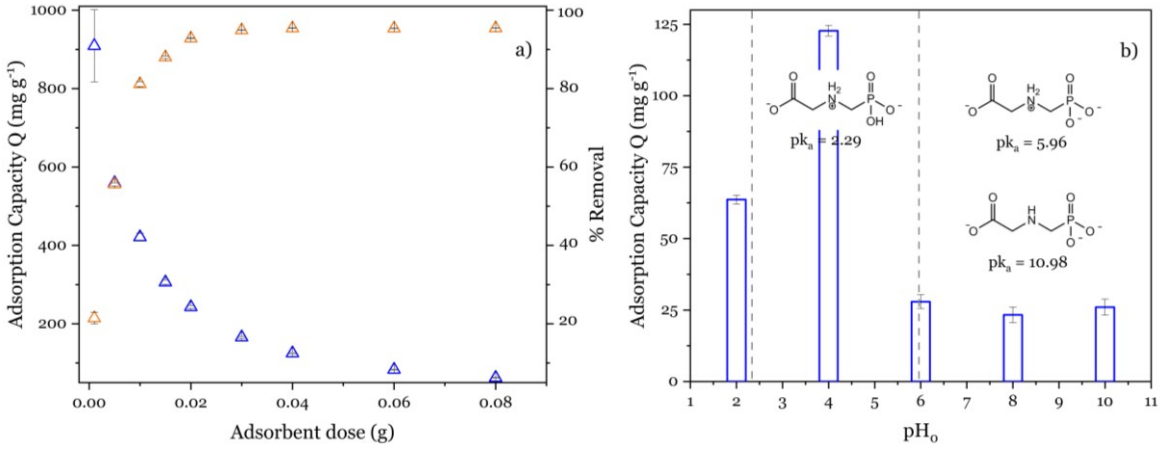


Figure 6.2. a) Adsorbent dose effect on GLY removal using MIL-53(Al)@RH; b) pH_0 effect on GLY removal using MIL-53(Al)@RH. (C_o = 100 mg L^{-1}, t = 180 min, T = 298.15 K).

6.3.2.3. Effect of contact time and adsorption kinetics

This procedure was carried out with solutions ranging from 20 to 400 mg L^{-1} and a contact time of 1 to 90 min to reach equilibrium (Figure 6.3). The removal process occurs rapidly until the first 10 min for all concentrations. After this time, the remotion was slow until equilibrium was achieved at approximately 30 min and maintained similar behavior until the final time of the assay. This behavior could be associated with two-phase adsorption, predominated by a rapid and a relatively slow phase (44). Thus, it may be attributed to the fact that the available active sites of MIL-53(Al)@RH tend to become progressively saturated, and then the adsorbate is slowly adsorbed onto the bulk of the adsorbent. The fast adsorption at initial times is owing to the availability of positively charged groups on the adsorbent, and the decrease in adsorption with time is probably caused by the electrostatic obstacle between the negatively charged adsorbed GLY and the surface. Finally, for the subsequent equilibration studies, the time of 30 min was selected.

The kinetic calculations represent useful information that can explain the mechanism path and the adsorption rate. For this purpose, PFO (45), PSO (46), Avrami (47-49), Bangham (1924), and intraparticle diffusion (51) kinetic models were applied to the results of the contact time effect (Supplementary data). The fits and parameters of the kinetic models are presented in Figure 6.3 and Table 6.1. The evaluation was performed based on the coefficient of determination (R^2), Marquardt's percent standard deviation (MPSD), and hybrid fractional error function (HYBRID) for each of the concentrations studied.

Table 6.1. Kinetic parameters for the adsorption of GLY with MIL-53(Al)@RH

	C_o (mg L^{-1})							
	20	**60**	**100**	**140**	**180**	**240**	**300**	**400**
PFO								
q_t (mg g^{-1})	22.464	66.737	113.876	158.339	192.163	240.176	246.116	254.128
K_1 (min^{-1})	0.738	0.920	0.554	0.558	0.582	0.223	0.275	0.256
HYBRID	8.219	19.458	100.341	87.645	153.718	308.383	221.625	218.167
MPSD	6.730	5.783	10.943	8.720	10.344	16.517	13.514	13.477
R^2	0.904	0.886	0.845	0.904	0.850	0.927	0.940	0.948
PSO								
q_t (mg g^{-1})	23.715	69.872	122.009	169.111	205.092	262.525	268.147	278.956
K_2 (g mg^{-1} min^{-1})	0.051	0.022	0.007	0.005	0.004	0.001	0.001	0.001
HYBRID	1.265	2.997	26.648	15.952	44.652	114.150	65.902	50.358
MPSD	2.578	2.248	5.790	3.669	5.658	9.518	7.013	6.449
R^2	0.985	0.983	0.963	0.982	0.959	0.969	0.980	0.988
Bangham								
β (g mg^{-1})	0.014	0.014	0.012	0.012	0.012	0.008	0.007	0.005
α (mg g^{-1} min^{-1})	0.113	0.093	0.143	0.141	0.135	0.231	0.213	0.228
HYBRID	10.917	20.956	45.275	96.730	95.041	241.514	260.699	259.798
MPSD	7.527	5.993	6.491	8.355	7.265	10.487	10.977	10.978
R^2	0.884	0.891	0.939	0.905	0.918	0.940	0.925	0.936
Avrami								
q_t (mg g^{-1})	23.471	69.779	124.543	167.456	206.498	256.818	260.280	271.714
K_{av} (min^{-1})	0.741	1.042	0.460	0.512	0.520	0.209	0.261	0.230
n_{av}	0.490	0.431	0.435	0.511	0.459	0.591	0.607	0.599

HYBRID	0.630	1.664	6.905	5.811	18.350	53.632	28.958	13.256
MPSD	1.763	1.660	2.798	2.011	3.455	6.027	4.424	3.087
R^2	0.983	0.980	0.978	0.984	0.961	0.965	0.979	0.992
Intraparticle Diffusion								
Stage 1								
K_{dif} (mg g^{-1} $min^{-0.5}$)	3.592	8.711	18.555	27.334	29.413	43.246	50.526	55.353
C	11.009	38.785	49.477	66.011	88.461	56.604	55.885	47.645
HYBRID	3.773	12.377	2.730	21.575	13.278	5.511	2.667	5.459
MPSD	4.964	4.994	1.721	4.469	2.969	2.058	1.244	1.833
R^2	0.949	0.913	0.991	0.963	0.973	0.995	0.997	0.996
Stage 2								
K_{dif} (mg g^{-1} $min^{-0.5}$)	0.698	2.510	6.162	10.602	14.872	26.500	21.278	21.590
C	20.114	57.990	89.250	118.770	135.930	124.190	156.210	156.360
HYBRID	0.024	0.750	0.203	1.371	2.322	0.794	4.803	6.472
MPSD	0.328	1.051	0.425	0.921	1.089	0.580	1.393	1.652
R^2	0.947	0.723	0.972	0.914	0.911	0.987	0.889	0.865
Stage 3								
K_{dif} (mg g^{-1} $min^{-0.5}$)	0.005	0.001	0.154	0.159	-0.596	1.003	1.175	1.747
C	23.163	68.993	119.91	163.380	205.830	240.210	245.320	252.360
HYBRID	0.014	0.016	1.166	0.026	3.450	0.262	0.414	4.658
MPSD	0.252	0.156	0.984	0.126	1.305	0.326	0.404	1.336
R^2	0.026	0.001	0.069	0.717	0.181	0.871	0.851	0.522

According to the obtained kinetic parameters (Table 6.1), the trend of the nonlinear best fit of the models, based on the R^2, and the HYBRID and MPSD values occurs as follows: Avrami > PSO > PFO > Bangham. In the Avrami model, the exponent nAv indicates one type of adsorption mechanism. In this study, for all the concentrations employed the value of nAv was < 1, suggesting that the adsorption of GLY on MIL-53(Al)@RH involves an anion interaction process (52). On the other hand, the calculated value of the theoretical adsorption capacity further demonstrates the good fit of the experimental data to the nonlinear PSO model, which is very close to the experimental adsorption capacity at all concentrations.

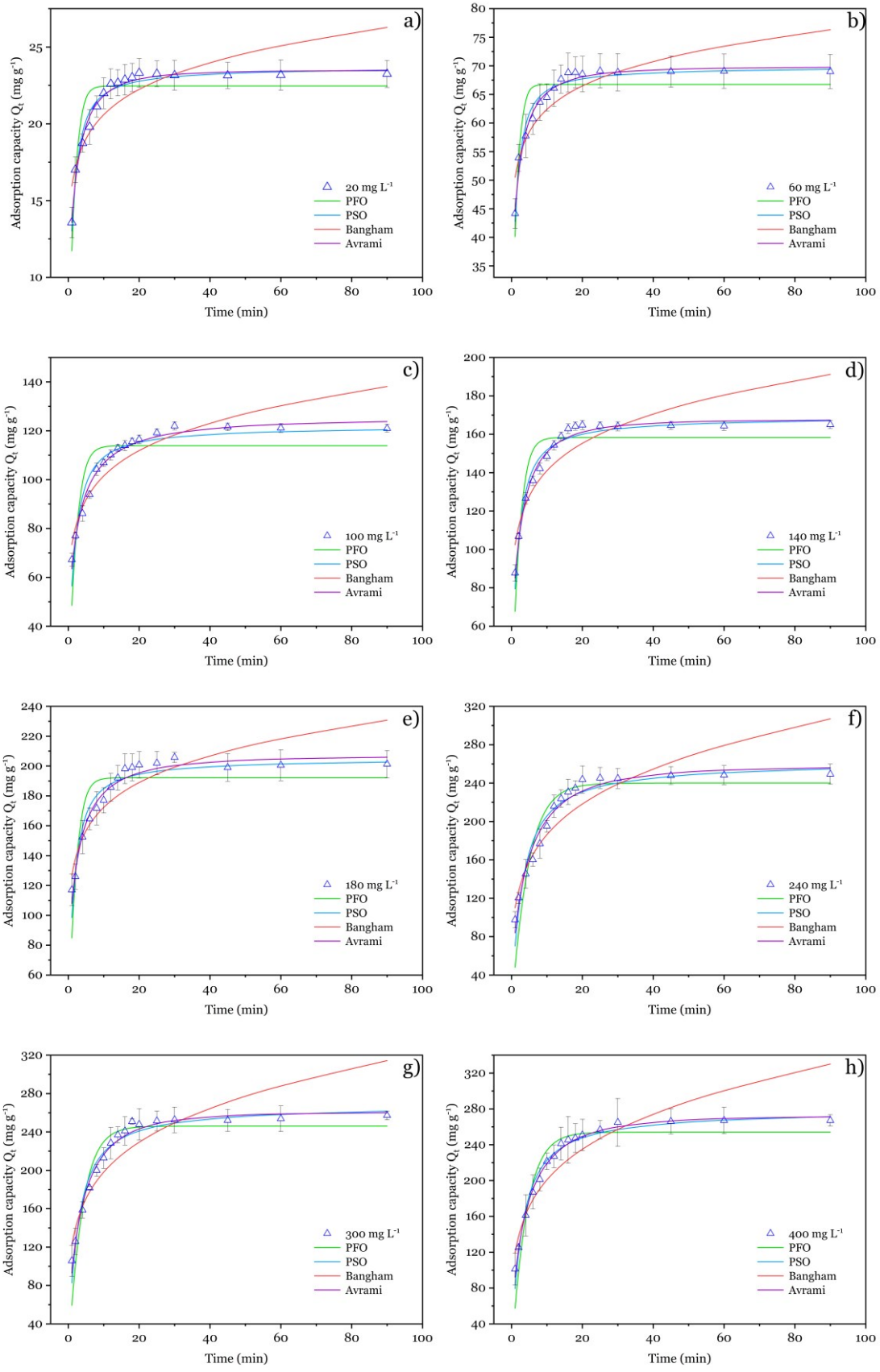


Figure 6.3. Contact time effect on the adsorption of GLY employing MIL-53(Al)@RH, and PFO, PSO, Bangham, and Avrami kinetic models with non-linear adjustment.

Furthermore, PSO model suggests that the adsorption of GLY on MIL-53(Al)@RH would be biased toward the chemisorption mechanism (53). Finally, the slight fit to the PFO model may indicate that the system is accompanied by physical adsorption (54).

To better understand the mechanism of adsorption of GLY, the intraparticle diffusion model was employed. The graphical representation of this model (q_t vs. $t^{0.5}$) is given by the linear relationship of kinetic data in three stages of adsorption (Figure S1). If C is zero, in any of the three stages, the adsorption rate is controlled by intraparticle diffusion. Otherwise, if none of the stages fulfills this condition, or if the graph shows multilinearity, the system can be controlled by multiple stages or combinations thereof (55). Figure S1 demonstrates that all stages are linear and none pass through the origin (0, 0), data that is corroborated by the value of $C \neq 0$ (Table 6.1), so intraparticle diffusion is not the limiting stage controlling the adsorption process, but other mechanisms are occurring simultaneously (56). The first stage shows a higher slope associated with mass transfer from the liquid phase to the adsorbent surface. The second stage shows gradual adsorption, related to pore diffusion, and the third stage (equilibrium) is related to surface diffusion. The highest values of the diffusion constant (K_i) were found at the first stage for all concentrations (Table 6.1), indicating that there is a significant influence of film diffusion, where a higher initial concentration and more active sites accelerate the adhesion of GLY molecules on the surface of MIL-53(Al)@RH in the first stage. Finally, the increase in C from one stage to the next indicates that the effect is greater on the boundary layer.

6.3.2.4. Adsorption isotherms

Adsorption isotherm models can be used to describe how adsorbate molecules are distributed on the adsorbent when the adsorption process achieves an equilibrium state. This study was performed at temperatures of 288.15, 298.15, 313.15, and 328.15 K. The isotherms at the four temperatures were analyzed through the models of Langmuir (57), Freundlich (58), Sips (59), Toth (60), and Khan (61) (Figure 6.4). The parameters are shown in Table 6.2.

Table 6.2. Adsorption isotherm parameters and R^2, HYBRID, and MPSD values for the Langmuir, Freundlich, Sips, Toth, and Khan isotherms at 288.15, 298.15, 313.15, and 328.15 K

	288.15 K	**298.15 K**	**313.15 K**	**328.15 K**
Langmuir				
q_m (mg g^{-1})	303.706	296.953	310.424	329.217
K_L (L mg^{-1})	0.023	0.082	0.267	0.657
R_L	0.684	0.378	0.157	0.070
HYBRID	2578.152	411.680	548.629	143.739
MPSD	134.082	28.104	33.916	11.712
R^2	0.958	0.979	0.985	0.990
Freundlich				
K_F [(mg g^{-1})(L $mg^{-1})^{1/n}$]	28.058	66.198	112.254	137.342
1/n	0.424	0.292	0.223	0.211
HYBRID	5166.541	3017.788	1738.621	3051.919
MPSD	187.182	100.469	74.909	100.452
R^2	0.898	0.901	0.950	0.941
Sips				
q_{max} (mg g^{-1})	232.575	269.698	344.285	350.941
K_s (L mg^{-1})	0.0007	0.028	0.346	0.608
n	0.444	0.652	1.468	1.298
1/n	2.252	1.533	0.681	0.770
HYBRID	206.220	227.142	122.757	135.375
MPSD	36.615	18.444	10.754	15.155
R^2	0.996	0.989	0.994	0.994
Toth				
q_m (mg g^{-1})	376.535	3.059	362.350	6.805
b	12.019	0.307	1.091	0.228
T_h	0.693	-0.084	0.531	-0.068
HYBRID	3863.008	4179.141	154.549	4640.261
MPSD	163.430	119.203	12.742	124.470
R^2	0.945	0.887	0.992	0.927
Khan				
Qs (mg g^{-1})	13.733	33.776	208.828	69.448
b_k	5.446	10.789	0.619	35.068
a_k	0.575	0.710	0.905	0.797
HYBRID	6086.111	3434.287	383.079	2594.081
MPSD	203.015	106.518	26.241	89.839
R^2	0.898	0.904	0.987	0.953

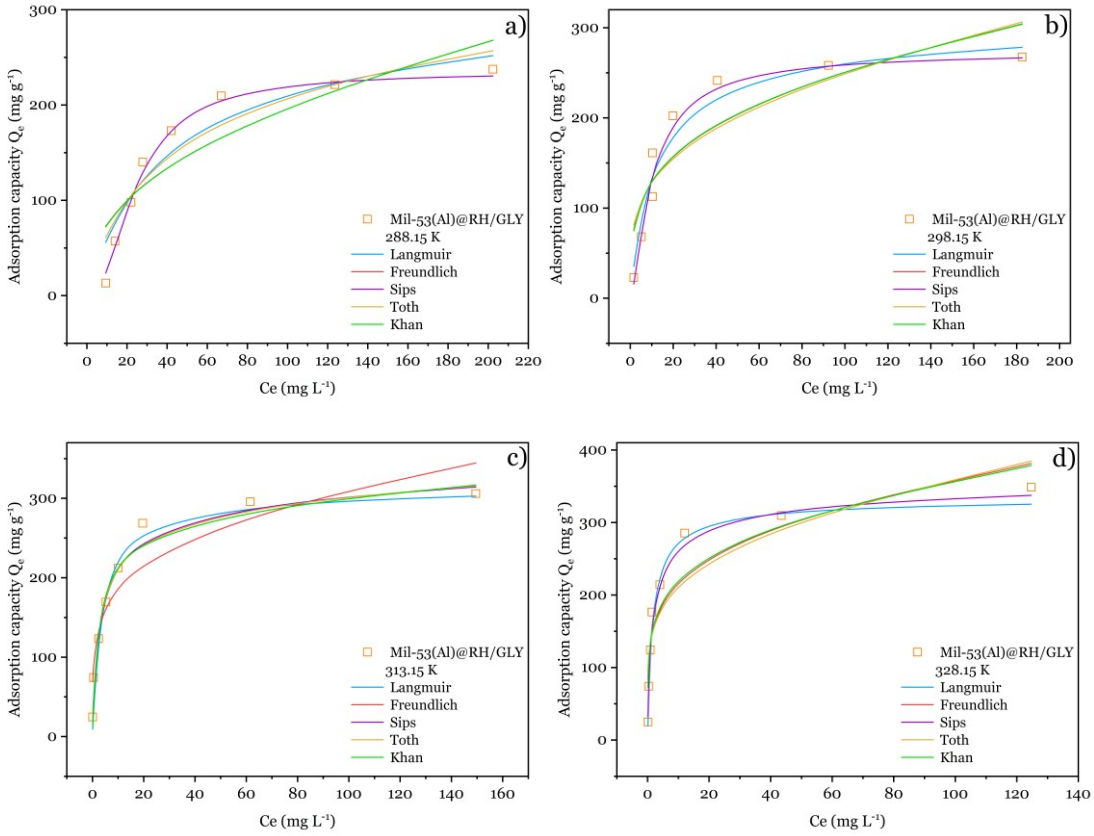


Figure 6.4. Equilibrium isotherms to adsorb GLY using MIL-53(Al)@RH

All models were adequately fit to the experimental isotherms for all temperatures tested. Nevertheless, the models that had the best fit were the Langmuir and Sips models, according to the R^2, HYBRID, and MPSD parameters. In this context, the Langmuir model suggests that adsorption occurs through the formation of a GLY monolayer on the MIL-53(Al)@RH surface, with a finite number of identical and specific adsorption sites. The R_L value was found to be between 0 and 1 for all temperatures, indicating favorable isothermal behavior. Furthermore, the good fit to the Langmuir model proposes that GLY adsorption follows the chemisorption mechanism (62). Thus, it is related to the PSO kinetics model where this mechanism is also proposed, which can be associated with the deprotonated state of the GLY molecule at pH 4 where it can have chemical interactions.

On the other hand, the Sips isotherm combines the Langmuir and Freundlich expressions to predict the heterogeneity of adsorption systems. Sips model does not follow Henry's law due to the reduction of the Freundlich model at low adsorbate concentrations, which relates the poor fit of the Freundlich model with the experimental results. However, at high adsorbate concentration, it predicts Langmuir behavior. Thus, the formation of monolayers governed by chemisorption is corroborated (63).

The Toth isotherm model was also applied, which despite not having a good fit, is an indicator of the heterogeneity of the adsorption system since the constant Th ≠ 1 (63). Finally, the Khan isotherm is a generalized model that represents the Langmuir and Freundlich models when the adsorption of an adsorbate occurs in pure solutions. In this model, if the constant a_K is ≤ 1, it behaves like a Langmuir isotherm (64). In this context, the Khan a_K constant a_K in the isotherms at all temperatures is < 1 (Table 6.2), which corroborates the proposed Langmuir mechanism.

6.3.2.5. Adsorption thermodynamics

Studying the adsorption thermodynamics can define the type of adsorption mechanism of GLY on MIL-53(Al)@RH. The thermodynamic parameters were calculated from the equilibrium constants derived from the Langmuir and Sips models (Table 6.3), once they presented the best fit to the experimental isotherms at different temperatures. The relation for the three thermodynamic parameters follows the Van't Hoff equation (Equation S12).

Table 6.3. Thermodynamic parameters for GLY adsorption onto MIL-53(Al)@RH

Models	**Langmuir**			**Sips**		
	ΔG^0 (KJ mol^{-1})	**ΔH^0 (KJ mol^{-1})**	**ΔS^0 (KJ mol^{-1})**	**ΔG^0 (KJ mol^{-1})**	**ΔH^0 (KJ mol^{-1})**	**ΔS^0 (KJ mol^{-1})**
288.15 K	8.550	64.228	0.193	14.991	129.463	0.397
298.15 K	6.617			11.018		
313.15 K	3.719			5.059		
328.15 K	0.821			-0.899		

The ΔH° of adsorption for the two equilibrium models was positive, confirming that the adsorption of GLY by MIL-53(Al)@RH is an endothermic reaction. This result correctly relates that the adsorption capacity increases with temperature (Figure 6.4). Furthermore, the value of ΔH° can be used to separate the chemisorption process (20.9 - 418.4 KJ mol^{-1}) from the physisorption process (2.1 - 20.9 KJ mol^{-1}) (65). In this study, the ΔH° value reported by Langmuir and Sips model are 64.22 KJ mol^{-1} and 129.46 KJ mol^{-1}, respectively, suggesting a chemisorption dominated process. On the other hand, a positive ΔS° reflects that the randomness of the solid-liquid interface increases with temperature. This increases the species' freedom and makes the process more stable and irreversible. Finally, the decrease of ΔG° indicates that the process is feasible and spontaneous which improves with energy input. The spontaneity can be directly related to the adsorption rate reported in the kinetic study.

6.3.3. Fixed-bed treatment

Fixed-bed tests were performed to verify the continuous application of GLY contaminated water treatment with MIL-53(Al)@RH (Figure 6.5a). Figure 6.5b shows the breakthrough curves corresponding to the study at concentrations of 25, 50, and 100 mg L^{-1} of GLY at a flow rate of 0.3 mL min^{-1}. Desirably, the GLY removal efficiencies were greater than 90% before the breakthrough time, which were 4, 3, and 2.5 hours for 25, 50, and 100 mg L^{-1} of GLY, respectively.

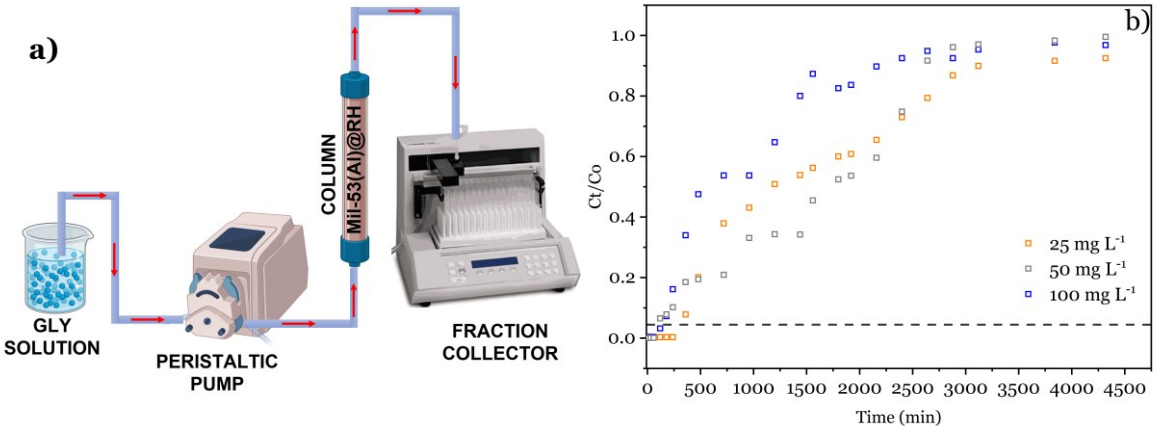


Figure 6.5. a) Scheme of the fixed-bed column adsorption system; b) Breakthrough curves of GLY adsorption by MIL-53(Al)@RH packed column

Figure 6.5b shows how the increase in concentration influences the breakthrough point due to the higher adsorbate-adsorbent interaction. This ensures that the adsorption sites are occupied at a higher rate and the behavior of the column is more ideal since the times between the breakthrough and saturation points are not too far apart. The opposite effect is observed at lower concentrations, which results in lower column efficiency.

For each of the proposed GLY concentrations, calculations of qu (mg g^{-1}), qt (mg g^{-1}), and MTZ (cm) were performed (Table 6.4).

Table 6.4. q_t, q_u, and MTZ of the GLY adsorption column at various concentrations calculated from the breakthrough curves.

	25 mg L^{-1} GLY	**50 mg L^{-1} GLY**	**100 mg L^{-1} GLY**
q_u (mg g^{-1})	38.992	40.321	76.304
q_t (mg g^{-1})	221.269	270.871	421.363
MTZ (cm)	2.471	2.553	2.712

Table 6.4 corroborates the behavior of the curves (Figure 6.5), where a better behavior is assumed at higher GLY concentrations, which is reflected in a higher total and useful adsorption capacity, and greater utilization of the total column bed.

In this context, the adsorption capacity of the column can be highlighted considering the mass of the packing (200 mg), bed height (3 cm), and column diameter (5 mm). Thus, this proposed material can be considered an attractive option for a scale-up study for the treatment of larger volumes of the affluent.

6.3.4. Adsorption mechanism

All of the studies that have been conducted on the effect of pH_0, kinetics, isotherms, and adsorption thermodynamics have demonstrated that the process is primarily controlled by several mechanisms, primarily chemisorption, and also physisorption. It should be considered that the hybrid maintains the physicochemical properties of its pristine materials, so the adsorption mechanism can be influenced by the elements that constitute both materials. For this, as a tool to analyze the interaction between GLY and MIL-53(Al)@RH, the analysis of FTIR spectra of the initial MIL-53(Al)@RH, and after being contacted at concentrations of 60, 140, and 300 mg L^{-1} of GLY (Figure 6.6a), is proposed as a tool to analyze the interaction between GLY and MIL-53(Al)@RH. According to Fernández-Andrade et al. (36), the FTIR spectrum of MIL-53(Al)@RH shows a band from 3007 to 3660 cm^{-1} that is related to the OH groups belonging to the cellulose of RH. It is observed that this band undergoes a stretching with increasing GLY concentration, which is attributed to the OH groups in the fiber forming hydrogen bonds with the anionic GLY^- species. At 1056 cm^{-1} a peak corresponding to Si-O-Si was observed, which also shows a stretching with GLY concentration. This behavior is related to the formation of hydrogen bonds between the amino group of GLY and the oxygens of the siloxane groups on the RH surface, or the bind of GLY molecules and siloxane groups on the RH surface through the mediation of water molecules. In addition, the RH silicates may favor an acid-base reaction mechanism acting as Lewis bases (Figure 6.6b).

On the other hand, it could be observed that there is a reduction of the peak at 1606 cm^{-1}, which is attributed to the C=C double bond of the aromatic ring that is part of the MIL-53(Al) structure. This reduction may be related to π*-π interactions between the amino group of GLY and the aromatic rings. Likewise, there is a reduction of the peaks at 1417 cm^{-1} and 758 cm^{-1}, corresponding to the O-C-O carboxylate groups coordinated with Al, and to the Al-O bond formed by the octahedra at the corners of the MOF, respectively. The reduction of these peaks can be related to the involvement of the metal centers as anchored nodes to bind to the GLY molecules. Purgel et al. (66) showed that there is a strong interaction between GLY and Al, through complexation between Al^{3+}-phosphonate groups, which maintain a highly stable chelating effect. Thus, the majority participation of the phosphonate group in several of the adsorption mechanisms is demonstrated.

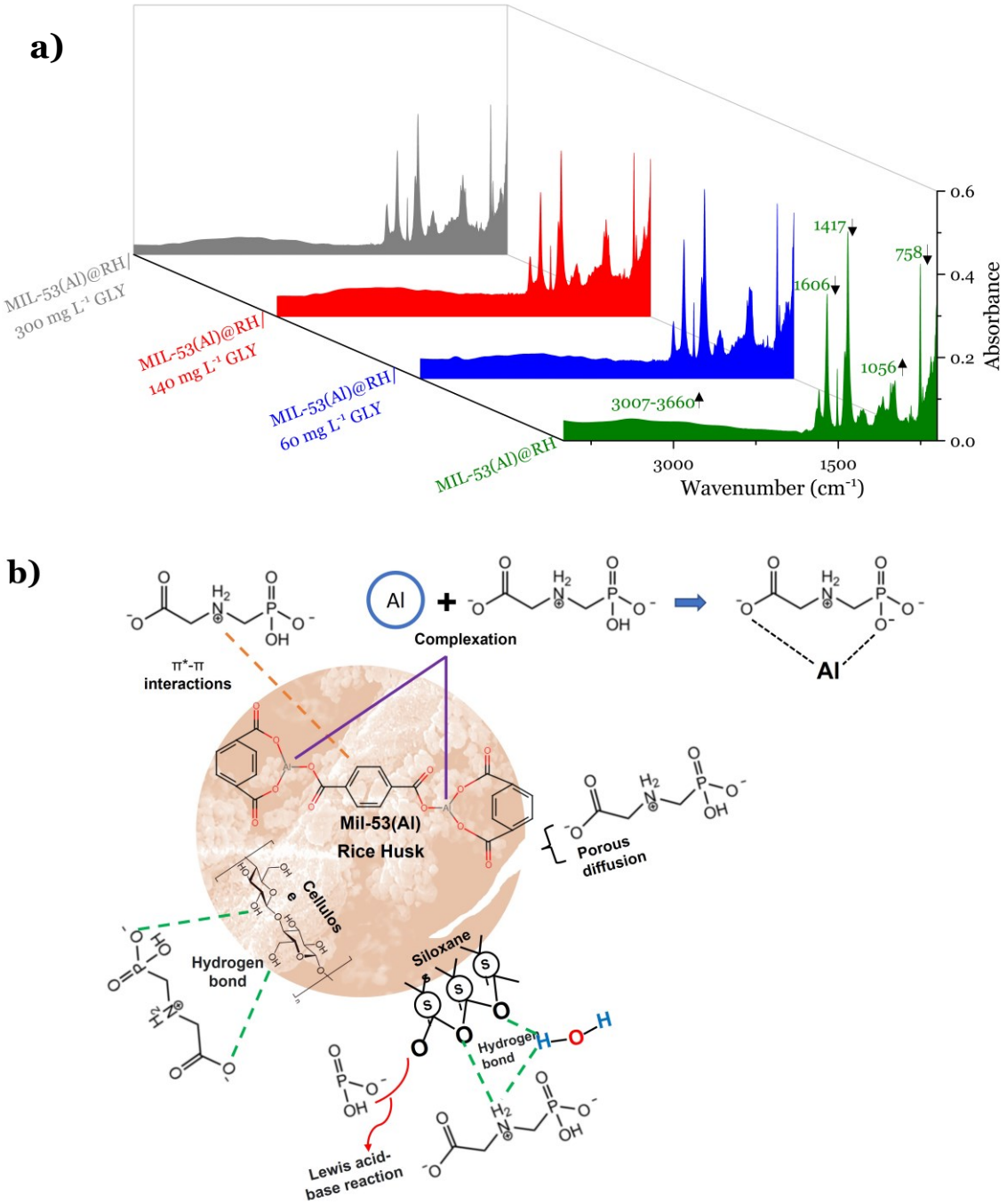


Figure 6.6. a) FTIR spectra of MIL-53(Al)@RH before and after contact with GLY solutions at 60, 140, and 300 mg L^{-1}, and b) Schematic illustration of the possible mechanism of GLY adsorption on MIL-53(Al)@RH.

6.4. Conclusion

In the present work, the hybrid MIL-53(Al)@RH synthesized through microwave assistance was successfully used for the removal of GLY. The hybrid exhibits remarkable adsorption capacity owing to the functional groups contributed by the two synthetic materials, its high surface area, and pore volume. In principle, the adsorption of GLY was highly dependent on the pH_0 of the solution (pH = 4), the molecule is in the anionic state of GLY^-, favored by a predominantly chemical type mechanism, which was proposed by the Avrami and PSO kinetic models. Likewise, Langmuir and Sips equilibrium models suggests the predominance of chemisorption. Moreover, this behavior was corroborated by the calculation of thermodynamic variables. On the other hand, FTIR spectra allowed to better elucidate the possible mechanisms, demonstrating the formation of hydrogen bridges, π*-π interactions, and the participation of the aluminum metal center of the MOF as an anchored node to form complexes with the anionic GLY^- groups. Finally, the dynamic study allowed us to verify that the process could be scaled up once there was no pressure drop in the system. Thus, it was determined that the hybrid can be utilized in a fixed bed system with good breakthrough times and useful adsorption capacity associated with the high exploitation of MTZ.

6.5. References

1. Md Meftaul I, Venkateswarlu K, Dharmarajan R, Annamalai P, Megharaj M. Pesticides in the urban environment: A potential threat that knocks at the door. Sci Total Environ. 2020;711:134612.
2. Heap I, Duke SO. Overview of glyphosate-resistant weeds worldwide. Pest Manag Sci. 2018;74(5):1040–9.
3. Singh S, Kumar V, Datta S, Wani AB, Dhanjal DS, Romero R, et al. Glyphosate uptake, translocation, resistance emergence in crops, analytical monitoring, toxicity and degradation: a review. Environ Chem Lett. 2020;18(3):663–702.
4. Xu J, Smith S, Smith G, Wang W, Li Y. Glyphosate contamination in grains and foods: An overview. Food Control. 2019;106:106710.
5. Melton LM, Taylor MJ, Flynn EE. The utilisation of ion chromatography and tandem mass spectrometry (IC-MS/MS) for the multi-residue simultaneous determination of highly polar anionic pesticides in fruit and vegetables. Food Chem. 2019;298:125028.
6. Zambrano-Intriago LA, Amorim CG, Rodríguez-Díaz JM, Araújo AN, Montenegro MCBSM. Challenges in the design of electrochemical sensor for glyphosate-based on new materials and biological recognition. Sci Total Environ. 2021;793:148496.
7. Zambrano-Intriago LA, Amorim CG, Araújo AN, Gritsok D, Rodríguez-Díaz JM,

Montenegro MCBSM. Development of an inexpensive and rapidly preparable enzymatic pencil graphite biosensor for monitoring of glyphosate in waters. Sci Total Environ. 2023;855:158865.

8. WHO/FAO. Report of the joint meeting of the FAO Panel of Experts on pesticide residues in food and the environment and the WHO Core Assessment Group on Pesticide Residues (JMPR). [Internet]. FAO Plant Production and Protection Paper. Rome: World Health Organization/Food and Agriculture Organization of the United Nations.; 2004 Sep.
9. IARC. Some organophosphate insecticides and herbicides [Internet]. Vol. 112, IARC Monographs. Leon: International Agency for Research on Cancer; 2015.
10. Koller VJ, Fürhacker M, Nersesyan A, Mišík M, Eisenbauer M, Knasmueller S. Cytotoxic and DNA-damaging properties of glyphosate and Roundup in human-derived buccal epithelial cells. Arch Toxicol. 2012;86(5):805–13.
11. Kwiatkowska M, Reszka E, Wozniak K, Jablonska E, Michalowicz J, Bukowska B. DNA damage and methylation induced by glyphosate in human peripheral blood mononuclear cells (in vitro study). Food Chem Toxicol. 2017;105:93–8.
12. Wozniak E, Sicinska P, Michalowicz J, Wozniak K, Reszka E, Huras B, et al. The mechanism of DNA damage induced by Roundup 360 PLUS, glyphosate and AMPA in human peripheral blood mononuclear cells - genotoxic risk assessement. Food Chem Toxicol. 2018;120:510–22.
13. Thongprakaisang S, Thiantanawat A, Rangkadilok N, Suriyo T, Satayavivad J. Glyphosate induces human breast cancer cells growth via estrogen receptors. Food Chem Toxicol. 2013;59:129–36.
14. Manas F, Peralta L, Raviolo J, Ovando HG, Weyers A, Ugnia L, et al. Genotoxicity of glyphosate assessed by the comet assay and cytogenetic tests. Env Toxicol Pharmacol. 2009;28(1):37–41.
15. Ehrl BN, Mogusu EO, Kim K, Hofstetter H, Pedersen JA, Elsner M. High Permeation Rates in Liposome Systems Explain Rapid Glyphosate Biodegradation Associated with Strong Isotope Fractionation. Environ Sci Technol. 2018;52(13):7259–68.
16. Zhan H, Feng Y, Fan X, Chen S. Recent advances in glyphosate biodegradation. Appl Microbiol Biotechnol. 2018;102(12):5033–43.
17. Carneiro RTA, Taketa TB, Gomes Neto RJ, Oliveira JL, Campos EVR, de Moraes MA, et al. Removal of glyphosate herbicide from water using biopolymer membranes. J Environ Manage. 2015;151:353–60.
18. Cevallos-Mendoza J, Amorim CG, Rodríguez-Díaz JM, Montenegro M da CBSM. Removal of Contaminants from Water by Membrane Filtration: A Review.

Membranes (Basel). 2022;12(6).

19. Feng D, Soric A, Boutin O. Treatment technologies and degradation pathways of glyphosate: A critical review. Sci Total Environ. 2020;742:140559.
20. Napoleão DC, E. MCZL, J.M. RD, da RSRM, M.C. B da S de MM, da NAA, et al. Use of the photo-Fenton process to discover the degradation of drugs present in water from the Wastewater Treatment Plants of the pharmaceutical industry. Afinidad J Chem Eng Theor Appl Chem. 2018;75(581 SE-Articles).
21. Tapia-Tlatelpa T, Buscio V, Trull J, Sala V. Performance analysis and methodology for replacing conventional lamps by optimized LED arrays for photocatalytic processes. Chem Eng Res Des. 2020;156:456–68.
22. Zaidan LEMC, de Lima Sales RV, de Almeida Salgado JB, da Silva AMRB, Napoleão DC, Rodríguez-Díaz JM, et al. Photodegradation applied to the treatment of phenol and derived substances catalyzed by TiO2/BiPO4 and biological toxicity analysis. Environ Sci Pollut Res. 2017;24(7):6002–12.
23. Gorozabel-Mendoza ML, Filho OAE, Zambrano-Intriago LA, Baquerizo-Crespo RJ, Giler-Molina JM, Rodríguez-Díaz JM. Degradation of Blue 1 and Yellow 6 Dyes in Binary Mixture Using Photo-Fenton/Sunlight System: Optimization by Factorial Designs. Water, Air, Soil Pollut. 2021;232(12):500.
24. Gkika DA, Mitropoulos AC, Kyzas GZ. Why reuse spent adsorbents? The latest challenges and limitations. Sci Total Environ. 2022;822:153612.
25. Pereira HA, Hernandes PRT, Netto MS, Reske GD, Vieceli V, Oliveira LFS, et al. Adsorbents for glyphosate removal in contaminated waters: a review. Environ Chem Lett. 2021;19(2):1525–43.
26. Sun Y, Zhou HC. Recent progress in the synthesis of metal–organic frameworks. Sci Technol Adv Mater. 2015;16(5):54202.
27. Pang Q, Tu B, Li Q. Metal–organic frameworks with multicomponents in order. Coord Chem Rev. 2019;388:107–25.
28. Lorignon F, Gossard A, Carboni M. Hierarchically porous monolithic MOFs: An ongoing challenge for industrial-scale effluent treatment. Chem Eng J. 2020;393:124765.
29. Isiyaka HA, Jumbri K, Sambudi NS, Zango ZU, Fathihah Abdullah NA, Saad B, et al. Adsorption of dicamba and MCPA onto MIL-53(Al) metal–organic framework: response surface methodology and artificial neural network model studies. RSC Adv. 2020;10(70):43213–24.
30. Seoane B, Téllez C, Coronas J, Staudt C. NH2-MIL-53(Al) and NH2-MIL-101(Al) in sulfur-containing copolyimide mixed matrix membranes for gas separation. Sep Purif

Technol. 2013;111:72–81.

31. Rivadeneira-Mendoza BF, Estrela Filho OA, Fernández-Andrade KJ, Curbelo F, Fred da Silva F, Luque R, et al. MOF@biomass hybrids: Trends on advanced functional materials for adsorption. Environ Res. 2023;216:114424.
32. Rojas R, Vanderlinden E, Morillo J, Usero J, El Bakouri H. Characterization of sorption processes for the development of low-cost pesticide decontamination techniques. Sci Total Environ. 2014;488–489:124–35.
33. Kaur P, Kaur P, Kaur K. Adsorptive removal of imazethapyr and imazamox from aqueous solution using modified rice husk. J Clean Prod. 2020;244:118699.
34. Gurav R, Bhatia SK, Choi TR, Choi YK, Kim HJ, Song HS, et al. Adsorptive removal of crude petroleum oil from water using floating pinewood biochar decorated with coconut oil-derived fatty acids. Sci Total Environ. 2021;781:146636.
35. Gu C, Wang Q, Zhang L, Yang P, Xie Y, Fei J. Ultrasensitive non-enzymatic pesticide electrochemical sensor based on HKUST-1-derived copper oxide @ mesoporous carbon composite. Sensors Actuators B Chem. 2020;305:127478.
36. Fernández-Andrade KJ, Fernández-Andrade AA, Zambrano-Intriago LÁ, Arteaga-Perez LE, Alejandro-Martin S, Baquerizo-Crespo RJ, et al. Microwave-assisted MOF@biomass layered nanomaterials: Characterization and applications in wastewater treatment. Chemosphere. 2022;137664.
37. Zambrano-Intriago LA, Gorozabel-Mendoza ML, Córdova Mosquera A, Delgado-Demera MH, Duarte MMMB, Rodríguez-Díaz JM. Kinetics, equilibrium, and thermodynamics of the blue 19 dye adsorption process using residual biomass attained from rice cultivation. Biomass Convers Biorefinery. 2020;
38. Geankoplis CJ. Transport Processes and Unit Operations [Internet]. Prentice Hall; 1992.
39. Fernández-Andrade KJ, González-Vargas MC, Rodríguez-Rico IL, Ruiz-Reyes E, Quiroz-Fernández LS, Baquerizo-Crespo RJ, et al. Evaluation of mass transfer in packed column for competitive adsorption of Tartrazine and brilliant blue FCF: A statistical analysis. Results Eng. 2022;14:100449.
40. Chen Q, Zheng J, Yang Q, Dang Z, Zhang L. Insights into the Glyphosate Adsorption Behavior and Mechanism by a MnFe2O4@Cellulose-Activated Carbon Magnetic Hybrid. ACS Appl Mater Interfaces. 2019;11(17):15478–88.
41. Marin P, Bergamasco R, Módenes AN, Paraiso PR, Hamoudi S. Synthesis and characterization of graphene oxide functionalized with MnFe2O4 and supported on activated carbon for glyphosate adsorption in fixed bed column. Process Saf Environ Prot. 2019;123:59–71.

42. Al Sharabati M, Sabouni R. Selective removal of dual dyes from aqueous solutions using a metal organic framework (MIL-53(Al)). Polyhedron. 2020;190:114762.
43. Qian X, Yadian B, Wu R, Long Y, Zhou K, Zhu B, et al. Structure stability of metal-organic framework MIL-53 (Al) in aqueous solutions. Int J Hydrogen Energy. 2013;38(36):16710–5.
44. Ahmad M, Lee SS, Rajapaksha AU, Vithanage M, Zhang M, Cho JS, et al. Trichloroethylene adsorption by pine needle biochars produced at various pyrolysis temperatures. Bioresour Technol. 2013;143:615–22.
45. Lagergren SK. About the theory of so-called adsorption of soluble substances. Sven Vetenskapsakad Handingarl. 1898;24:1–39.
46. Ho YS, McKay G. Pseudo-second order model for sorption processes. Process Biochem. 1999;34(5):451–65.
47. Avrami M. Kinetics of phase change. II transformation-time relations for random distribution of nuclei. J Chem Phys. 1940;8(2):212–24.
48. Avrami M. Granulation, phase change, and microstructure kinetics of phase change. III. J Chem Phys. 1941;9(2):177–84.
49. Avrami M. Kinetics of phase change. I General theory. J Chem Phys. 1939;7(12):1103–12.
50. Bangham DH, Burt FP, Dixon HB. The behaviour of gases in contact with glass surfaces. Proc R Soc London Ser A, Contain Pap a Math Phys Character. 1924;105(732):481–8.
51. Weber Jr WJ, Morris JC. Kinetics of adsorption on carbon from solution. J Sanit Eng Div. 1963;89(2):31–59.
52. Ko SJ, Yamaguchi T, Salles F, Oh JM. Systematic utilization of layered double hydroxide nanosheets for effective removal of methyl orange from an aqueous system by π-π stacking-induced nanoconfinement. J Environ Manage. 2021;277:111455.
53. Jiang L hua, Liu Y guo, Zeng G ming, Xiao F yu, Hu X jiang, Hu X, et al. Removal of 17β-estradiol by few-layered graphene oxide nanosheets from aqueous solutions: External influence and adsorption mechanism. Chem Eng J. 2016;284:93–102.
54. Chandarana H, Senthil Kumar P, Seenuvasan M, Anil Kumar M. Kinetics, equilibrium and thermodynamic investigations of methylene blue dye removal using Casuarina equisetifolia pines. Chemosphere. 2021;285:131480.
55. Andrade CA, Zambrano-Intriago LA, Oliveira NS, Vieira JS, Quiroz-Fernández LS, Rodríguez-Díaz JM. Adsorption Behavior and Mechanism of Oxytetracycline on Rice Husk Ash: Kinetics, Equilibrium, and Thermodynamics of the Process. Water, Air,

Soil Pollut. 2020;231(3):103.

56. Wang Y, Lin C, Liu X, Ren W, Huang X, He M, et al. Efficient removal of acetochlor pesticide from water using magnetic activated carbon: Adsorption performance, mechanism, and regeneration exploration. Sci Total Environ. 2021;778:146353.
57. Langmuir I. THE ADSORPTION OF GASES ON PLANE SURFACES OF GLASS, MICA AND PLATINUM. J Am Chem Soc. 1918;40(9):1361–403.
58. Freundlich HMF. Over the adsorption in solution. J Phys chem. 1906;57(385471):1100–7.
59. Sips R. Combined form of Langmuir and Freundlich equations. J Chem Phys. 1948;16(429):490–5.
60. Toth J. State equation of the solid-gas interface layers. Acta chim hung. 1971;69:311–28.
61. Khan AR, Ataullah R, Al-Haddad A. Equilibrium Adsorption Studies of Some Aromatic Pollutants from Dilute Aqueous Solutions on Activated Carbon at Different Temperatures. J Colloid Interface Sci. 1997;194(1):154–65.
62. Feng X, Qiu B, Dang Y, Sun D. Enhanced adsorption of naproxen from aquatic environments by β-cyclodextrin-immobilized reduced graphene oxide. Chem Eng J. 2021;412:128710.
63. Al-Ghouti MA, Da'ana DA. Guidelines for the use and interpretation of adsorption isotherm models: A review. J Hazard Mater. 2020;393:122383.
64. Sadeghalvad B, Khosravi S, Azadmehr AR. Nonlinear isotherm and kinetics of adsorption of copper from aqueous solutions on bentonite. Russ J Phys Chem A. 2016;90(11):2285–91.
65. Nanthamathee C, Dechatiwongse P. Kinetic and thermodynamic studies of neutral dye removal from water using zirconium metal-organic framework analogues. Mater Chem Phys. 2021;258:123924.
66. Purgel M, Takacs Z, Jonsson CM, Nagy L, Andersson I, Banyai I, et al. Glyphosate complexation to aluminium(III). An equilibrium and structural study in solution using potentiometry, multinuclear NMR, ATR-FTIR, ESI-MS and DFT calculations. J Inorg Biochem. 2009;103(11):1426–38.

6.6. Supplementary Data

S1. Adsorption kinetics and equilibrium models

In all the equations, q_e and q_t (mg g^{-1}) are the adsorption capacity at the equilibrium and at the time t (min), respectively, and C_e (mg L^{-1}) is the adsorbate concentration in the equilibrium.

The kinetic models used were those of pseudo-first order, pseudo-second order, Bangham, Avrami, and Weber-Morris intraparticle diffusion. The Pseudo-first order model is represented by the Lagergren equation (Equation S1) (1), where q_e and q_t are the amount of GLY adsorbed at equilibrium and at time t (mg g^{-1}), respectively, and k_1 (min^{-1}) is the adsorption rate constant. The values of q_e and k_1 were calculated from non-linear regression of the slopes ($-k_1$) and interceptions (log q_e) when graphing $\log_{10}$ ((q_e-q_t)/q) vs. t.

The Pseudo-second order kinetic model is also based on the adsorption capacity of the solid phase and shows the behaviour of the process throughout the phase of the contact time. It is represented by Equation S2 (2), where K_2 is the adsorption rate constant (g $mg^{-1}min^{-1}$), q_e and q_t (mg g^{-1}) are the amount of GLY adsorbed at equilibrium and at time t (min).

The Bangham kinetic model can be used to verify whether diffusion into the pores is the only stage of velocity control in the adsorption system using its equation (Equation S3) (3), where K and α (<1) are the empirical constants of the equation, C_o (mg L^{-1}) is the initial concentration of the adsorbate in solution, V is the volume of the solution (mL), m (g) is the mass of the adsorbent, and q_t (mg g^{-1}) is the amount of adsorbate retained per unit of adsorbent. If the experimental data can be represented by Equation S3, then the adsorption kinetics may be limited by diffusion into the pores of the adsorbent (4).

The specific Avrami adsorption equation evaluates the changes in adsorption mechanisms as a function of contact time (5) (Equation S4), where k_{AV} is the Avrami kinetic constant (min^{-1}) and n_{AV} the fractional number which reflects adsorption mechanism.

The Weber-Morris model is used to determine whether the limiting step of the adsorption process occurs by intraparticle diffusion. When plotting the adsorption capacity of the adsorbent vs. the square root of time, a straight line through the plane origin must be obtained (6). In Equation S5, K_{dif} (mg g^{-1} $min^{-0.5}$) is the kinetic constant of Weber and Morris and C is the constant related to the boundary layer. This factor has been added by the authors to provide an exact representation of the possible difference in the regression at the origin of the graph (7).

$$log_{10}\left(\frac{q_e - q_t}{q_e}\right) = \frac{-k_1}{2.303}t \qquad \text{Equation S1}$$

$$q_t = \frac{tK_2 q_e^2}{1 + tK_2 q_e} \qquad \text{Equation S2}$$

$$\log\left[\log\left(\frac{C_0}{C_0 - q_t.m}\right)\right] = \log\left(\frac{\mathrm{k}.m}{2{,}303.V}\right) + \alpha.\log t \qquad \text{Equation S3}$$

$$Qt = Qe[1 - \exp(-K_{AV} t^{n_{AV}})] \qquad \text{Equation S4}$$

$$q_t = k_{dif} t^{0,5} + C \qquad \text{Equation S5}$$

In the Langmuir model (8), q_e (mg g^{-1}) is the maximum amount of sorbate per unit weight of adsorbent required to form a complete monolayer on the surface at high Ce, and K_L (L mg^{-1}) is determined by the C_e/q_e versus Ce graph (Equation S6). Concerning the Freundlich model (9) (Equation S7), K_f and n are the constants (n is dimensionless; K_f (mg $L^{-1}g^{-1}$ $L^{1/n}$)). In the Toth model (10) (Equation S8), K_T (mg g^{-1}) and aT (L mg^{-1}) are adsorption constants. In of the Sips model (11) (Equation S9), q_e (mg g^{-1}) is the amount of adsorbate adsorbed at equilibrium, C_e (mg L^{-1}) is the concentration of the aqueous phase at equilibrium, K_s (L mg^{-1}) is the Sips constant and n is the index of heterogeneity.

Khan isotherm is a generalized model suggested for the adsorbate adsorption from pure solutions, in which it is representing both Langmuir and Freundlich models (Equation S10). The development of this isotherm model was made for single-component and multicomponent adsorption systems. When a_K is equal to unity, Equation S10 reduces to the Langmuir isotherm. This equation at high concentration of Ce reduces to the Freundlich isotherm.

$$q_e = \frac{K_L q_m C_e}{1 + K_L C_e} \qquad \text{(Equation S6)}$$

$$q_e = K_{F.} {C_e}^{1/n} \qquad \text{(Equation S7)}$$

$$qe = \frac{K_T * C_e}{[a_T + C_e^t]^{\frac{1}{t}}} \qquad \text{(Equation S8)}$$

$$qe = \frac{K_s * C_e^{\beta s}}{1 + a_s C_e^{\beta s}} \qquad \text{(Equation S9)}$$

$$q_e = \frac{q_s b_k C_e}{(1 + b_k C_e)^{a_K)}} \qquad \text{(Equation S10)}$$

S2. Thermodynamics parameters

The thermodynamic parameters of the adsorption processes were determined by carrying out a study at temperatures of 288.15, 298.15, 313.15, and 328.15 K. The free energy of adsorption (ΔG°) was calculated using Van't Hoff's equation (Equation S11), where K_c is the constant obtained by multiplying the equilibrium constant by 55.5 and 1000 (12), and R is the gas constant (8.314 J/mol K). Adsorption enthalpy (ΔHº) and adsorption entropy (ΔSº) were calculated by employing the adsorption data at different temperatures using Equation S12 (13). The magnitude of ΔHº and ΔSº was calculated through the slope and intercept of the $\ln K_c$ vs 1/T graph.

$\Delta G^0 = -RT\ln K_c$ (Equation S11) $ln(K_c) = \frac{\Delta S}{R} - \frac{\Delta H}{RT}$ (Equation S12)

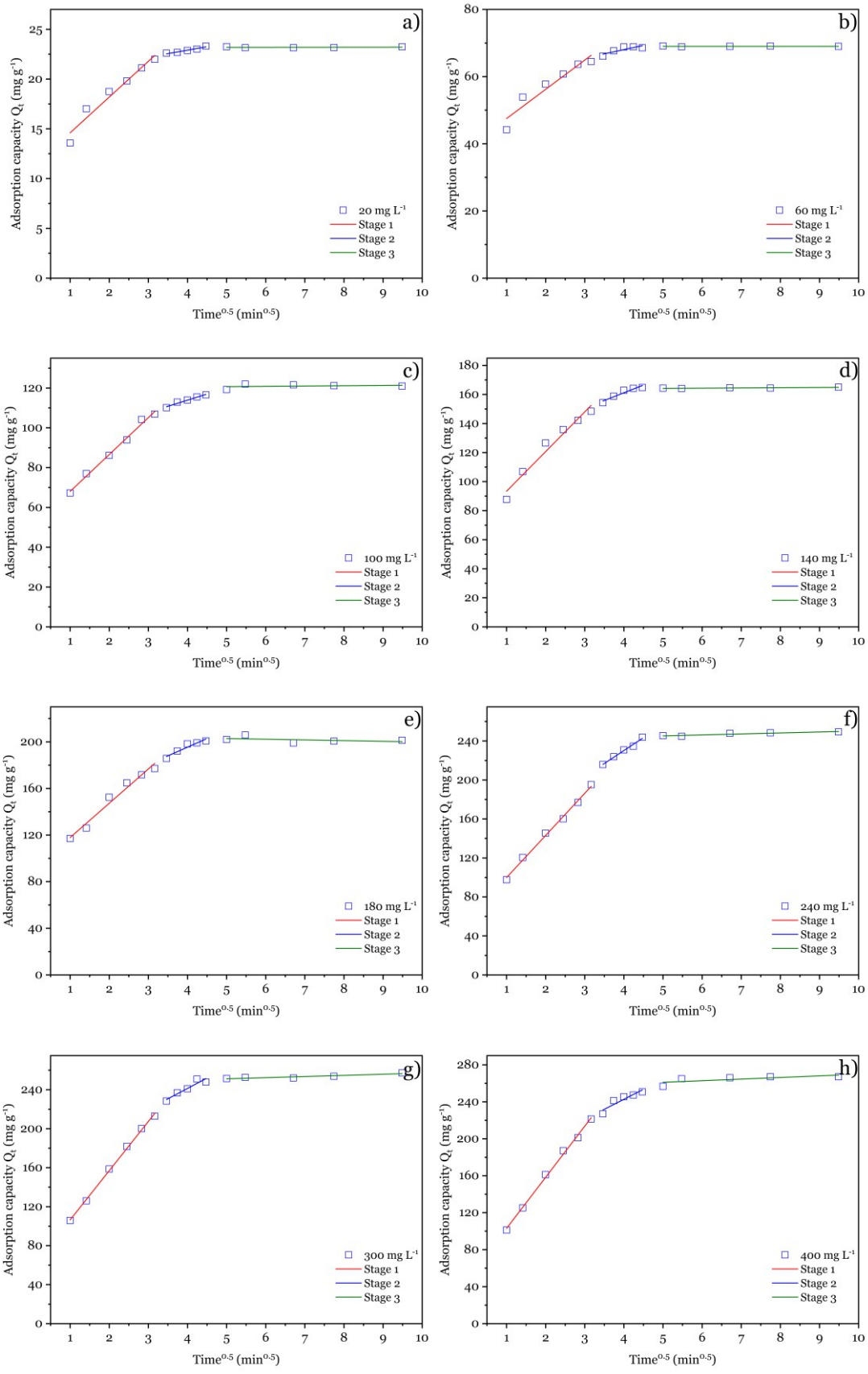


Figure S1. Weber-Morris intraparticle diffusion model adjusted to experimental data for different initial concentrations: a) 20 mg L^{-1}, b) 60 mg L^{-1}, c) 100 mg L^{-1}, d) 140 mg L^{-1}, e) 180 mg L^{-1}, f) 240 mg L^{-1}, g) 300 mg L^{-1}, and h) 400 mg L^{-1} (w = 0.04 g, V = 50 ml, pH_0 = 4.0, T = 298.15 K).

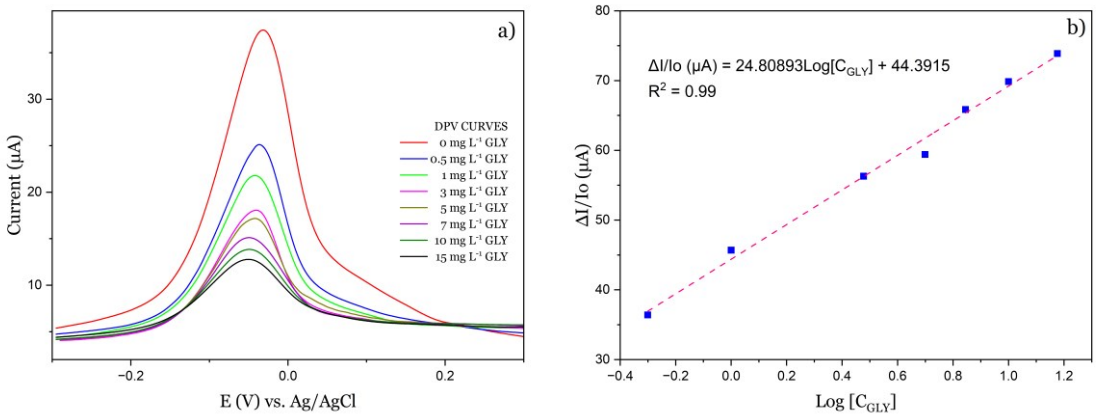


Figure S2. a) First DPV curves of CuOx@mC/GCE (sensor 1) in 0.1 M PBS and 0.05 M NaCl with GLY concentrations from 0.5 to 15 mg L^{-1}, and b) The corresponding calibration curves between ΔI/Io (μA) vs. Log [C_{GLY}].

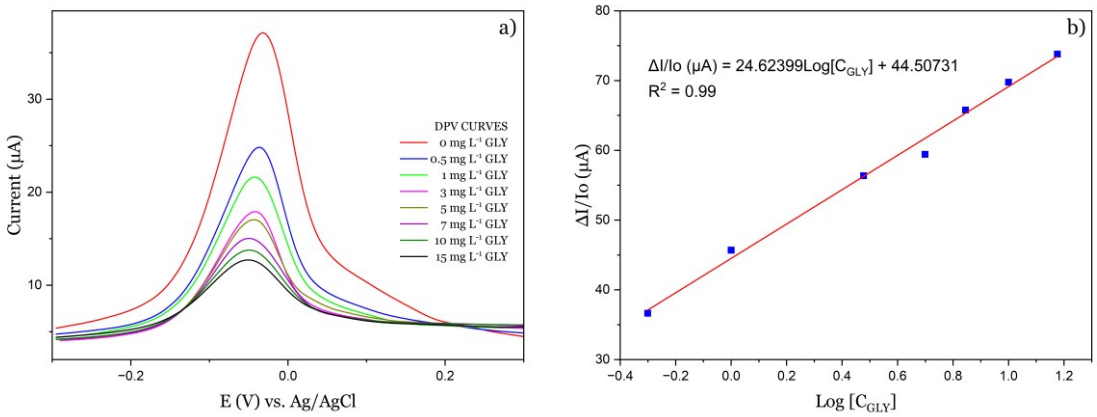


Figure S3. a) Second DPV curves of CuOx@mC/GCE (sensor 1) in 0.1 M PBS and 0.05 M NaCl with GLY concentrations from 0.5 to 15 mg L^{-1}, and b) The corresponding calibration curves between ΔI/Io (µA) vs. Log [C_{GLY}].

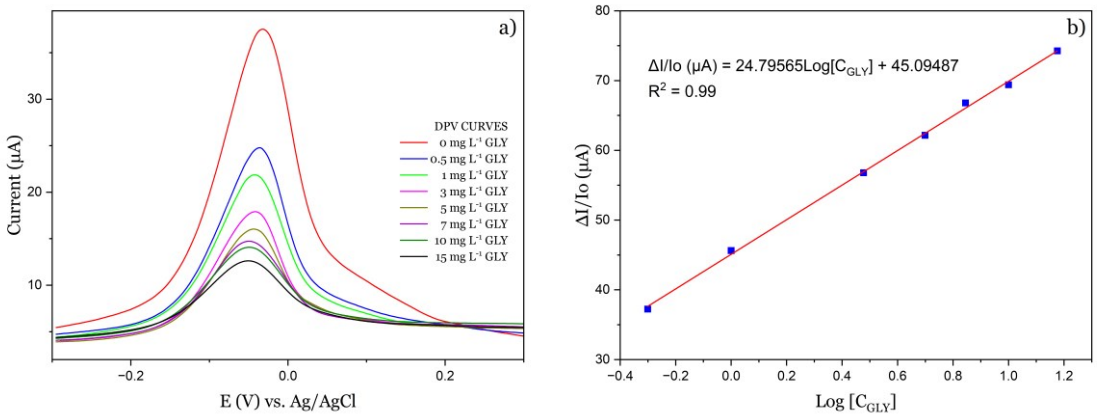


Figure S4. a) Third DPV curves of CuOx@mC/GCE (sensor 1) in 0.1 M PBS and 0.05 M NaCl with GLY concentrations from 0.5 to 15 mg L^{-1}, and b) The corresponding calibration curves between ΔI/Io (µA) vs. Log [C_{GLY}].[4]

[4] The other DPV and calibration curves can be found in the Mendeley Data base (DOI: 10.17632/89ghm7v984.1).

References

1. Lagergren SK. About the theory of so-called adsorption of soluble substances. Sven Vetenskapsakad Handingarl. 1898;24:1–39.
2. Ho YS, McKay G. Pseudo-second order model for sorption processes. Process Biochem. 1999;34(5):451–65.
3. Bangham DH, Burt FP, Dixon HB. The behaviour of gases in contact with glass surfaces. Proc R Soc London Ser A, Contain Pap a Math Phys Character. 1924;105(732):481–8.
4. Ren X, Liu S, Qu R, Xiao L, Hu P, Song H, et al. Synthesis and characterization of single-phase submicron zeolite Y from coal fly ash and its potential application for acetone adsorption. Microporous Mesoporous Mater. 2020;295:109940.
5. Oladoja NA. A critical review of the applicability of Avrami fractional kinetic equation in adsorption-based water treatment studies. Desalin Water Treat. 2016;57(34):15813–25.
6. Weber Jr WJ, Morris JC. Kinetics of adsorption on carbon from solution. J Sanit Eng Div. 1963;89(2):31–59.
7. Mane VS, Mall ID, Srivastava VC. Use of bagasse fly ash as an adsorbent for the removal of brilliant green dye from aqueous solution. Dye Pigment. 2007;73(3):269–78.
8. Langmuir I. THE ADSORPTION OF GASES ON PLANE SURFACES OF GLASS, MICA AND PLATINUM. J Am Chem Soc. 1918;40(9):1361–403.
9. Freundlich HMF. Over the adsorption in solution. J Phys chem. 1906;57(385471):1100–7.
10. Toth J. State equation of the solid-gas interface layers. Acta chim hung. 1971;69:311–28.
11. Sips R. Combined form of Langmuir and Freundlich equations. J Chem Phys. 1948;16(429):490–5.
12. Tran HN, You SJ, Hosseini-Bandegharaei A, Chao HP. Mistakes and inconsistencies regarding adsorption of contaminants from aqueous solutions: A critical review. Water Res. 2017;120:88–116.
13. MacQueen JT. Some observations concerning the van't Hoff equation. J Chem Educ. 1967;44(12):755.

Chapter 7

General Conclusions

Electrochemical sensors are an effective analytical tool for GLY detection systems. These are particularly beneficial because of their small size, portability, sensitivity, specificity, and low cost of construction. Electrodes for GLY detetction were chemically and physically modified for better electrocatalytic activity. These have been extensively exploited by investigating new immobilization designs (biomaterials as enzymes) and surface supports.

The research conducted in this thesis attempted to contribute to the creation of portable and autonomous biosensors that are inexpensive and can provide accurate results. The general objectives were accomplished by the design of an amperometric enzymatic biosensor that utilized PGE as a transducer. This type physical support is a valuable electroanalytical tool applied in sensors and biosensors, due to their sp2 carbon graphite composition, which influences their excellent conductive properties. The sensor was developed using a PSF membrane modified with MWCNT as conductive material and with the HRP enzyme immobilized. The PGE electrode surface was covered with this membrane. The correct immobilization of HRP was evaluated by SEM/EDS, FTIR, and the electrocatalytic behaviour through voltammetric, amperometric and impedance techniques. In the first instance, the conditions of the electrochemical environment of the cell were optimized so that the enzymatic reaction with the substrate H_2O_2 in the presence of HQ as a redox mediator could be detected. The results with substrate showed that HRP obtains good sensitivity, which defines the correct immobilization and the appropriate composition of the conductive materials to guarantee the electronic flow, and the adequate connection of HRP with the bulk solution. Finally, as the biosensor had controlled and reproducible conditions, it was possible to apply it for indirect measurement by the effect of enzymatic inhibition against inhibitors such as GLY. The detection principle was based on the competitive inhibition of the HRP enzyme by coordination of the NH_2 group with the oxygen atoms present in the carbonyl groups of the peroxidase, forming a GLY-enzyme complex unavailable for further interaction with H_2O_2. From the fixed substrate concentration, it was possible to develop a method with a linear detection range of 0.1 to 10 mg L^{-1}, with LOD of 0.025 ± 0.002 mg L^{-1}, ideal for compliance with regulations such as the EPA. Finally, sensitivity and selectivity tests demonstrated that this device could become a valuable tool for analysis in real samples.

The second phase of the doctoral research consisted of the development of technologies for the remediation of aqueous media contaminated with GLY. One of the biggest problems in wastewater treatment plants to date is the removal of emerging organic pollutants such as GLY. Currently, one of the major trends in the development of functionalized materials between biomasses and complex structures that are capable of removing high concentrations of pollutants from water. Therefore, the use of microwave assisted synthesis of the MOF Mil-53(Al) in the presence of rice husk was proposed for the formation of the hybrid Mil-53(Al)@RH. The physicochemical characterization of this material by SEM, BET, XRD, FTIR, TGA, and pH_{PZC} techniques showed that Mil-53(Al)@RH has an adequate presence of constituents and physicochemical properties of pristine materials, proving to be a potential adsorbent material. By obtaining a hybrid, problems that MOFs constantly present such as particle size and low synthesis yield were eliminated. The application of this material for GLY adsorption tests in Batch and column systems, allowed to elucidate that Mil-53(Al)@RH can remove this pollutant through chemical interactions such as Hydrogen bonds, π*-π interactions, and complexes between the metal center of Mil-53(Al) and the anionic groups of glyphosate, which promotes a strong attraction and avoid desorption. In this way, Mil-53(Al)@RH can remove GLY at rates up to 296.95 mg g^{-1} favoured by the high surface area provided by the MOF, and the heterogeneous presence of functional groups provided by both materials. Finally, in this chapter, as a methodology, the potential application of electrochemical sensors for monitoring the concentration of contaminants in treatment systems was demonstrated, becoming a viable alternative tool to conventional analytical methods.

Appendix

Appendix A. Short CV

1993. Born on the 26th of August in Portoviejo, Ecuador.

1999 - 2005. Primary school education – 5 de Junio, Portoviejo.

2005 - 2011. High school education – Colegio Técnico Industrial Latinoamericano, Portoviejo.

2011 - 2017. Degree in Chemical Engineering – Universidad Técnica de Manabí, Ecuador.

2018 - 2023. Ph.D. studies in Pharmaceutical Sciences – University of Porto, Portugal.

Papers directly resulting from the Doctoral Thesis

1. Zambrano-Intriago, L.A.; Amorim, C.G.; Rodríguez-Díaz, J.M.; Araújo, A.N.; Montenegro, M.C.B.S.M. Challenges in the design of electrochemical sensor for glyphosate-based on new materials and biological recognition. Science of the Total Environment. 2021, 793, 148496, doi:https://doi.org/10.1016/j.scitotenv.2021.148496.
2. Zambrano-Intriago, L.A.; Amorim, C.G.; Araújo, A.N.; Gritsok, D.; Rodríguez-Díaz, J.M.; Montenegro, M.C.B.S.M. Development of an inexpensive and rapidly preparable enzymatic pencil graphite biosensor for monitoring of glyphosate in waters. Science of the Total Environment. 2023, 855, 158865, doi:https://doi.org/10.1016/j.scitotenv.2022.158865.
3. Zambrano-Intriago LA, Daza-López EV, Fernández-Andrade A, Luque R, Amorim CG, Araújo AN, Rodríguez-Díaz JM, Montenegro MCBSM. Application of a novel hybrid Mil-53(Al)@rice husk for the adsorption of glyphosate in water: Characteristics and mechanism of the process. Chemosphere. 2023, 327, 138457, doi:https://doi.org/10.1016/j.chemosphere.2023.138457

Papers indirectly resulting from the Doctoral Thesis

1. Zambrano-Intriago, L.A.; Amorim, C.G.; Rodríguez-Díaz, J.M.; Montenegro, M.C.B.S.M.; Araújo, A.N. Electrochemical Biosensing of Algal Toxins. In Advances in the Domain of Environmental Biotechnology: Microbiological Developments in Industries, Wastewater Treatment and Agriculture; Maddela, N.R., García Cruzatty, L.C., Chakraborty, S., Eds.; Springer Singapore: Singapore, 2021; pp. 227–252 ISBN 978-981-15-8999-7.
2. Daza-López, E.V.; Fernández-Andrade, K.J.; Nóbrega, R. de Q.; Zambrano-Intriago, L.Á.; Villanueva Ramos, G.; Quiroz-Fernández, L.S.; Montenegro, M.C.B.S.M.; Rodríguez-Díaz, J.M. Modified or Functionalized Natural Bioadsorbents: New Perspectives as Regards the Elimination of Environmental Pollutants BT - Advances in the Domain of Environmental Biotechnology: Microbiological Developments in Industries, Wastewater Treatment and Agriculture. In; Maddela, N.R., García Cruzatty, L.C., Chakraborty, S., Eds.; Springer Singapore: Singapore, 2021; pp. 195–225 ISBN 978-981-15-8999-7.
3. Fernández-Andrade K.J.; Fernández-Andrade A.A.; Ávila-Toro B.A.; Zambrano-Intriago L.A.; Baquerizo-Crespo R.J.; Rodríguez-Díaz J.M. Nanocatalysts for Advanced Oxidation Processes in Heterogeneous Systems: Characteristics, Classification, and Future Perspective - Handbook of Green and Sustainable Nanotechnology. In; U. Shanker et al. (eds.).; Springer Nature Switzerland AG 2022; https://doi.org/10.1007/978-3-030-69023-6_10-1

Oral communications

1. C.G. Amorim*, L.A. Zambrano-Intriago, A.N. Araújo, J.M. Rodríguez-Díaz, M.C.B.S.M. Montenegro. Development of an enzymatic biosensor for determination of glyphosate in environmental samples. II Convención Científica Internacional UCLV 2019, VII Simpósio Internacional de Química 2019. June 2019, Santa Clara (Cuba).
2. L.A. Zambrano-Intriago***,** C.G. Amorim, A.N. Araújo, J.M. Rodríguez-Díaz, M.C.B.S.M. Montenegro. Glyphosate electrochemical biosensor based on pencil graphite. III Congreso de Ingeniería Aplicada, Cuarta Convención Científica Internacional de la UTM 2020. October 2020, Portoviejo (Ecuador)

Posters

1. L.A. Zambrano-Intriago*, C.G. Amorim, A.N. Araújo, J.M. Rodríguez-Díaz, M.C.B.S.M. Montenegro. Development of a new support platform for glyphosate biosensor. 26th National Meeting of the Portuguese Chemical Society. June 2019, Porto (Portugal)

Environmental contamination by the broad-spectrum herbicide glyphosate: development of simple and low-cost analytical procedures for its quantification and remediation technologies

Luis Angel Zambrano Intriago

Faculdade de Farmácia

